NTNU

Norwegian University of
Science and Technology

Characterization and Mechanical Testing of Co-Extruded Rods with an AA6082 Core and Rapidly Solidified AA7090/AA7090-Sc Sleeve

Vegard Jørgenvåg Bjerkestrand

Materials Technology (MIMT)
Submission date: June 2018
Supervisor: Hans Jørgen Roven, IMA
Co-supervisor: Xiang Ma, SINTEF Materials and Chemistry
Rune Østhus, SINTEF Raufoss Manufacturing
Christian Simensen, SINTEF Materials and Chemistry

Norwegian University of Science and Technology
Department of Materials Science and Engineering

Preface

This thesis is written at the Department of Materials Science and Engineering at NTNU as a part of the Materials Technology master project in the spring of 2018. The master project is carried out in collaboration with a SINTEF Industry research project, partially supported by the Hydro-fond project. This thesis is a result of individual work, with good help with regards to experimental work and interpretation of the results.

Trondheim, June 2018
Vegard Jørgenvåg Bjerkestrand

Acknowledgement

I would like to thank those involved in this project who helped with the experimental work and analysis: Morten Ingar Onsøien, Trygve Lindahl Schanche, Yingda Yu and Pål Christian Skaret. I would also like to thank the experts, who're a part of this research project, for feedback and input: Xiang Ma and Christian J. Simensen from SINTEF Industry and Rune Østhus from SINTEF Raufoss Manufacturing. Finally, I would like to thank my supervisor Prof. Hans Jørgen Roven of the Department of Materials Science and Engineering at NTNU. The door to his office was always open and he guided me in the right direction whenever I had any questions or problems.

Aims

The aim of the SINTEF Industry research project was to produce hybrid materials with excellent properties. In this thesis, the goal was to produce rapidly solidified AA7090, co-extrude it as the sleeve material and AA6082 as the core material and characterize the rods properties.

Abstract

The development and implementation of materials having a combination of mechanical properties, e.g. high strength and high ductility, have been of interest within the material science community for decades. In the growing demand for green energy and reduction of emissions, the implementation of lighter metals such as aluminium is of significant importance.

Co-extrusion is a process that can be used to produce lightweight parts with a combination of good mechanical properties and reduced cost. In this project, the aim was to produce two types of hybrid aluminium materials having a high strength sleeve of (i) AA7090 or (ii) AA7090 with additions of Sc. While an AA6082 alloy was used as the core material, maintaining high ductility. The sleeve material of AA7090/AA7090-Sc was produced by rapid solidification through melt spinning to attain a material with unique properties unattainable by conventional casting methods. The 12 mm diameter co-extruded rods achieved excellent metallurgical bonding between the two dissimilar alloys.

The precipitation hardening response of the two dissimilar alloys was investigated. After solution heat treatment at 470°C and precipitation heat treatment at 140°C for 8 hours, the sleeve of rapidly solidified AA7090 and AA7090-Sc displayed a hardness of 216 HV1 and 210 HV1, respectively. While the hardness of the AA6082 core material was approximately 45 HV1. Microstructural characterization after solution heat treatment showed that the AA7090 alloy with additions of Sc displayed improved resistance to recrystallization. Tensile testing of the co-extruded rods demonstrated a nearly linear relationship between the maximum stress and average sleeve thickness. An 831 μm sleeve thickness of AA7090 increased the maximum strength by 259 MPa maximum stress maintained. In comparison, the tensile strength of the AA6082 core material was 200 MPa. The co-extruded rods with AA7090-Sc as the sleeve material displayed improved toughness compared to those with AA7090 as the sleeve.

Co-extrusion of AA7090/AA7090-Sc and AA6082 shows promising results and may provide a potential solution to creating composite metals having attractive mechanical properties at an affordable cost.

Sammendrag

Utvikling og implementering av materialer med kombinasjoner av mekaniske egenskaper, som f.eks. høy styrke og duktilitet, har vært av stor interesse i det materialtekniske miljøet de siste årene. I den økende jakten på miljøvennlig energi og redusering av utslipp, så er implementeringen av lettere metaller som aluminium svært viktig.

Co-ekstrudering er en prosess som gjør det mulig å produsere lette komponenter med kombinasjoner av gode mekaniske egenskaper ved lave kostnader. I dette prosjektet var målet å produsere to typer hybridmaterialer med et yttersjikt med høy styrke av enten AA7090 eller AA7090 tilsatt med Sc. Kjernen består av en AA6082 legering for å opprettholde høy duktilitet. Yttersjiktet av AA7090/AA7090-Sc ble hurtigstørknet ved hjelp av smeltespinning for å oppnå unike egenskaper uoppnåelig av vanlige støping. Det co-ekstruderte staget hadde en diameter på 12 mm og oppnådde utmerket metallurgisk binding mellom de to forskjellige legeringene.

Herdbarheten til de to forskjellige legeringene ble studert. Etter innherding på 470°C og utherding ved 140°C i 8 timer oppnådde yttersjiktet av hurtigstørknet AA7090 og AA7090-Sc en hardhet på henholdsvis 216 HV1 og 210 HV1. Mens hardheten i kjernen av AA6082 ble målt til omtrent 45 HV1. Karakterisering av mikrostrukturen etter innherding viste at yttersjiktet av AA7090 som var tilsatt Sc hadde oppnådd økt motstand mot rekrystallisering. Strekktesting av de co-ekstruderte stagene viste at det var en nær lineær sammenheng mellom maksimum spenning og gjennomsnittlig tykkelse på yttersjiktet. Et yttersjikt med tykkelse på 831 μm oppnådde en styrke på 259 MPa før brudd. Til sammenlikning ble strekkfastheten til kjernematerialet AA6082 målt til 200 MPa. Det co-ekstruderte staget med AA7090-Sc som yttersjikt viste en økning i seighet sammenliknet med det som hadde AA7090 som yttersjikt.

Co-ekstrudering av AA7090/AA7090-Sc og AA6082 viste lovende resultater og kan være en mulig løsning for å lage kompositttmetaller med kombinasjoner av mekaniske egenskaper ved lave kostnader.

Table of Contents

1 Introduction

In the growing demand for green energy, weight reduction is a great factor to reduce emissions. Greenhouse gases from vehicles, which is a main cause of pollution in cities, contributed to 70% of the total greenhouse gas emission in Europe in 2014 [1]. The introduction and implementation of lighter metals, such as aluminium, is therefore inevitable. In order to accomplish this, it's impotent to take into account the two equally important motivations [2]: Affordability and life cycle impact minimization. Implementation of lightweight constructions and components have become important for several industries, which can be seen in the aerospace industry through e.g. NASA [3] and the automotive industry through EU projects like 'Super Light Car' [4] and ENLIGHT [2]. M. Kleiner et al. [5] defined lightweight construction as: "An integrative construction technique using all available means from the field of design, material science, and manufacturing in a combined way to reduce the mass of a whole structure and its single elements while at the same time the functional quality is increased". On the other hand, the reduction of constructions weight does not always justify the increased cost associated with the use of more sophisticated processes and materials. Development of new materials and manufacturing technologies have therefore become crucial in order to reduce cost, emissions and depletion of the earth's natural re-sources [2, 1].

In recent years the advancement of polymeric composites materials have challenged metals when it comes to engineering applications due to their high strength/weight and stiffness/weight ratios [6]. The Boeing 787 Dreamliner, one of the most fuel-efficient airliners in the world, was built with 50% of the weight consisting of carbon fibre-reinforced polymeric composites, hence replacing the use of more traditional metals. But due to the metals unique abilities when it comes to high-temperature properties, fracture toughness and recyclability, they will remain irreplaceable for many applications. As stated by K. Lu [6]: "Modern technologies not only strongly rely on these unique properties of metals, but urgently call for even better metals. Increasing the strength of metals without sacrificing other properties is critical for their competitiveness".

Aluminium is a metal that is widely used in many engineering applications. Aluminium alloys, especially those in the 7xxx series, have been applied in the aerospace industry for centuries because of their high strength and low weight. The strength of these alloys has come to the level of many steels but with just 1/3 the weight [7]. This has been done by controlling the microstructure and precipitation hardening. But these alloys are often relatively expensive as they contain lots of expensive alloying elements and due to their increase in strength, they also become more brittle as these properties are usually mutually exclusive [8]. There are many alternative methods available for solving these problems. A possible solution to

the problem at hand is the use of a technique called co-extrusion. Through this technique it's possible to produce a hybrid material with combination the mechanical properties, while at the same time reducing cost.

In this project, one aluminium alloy of AA7090 and one AA7090 with additions of scandium (Sc) have been rapidly solidified by melt spinning, cold compacted and co-extruded as the sleeve together with an AA6082 alloy as the core material. The microstructure of this hybrid material has been characterized and the thickness of the sleeve material throughout the co-extruded rods have been measured. In order to investigate the response to precipitation hardening of these two dissimilar materials, a precipitation hardening curve was made. With the objective to find the mechanical properties of the co-extruded rods, a tensile test was performed. Deformation behaviour was analyzed using digital image correlation (DIC) during the tensile testing. Afterwards, the fractured specimens were investigated in the scanning electron microscope (SEM) with a special interest in the interface between the two dissimilar alloys.

2 Theory

2.1 Aluminium and Aluminium Alloys

In the following chapter, some general information about aluminium will be presented and two series aluminum alloys will be discussed. The difference in mechanical properties and how these alloys achieve them will also be presented.

2.1.1 Aluminium in General

Aluminium is known for its low density (2.7 g/cm^3), corrosion resistance and high thermal- and electrical conductivity [7]. Aluminium is produced by electrolysis of Al_2O_3, which again is produced by bauxite [9]. The mechanical properties of pure aluminium are relatively poor and it has a relatively low melting temperature of only $660°C$. As opposed to many steels, aluminium has no ductile-brittle transition due to its FCC structure [7]. This allows the aluminium to maintain its ductility at lower temperatures. By alloying or cold work, the mechanical properties can be increased to that of many structural steels, with just 1/3 of the weight [9].

Aluminium alloys are generally classified as either cast or wrought and by the main alloying element, as shown in table 2.1.

Table 2.1: *Classification of aluminium alloys [9].*

Cast		**Wrought**	
Alloy	**Main alloying element**	**Alloy**	**Main alloying element**
1xx	Al $\geq$ 99.00%	1xxx	Al $\geq$ 99.00%
2xx	Cu	2xxx	Cu
3xx	Si with some Cu and/or Mg	3xxx	Mn
4xx	Si	4xxx	Si
5xx	Mg	5xxx	Mg
6xx	Zn	6xxx	Mg and Si
7xx	Sn	7xxx	Zn
8xx	Other elements	8xxx	Other elements

2.1.2 Aluminium-Magnesium-Silicon Alloys

Al-Mg-Si alloys, also known as 6xxx alloys, are aluminium alloys that have a wide area of applications, often used as extruded profiles in the building- and automotive industry [10]. Half of the aluminium profiles produced worldwide are profiles from the 6xxx alloys [9]. The reason for their widespread use is the combination of relatively high strength and formability, as well as excellent corrosion resistance

in all natural atmospheres. Their major alloying elements are Mg and Si, which typically added in the area of 0.5 - 1.3% and 0.4 - 1.4%, respectively. Small amounts of Mn, Cr and Cu are also added to further improve the mechanical properties. The yield strength (σ_{YS}) and ductility of these alloys are typically in the range 190 - 360 MPa and 17 - 12%.

The 6xxx alloys are classified as wrought alloys, due to the fact that their mechanical properties are mainly determined by precipitation [9]. Even though there is a relatively low solubility of Mg and Si in the Al matrix, these elements provide a significant hardening effect when precipitated as the coherent and semi-coherent phases of Mg_2Si during ageing [11]. The precipitation sequence in 6xxx alloys is typically:

$$solid - solution(\alpha) \rightarrow GP - zones \rightarrow \beta'' \rightarrow \beta' \rightarrow \beta(Mg_2Si)$$

The coherent and semi-coherent GP-zones and β'' are considered the most efficient hardening precipitates, but maximum hardness is achieved through a structure with a combination of β'' and β' [11]. A typical heat treatment process to achieve maximum strength (T6) in an extruded rod of a 6xxx alloy can be the following [12]: Solution heat treatment at $520°C$, quenching and precipitation heat treatment at $175°C$ for 8 hours.

2.1.3 Aluminium-Zinc-Magnesium-Copper Alloys

The Al-Zn-Mg-Cu alloys, also known as 7xxx alloys, are high strength aluminium alloys often used in military equipment and in the aerospace industry [13]. The 7xxx alloys are also classified as wrought alloys and depend mainly on precipitation hardening to get their high strength. Through rapid solidification and alloying with Ni and Zr it's possible to achieve σ_{YS} above 750 MPa, but these alloys are brittle with a ductility of only 5% [9].

For some high strength Al-Zn-Mg-Cu alloys containing less than 1% Cu, it's possible to use the basic Al-Zn-Mg phase diagram, with some restrictions, to understand some of the thermodynamics regarding these alloys [14]. As seen in figure 2.1, the solubility of Zn and Mg in Al decreases with temperature, so during solidification these elements will precipitate into phases like $Al_2Mg3Zn3$(T-phase) and $MgZn_2$ (η/M-phase). These phases will later contribute to precipitation hardening in these alloys. The alloys in the 7xxx series that has the highest strength normally contain 8-10% Zn and 3-4% Mg, but these alloys are susceptible to stress corrosion.

With the addition of Cu, the phase diagram of the Al-Zn-Mg-Cu will be a combination of the Al-Zn-Mg- and Al-Cu-Mg-phase diagrams, as seen in figure 2.2 [14]. One key characteristic of this diagram is that there are three phases in the

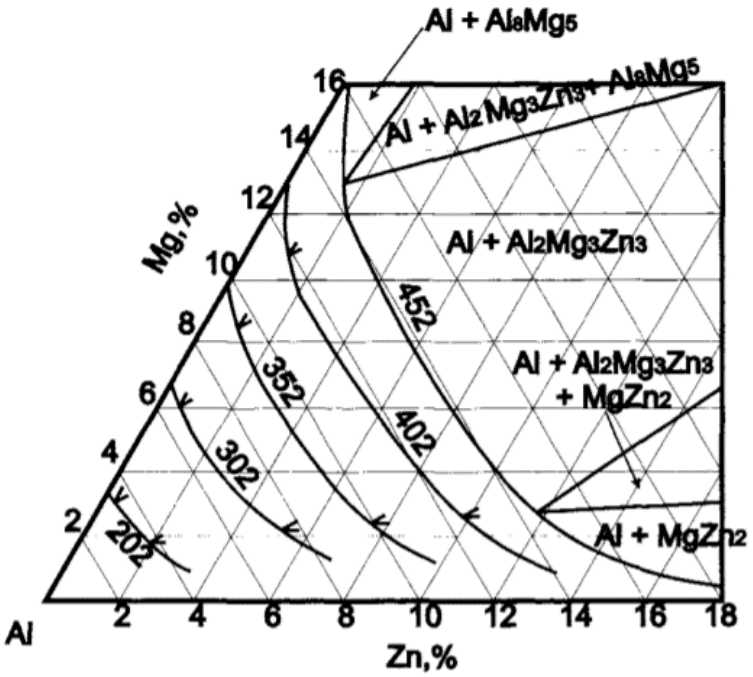

Figure 2.1: *Phase diagram of the Al-Zn-Mg system in the Al rich part. Shows the solid solubility of Zn and Mg at different temperatures [14].*

.

Al-Zn-Mg- and Al-Cu-Mg phase diagrams that are fully miscible with each other. These are Al_6CuMg_4-$Al_2Mg_3Zn_3$, $MgZn_2$-$AlCuMg$ and $Al_5Cu_6Mg_2$-Mg_2Zn_{11}, also known as T-, M- and Z-phase, respectively. Alloys in the 7xxx series are known to contain at least one of the two phases T or M. A normal precipitation sequence for the 7xxx alloys can be the following if M is the main precipitating phase [9]:

$$solid - solution(\alpha) \rightarrow GP - zones \rightarrow M^{'} \rightarrow M(MgZn_2)$$

Also here, the coherent and semi-coherent GP-zones and $M^{'}$ are the most efficient hardening precipitates [9]. One way to maximum strength(T6) for an extruded rod can be solution heat treatment at $465°C$, followed by quenching and precipitation heat treatment at $120°C$ for 24 hours [12]. A two- or three-stage precipitation heat treatment process at different temperature may also be used.

The high strength alloys in the 7xxx series do also contain some transition metals, e.g Cr, Ti, Mn and Zr, that will form fine dispersions within the grains and at the grain boundaries [13, 14]. These dispersions will restrict grain growth and recrystallization. Impurity elements like Si and Fe will cause the formation of Mg_2Si- and Al_3Fe-phases, reducing the properties of the alloy.

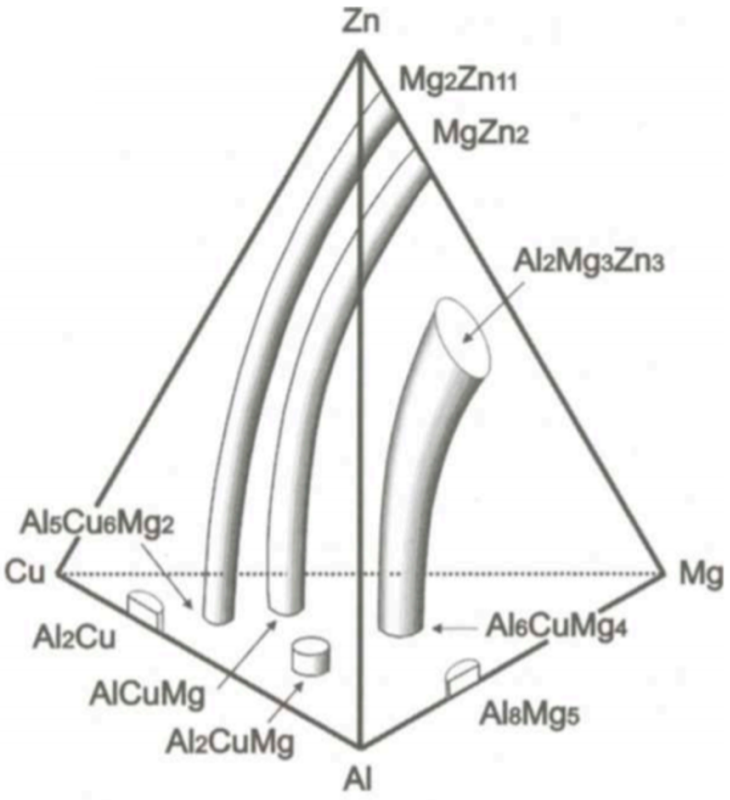

Figure 2.2: *3D-phase diagram of the Al-Zn-Mg-Cu system in the Al rich part [14].*

2.2 Rapid Solidification

In the following chapters, some general principles with regards to the concept of solidification of metals will be discussed and connected to the idea of rapid solidification and how this affects the physical and chemical properties of a metal.

2.2.1 Concept of Solidification

Solidification is the phase transformation when a material becomes solid [15]. By controlling the extraction of heat in a melt, it's possible to influence the microstructure and improve quality of the material. Defects created during solidification are difficult to eliminate and will remain even after heavy deformation, influencing the final product [16].

If the temperature of a molten metal is reduced to a temperature below the liquidus temperature, the most thermodynamically stable form of the metal is solid and the transformation from liquid to solid starts [17]. The rate at which this transformation occurs depends mainly on the heat extraction rate. The heat extraction affects the driving force for nucleation (ΔG) and the growth of crystals.

Heat extraction is often expressed as the cooling rate, dT/dt. The process by which a steel ingot is made in a mould is considered the conventional way of

solidification [15]. By using this technique it's possible to achieve cooling rates ranging from 10^{-1} to 10^{-6} $°C/s$, depending on the size and material of the mould. In an ingot like this three different solidification zones can be observed, as seen in figure 2.3. At the interface between the mould and melt, the cooling rate is relatively high due to the low temperature of the mould [16]. This creates an outer zone with many small equiaxed grains. Some of these grains will continue to grow in an elongated order due to the temperature of the melt, leading to the formation of a characteristic columnar zone. After some time, new grains will start to nucleate independently inside the melt and grow into equiaxed grains. This zone is called the inner equiaxed zone. If there are particles present in the melt that can act as nucleation sites for new grains, a structure with fine equiaxed grains throughout the cast may be achieved [17].

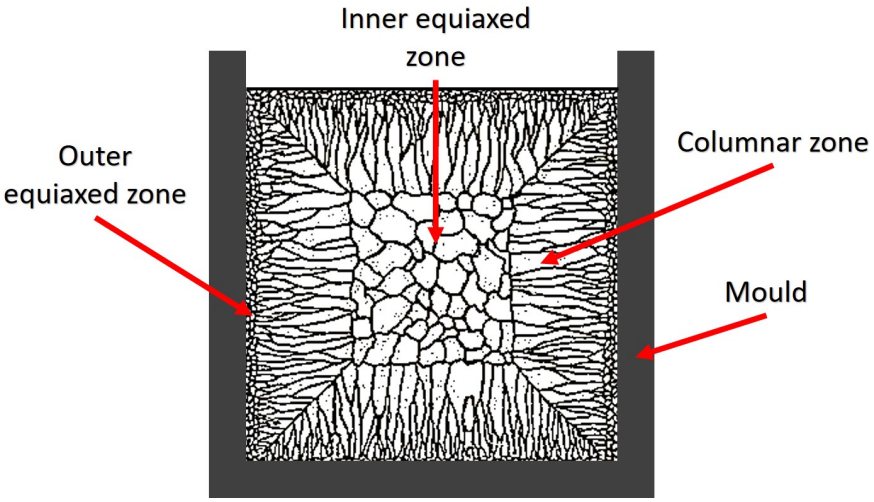

Figure 2.3: *Schematic representation of the structures achieved during stationary mould casting [16].*

There are many ways of influencing the properties gained through the solidification process. Some ways of achieving the desired properties of the as-cast structure are e.g. through the selection of a suitable casting method and chemical composition of the melt.

2.2.2 Rapid Solidification and Melt Spinning

In order to get better control of the solidification process and improved properties of metals, a lot of effort has been put into the development of techniques that can achieve rapidly solidified alloys. These techniques are able to achieve cooling rates typically in the range of 10^4 $°C/s$ to 10^9 $°C/s$ [18]. The high cooling rates cause solute trapping due to the fact that the solute atoms do not have time to rearrange themselves in the material [16]. This will result in the formation phases that are

outside their equilibrium, as well as refinement of the microstructure and reducing the amount of segregations [15, 13].

For aluminium alloys, this allows for unusual alloying due to the extension of the solubility of various alloying elements, as seen in table 2.2 [18]. This is especially beneficial when it comes to the major impurities, Si and Fe, in the aluminium alloys in the 7xxx-series [14]. These elements form inclusions that often has weak cohesion with the Al-matrix [19]. Cracks easily can nucleate and propagate along these inclusions under loading, reducing the mechanical properties. Through the rapid solidification techniques, it's possible to make materials with unique properties unattainable by conventional casting methods.

Table 2.2: *Extension of the maximum solubility of elements in solid solution of binary aluminium alloys due to rapid solidification [18].*

Elements	**Equilibrium Solubility [wt%]**	**Extended Solubility [wt%]**
Mg	17.35	34.6 - 37.5
Cu	5.7	15.1 - 17.0
Si	1.65	10.4 - 16.5
Mn	1.42	11.5 - 16.8
Cr	0.84	9.2 - 11.0
Ti	0.27	0.4 - 3.5
Zr	0.28	3.8 - 4.9
Fe	0.05	7.9 - 11.7
Ni	0.05	2.6 - 15.4

One technique for obtaining rapid solidification is called melt spinning and can achieve cooling rates between $10^4 - 10^7\ ^\circ C\ s^{-1}$. Melt spinning is classified as a non-conventional forming process and has the ability to produce a large amount of rapidly solidified material with unique properties [20].

Melt spinning is done by putting the metal in a crucible and melted, often by using induction as seen in figure 2.4 [21]. There is a small hole in the bottom of the crucible, but the capillary effect keeps it from flowing out of it. When the melt comes to the desired temperature, a pressure is introduced from above by the use of Ar-gas. The molten alloy will solidify when it hits the rotating wheel, often made of copper and water-cooled [15]. Ribbons with thickness around 100 μm, or even lower depending on the cooling rate, can be made. The cooling rate is again dependent on the speed of the wheel. The ribbons are then cut into smaller flakes and compacted into billets, which then can follow the normal procedure of extrusion.

For some 7xxx alloys, it's possible to produce a structure with equiaxed grains with diameter below 50 μm. This is finer than the as-cast microstructure that has

grains larger than 100 μm [22].

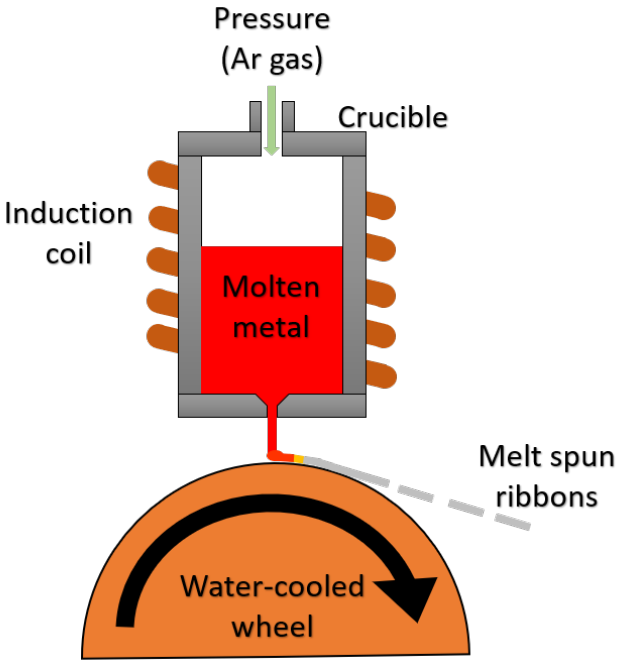

Figure 2.4: *Schematic representation of the melt spinning process [23].*

2.3 Co-Extrusion

In the following chapter the concept of extrusion and co-extrusion will be presented, as well as the important process parameter that may influence the quality of the end product.

2.3.1 Concept of Extrusion

The definition of extrusion is when a block of metal, a billet, is forced to flow through a die with a ram, as shown in figure 2.5 [24]. The die has a smaller cross-section than the original billet and creates the shape of the finished product. The extrusion process can be done either hot or cold depending on the method and the material being extruded.

For aluminium there are two common types of extrusion: direct- and indirect extrusion [24]. The conventional and most used method is direct extrusion, which is the one illustrated in figure 2.5. The main difference between the two methods is that for direct extrusion the ram forces the billet through the die, but for indirect extrusion the die moves.

It's possible to influence the mechanical properties of the finished product by controlling the metal flow during the extrusion [24]. Type of extrusion, the design of the die, extrusion speed and temperature of the billet, container and die are a

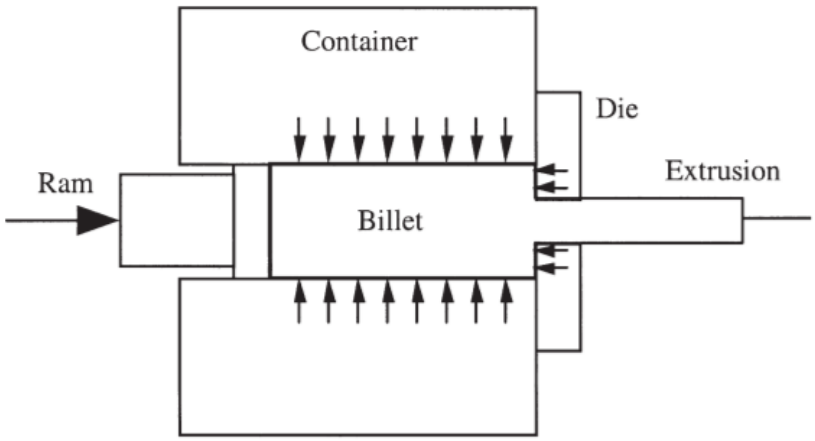

Figure 2.5: *Schematic representation of the direct extrusion process [24].*

few of the factors that can affect the metal flow. The extrusion speed is dependent on the extrusion ratio and ram speed and can be calculated from equation 1.

$$Extrusion\ Speed\ [m/min] = \frac{A_0}{A_f} \times V_R \times \frac{60}{1000} \tag{1}$$

where A_0/A_f is the extrusion ratio(A_0=cross-section area of billet and A_f=cross section area of final product), V_R is the ram speed given in mm/s and 60/1000 converts from mm/s to m/min.

2.3.2 Co-extrusion

The co-extrusion process creates a hybrid billet by extruding two or more materials into one single billet with a sleeve and a core, as seen in figure 2.6 [25, 26]. By using this method it's possible to make materials with combinations of mechanical properties that a single metal material cannot achieve, e.g. high strength and ductility, while at the same time reducing weight and cost [27]. The quality of the end product is really sensitive to the co-extrusion parameters [25]. The high pressure and temperature during the co-extrusion make the metals metallurgically bonded, but may also cause cracking. The geometry of the die and extrusion speed are also important to create a uniform sleeve and core thickness and to make them bond well together.

While working with co-extruding of unequal-strength metals it's important to understand how the different co-extrusion parameters influence the plastic flow [28]. There has to be relatively low external contact friction in extrusion container and high internal friction between the core and sleeve material, to avoid turbulent plastic flow and uneven sleeve/core thickness. The relationship between the strength and volume ratio of sleeve and core material greatly influences the plastic flow. A soft

sleeve and hard core will not create any uneven flow velocities in the system, but a hard sleeve and soft core may cause difficulties. The hard sleeve will cramp the flow in the centre, increasing the flow velocity of the softer core material. To better control this, it's important to choose a die shape with optimal die angle. It should be noted that the optimal die angel for normal extrusion may not necessarily be the same as for co-extrusion.

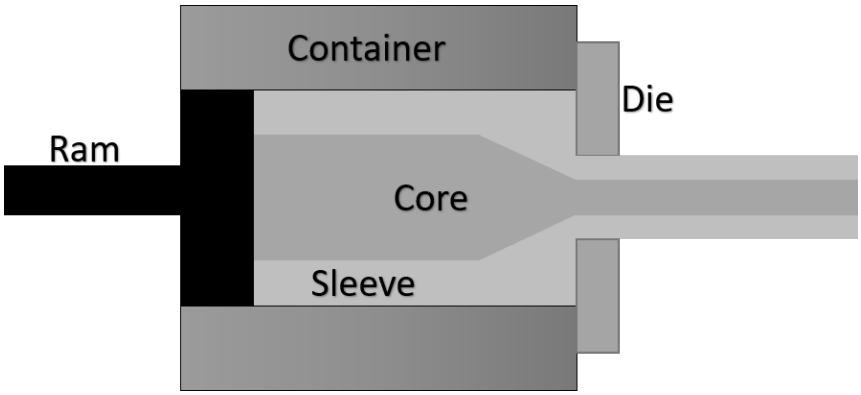

Figure 2.6: *Schematic representation of the co-extrusion process [29].*

2.4 Mechanical and Physical Properties of Metals

In the following chapter, the main strengthening mechanisms for aluminium and aluminium alloys are presented and examples of how some of these mechanical properties are measured.

2.4.1 Strengthening Mechanisms for Aluminium Alloys

Plastic deformation occurs when there is movement of many dislocations. To improve the strength of an aluminium alloy one must reduce the mobility of these dislocations [7]. There are four main types of strengthening techniques used for aluminium:

- Grain size reduction
- Strain hardening
- Solid-solution hardening
- Precipitation hardening

Grain size reduction

When a material has a fine grain structure it has higher strength and toughness than if it had a coarser grain structure [7]. This is due to the increasing amount of grain

boundaries. Two grains, sharing a common grain boundary, often have a different crystallographic orientation. This difference in orientation makes it difficult for a dislocation to move between the two grains because it has to change direction when crossing the grain boundary. Generally, the larger the misorientation, the more difficult the dislocation movement becomes. The Hall-Petch relationship (equation 2) is often used to describe the correlation between the grain size and the yield strength(σ_{YS}) of a material.

$$\sigma_{YS} = \sigma_0 + k_y d^{-1/2} \tag{2}$$

In this equation d is the average grain diameter and both σ_0 and k_y are material specific constants [7]. The grain size of a material can be regulated by controlling the solidification process and by heat treatment after plastic deformation.

Strain hardening

Strain hardening, often called work hardening, is one of the most commonly used methods of increasing the mechanical properties of a metal in the fabrication industry [7]. This technique is based on the increased dislocation density caused by plastic deformation. Two dislocations normally have a repulsive force between each other, so the motion of one is hindered by the other. When the dislocation density increases, the mobility of dislocations are reduced and the strength and hardness improve.

Solid-solution hardening

By introducing alloying elements to a metal, they will either go into substitutional or interstitial solid solution [7]. These impurity atoms will cause strains in the crystal lattice, compressive strain if the atom is larger than the host atom or tensile strain if it's smaller than the host atom. The impurity atoms tend to move to where they will neutralize the strains caused by dislocations, which again will reduce the mobility of the dislocation and increase the strength and hardness of the metal.

Precipitation hardening

Precipitation hardening is done over three stages to get particles in the original phase. The three stages are solution heat treatment followed by quenching and precipitation heat treatment as shown in figure 2.7 [7]. The first stage, the solution heat treatment is done by heating the alloy to T_0, which is above the solvus line in the hypothetical phase diagram of A and B as seen in figure 2.8. The temperature is kept until all of the β-phase and other phases are dissolved in the α-phase. When this happens, one will get a pure α-phase with a concentration C_0 of B.

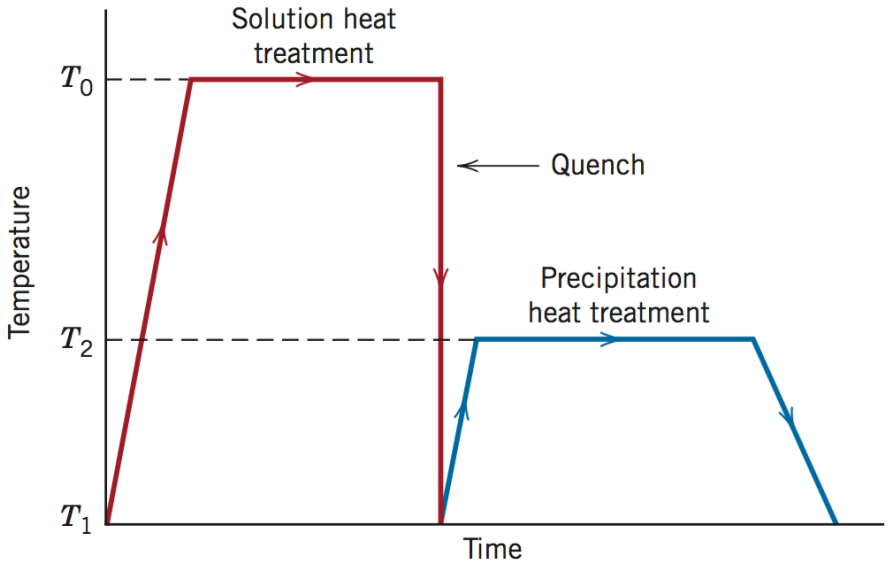

Figure 2.7: *Precipitate hardening steps [7].*

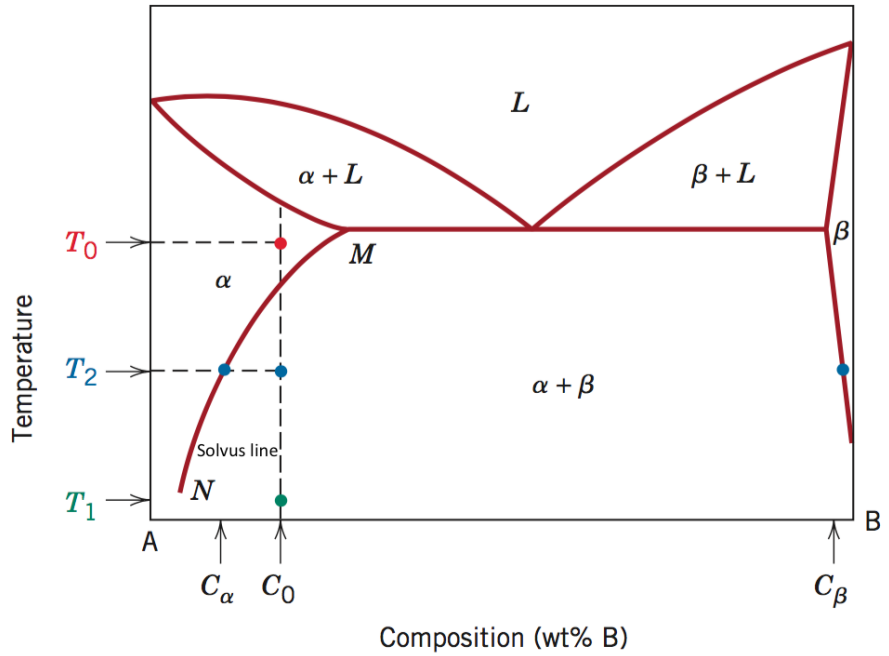

Figure 2.8: *Precipitate hardening hypothetical phase diagram of A and B [7].*

If the alloy were to be cooled slowly from T_0, there will be formed β again [9]. After the solution heat treatment, the alloy will be quenched to T_1, preventing the formation of the β-phase. This will create a situation where the α-phase will be supersaturated with B-atoms [7]. Some alloys can experience diffusion at this low temperature, this is known as natural ageing [30].

But some alloys may be stable at T_1 due to the low diffusion rate and require

further heat treatment for precipitates to form, also known as artificial ageing [30]. The alloy is heated to T_2, which is in the $\alpha + \beta$ area of the phase diagram (see figure 2.8) [7]. At this temperature, the diffusion rate increases and the β-phase precipitates as finely, distributed particles. This process depends on both temperature(T_2) and the time it's kept at this temperature(ageing time) when it comes to the strength and hardness of the end product, as seen in figure 2.9. This figure shows a schematic diagram of an aluminium-copper alloy, which precipitates a θ-phase($CuAl_2$). The type of precipitate depends on the alloy composition.

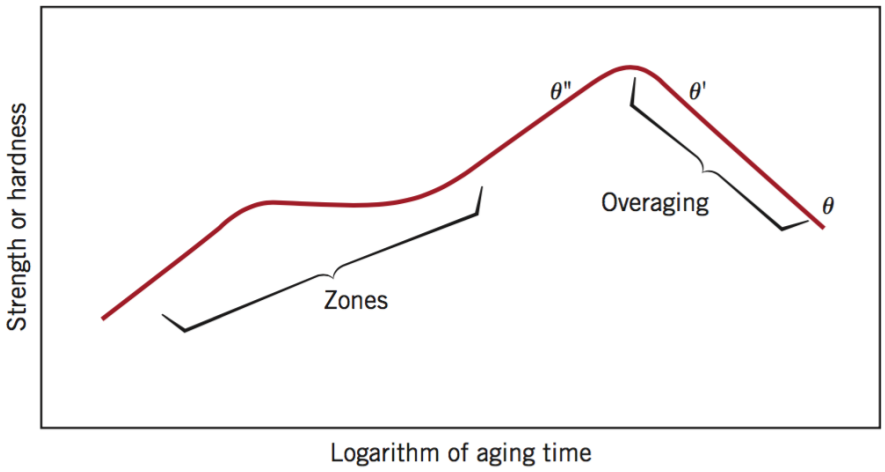

Figure 2.9: *Schematic diagram of the strength and hardness as a function of aging time at T_2 [7].*

The heat treatment process passes several stages when forming the precipitates which affect the mechanical properties in different ways:

$$solid - solution(\alpha) \rightarrow GP - zones \rightarrow \theta'' \rightarrow \theta' \rightarrow \theta$$

The supersaturated α-phase is heated and the B atoms will start to form small discs, only a few atoms thick, also known as Guiner-Preson-zones(GP-zones) [7]. With time, more and more atoms will diffuse to these GP-zones and the strength of the alloy increases as a function of the size of these zones. At some point the GP-zones will become particles, which will later turn into the transition phases θ''. This precipitate particle will be the one that gives the maximum strength and can be preserved by cooling the alloy to room temperature. If the alloy furthered heated, the θ'' will transform into θ' and then the equilibrium phase θ. This is called overageing and will reduce the strength of the alloy as seen in figure 2.9. Strong bonding of these phases to the matrix and coherency with the lattice is important for the strength, as well as shape, size, distribution and spacing of the precipitate [13].

The combination of strain- and precipitation hardening are often used to achieve maximum strength in many metals. This is done by strain hardening after the quenching step and before the precipitation heat treatment [7]. The precipitation process will be accelerated, and the distribution of the precipitates are improved [13].

2.4.2 Stress-Strain Behavior of Metals

One common way of finding some of the key mechanical properties of a material is by doing a stress-strain test [7]. The material is machined into either a flat or a circular specimen, with a section with a reduced cross-section in the middle. The reduced cross section is done to better control where the fracture will occur. The specimen is mounted in a tensile-testing apparatus that elongates it with a constant rate. The applied load (F) and resulting elongation are continuously measured all the way till the specimen fractures.

The load and elongations measured depend on the size of the specimen [7]. To get comparable parameters not dependent of geometry, the load and elongation are converted into engineering stress(equation 3) and engineering strain(equation 4), respectively. This is normally done by the apparatus itself and a stress-strain curve is created. A schematic presentation of a typical stress-strain curve is shown in figure 2.10.

$$\sigma = \frac{F}{A_0} \tag{3}$$

$$\epsilon = \frac{l_i - l_0}{l_0} = \frac{\Delta l}{l_0} \tag{4}$$

where A_0 and l_0 is the cross-sectional area and length of the specimen before it's loaded, l_i is the length when loaded and Δl is the change in length $(l_i - l_0)$ [7]. The unit of σ is MPa and ϵ is unitless, but it's often given in percentage.

Deformation of a material where the stress and strain a proportional is known as elastic deformation and is illustrated in figure 2.10 [7]. In this area, the deformation will not be permanent and the specimen will return to its original shape when unloaded. From this linear part of the curve, the modulus of elasticity (Young's modulus or E-module) can be calculated as the slope of the line by Hooke's law(equation 5). The E-module can be seen as the materials stiffness or resistance elastic deformation.

$$E = \frac{\Delta\sigma}{\Delta\epsilon} \tag{5}$$

where $\Delta\sigma$ and $\Delta\epsilon$ can be found as shown in figure 2.10.

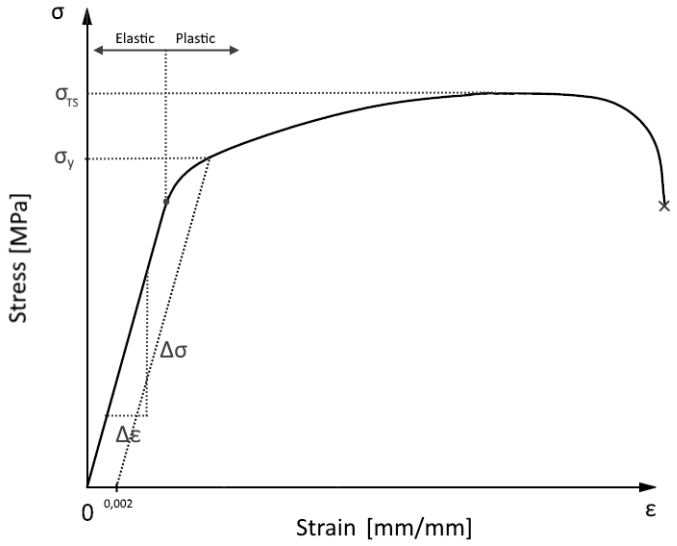

Figure 2.10: *Schematic presentation of a typical nominal stress-strain curve for a material that has been stressed until fracture. The figure shows how the E-module, yield strength(σ_{YS}) and tensile strength(σ_{TS}) are found, as well as the elastic- and plastic area.*

In the transition between the elastic and plastic area, Hooke's law ceases to be valid and the specimen starts to become permanently deformed. The material starts to yield [7]. In many cases, a component is considered defective if it's permanently deformed. That's why it's essential to know at which stress this yielding occurs. This mechanical property is known as yield strength (σ_{YS}). The σ_{YS} often found by creating a line that is parallel to the linear part of the curve and displacing it 0.002 along the strain axis as shown in figure 2.10. During further deformation into the plastic area, the stress reaches a maximum also known as tensile strength (σ_{TS}) [7]. The specimen begins to form necking and strain rapidly increases, stress declines and fracture occurs, as shown in figure 2.10.

Another important mechanical property that can be found by a stress-strain test is the ductility [7]. Ductility indicates how much the material plastically deforms before it fractures and is measured either by per cent elongation or per cent reduction in area. A material is considered brittle when the strain at which it fractures is lower than 5%.

2.4.3 Hardness

A material's ability to resist local plastic deformation is defined as the materials hardness [7]. There are several methods for measuring hardness. Common for them all is that an indenter, often a diamond, is forced into the specimen at a pre-set load. The indent in the specimen is measured by a microscope and the hardness is

calculated as a function of the size of the indent and the load. The standard way of stating the hardness is in Vickers, Rockwell and Brinell depending on the material and the specimen size.

For hardness measurements using Vickers method, a square-based pyramid with an angle of 136° between the oppositely facing sides is indented into the specimen [31]. By using the load and the projected area that the indentation creates it's possible to calculate the pressure (p) over the indentation by using equation 6.

$$p = \frac{Load}{Projected\ area\ of\ indentation} \tag{6}$$

For many metals, there is a relation between the hardness and the σ_{YS} of metal. This is given in equation 7 [31]. This equation is in most cases true but becomes less accurate when the relationship E/σ_{YS} gets below 100.

$$\sigma_{YS} = \frac{1}{3} \times p \tag{7}$$

3 Experimental Procedures

3.1 Materials and Melt Spinning

The aluminium alloys used to create the sleeve material were an AA7090 billet and an AA7090 alloy with additions of Sc, hereby referred to as AA7090-Sc. The alloy intended as the core material was an AA6082 alloy, while direct chill (DC) cast AA7090 was used as a reference. The chemical composition of these alloys can be seen in table 3.1. The chemical analysis was done by SINTEF Raufoss Manufacturing, who used a spectrograph for all alloys. Except for RS AA7090-Sc, that had to be taken to the SEM and chemical analysis had to be done by EDS X-ray.

Table 3.1: *Chemical composition of the aluminium alloys provided by SINTEF Raufoss Manufacturing. Shows only the amount of alloying elements added, the rest is Al. Alloys marked with RS is the alloys intended for rapid solidification.*

		Alloy			
		RS AA7090	RS AA7090-Sc	DC AA7090	AA6082
Alloying elements [wt%]	Zn	8.511	9.34	8.807	0.118
	Mg	2.926	2.71	2.927	0.665
	Cu	0.468	0.50	0.478	0.064
	Cr	0.184	0.21	0.184	0.018
	Fe	0.096		0.046	0.217
	Zr	0.089	0.17	0.093	-
	Si	0.055		0.034	0.935
	Sc	-	0.18	-	-
	Ti	0.012		0.006	0.014
	Ni	0.007		0.003	0.001
	Mn	0.0014		-	0.541

Billets of AA7090 and AA7090-Sc were cut into two bolts of AA7090 and two bolts of AA7090-Sc, each bolt with a weight of approximately 1 kg. These billets were remelted and melt spun, in a modified melt spinner at NTNU. The bolts were melted at a temperature of 720°C with an Ar-gas to avoid oxidation. The molten metal was rapidly solidified at a water-cooled copper wheel, rotating at 500 rpm during the solidification. With a diameter of 25 cm, this equals a linear velocity of approximately 6.5 m/s on the surface of the wheel. Four different batches of melt-spun ribbons were produced: AA7090 batch 1 and batch 2 and AA7090-Sc batch 1 and batch 2. These ribbons were cut into smaller flakes at NTNU, in

preparation for compacting. The production and examination of the melt spun ribbons were done in previous work [32].

3.2 Compaction of Ribbons

The compacting of the ribbons was done at Strecon in Denmark. A schematic image of how the compaction process was done can be seen in figure 3.1. The diameter of the container was 60.3 mm and the initial diameter and wall thickness of the steel pipe were 60 mm and 6.7 mm, respectively. Images of the steel pipes can be seen in figure 3.2a. This left an empty cylindrical volume where the ribbons were filled into with a diameter of approximately 47 mm. The steel pipe with the ribbons inside was compacted with a load of approximately 490 tons, producing a billet with a steel sleeve and aluminium core, as seen in figure 3.2b. This setup causes the ribbons to be compacted from both the vertical and horizontal direction, ensuring uniform compaction throughout the billet and a density close to the theoretical density. Four billets were made of ribbons from AA7090 batch 1, AA7090 batch 2, AA7090-Sc batch 1 and AA7090-Sc batch 2, hereby referred to R1, R2, R3 and R4, respectively. The steel sleeve was later removed by machining.

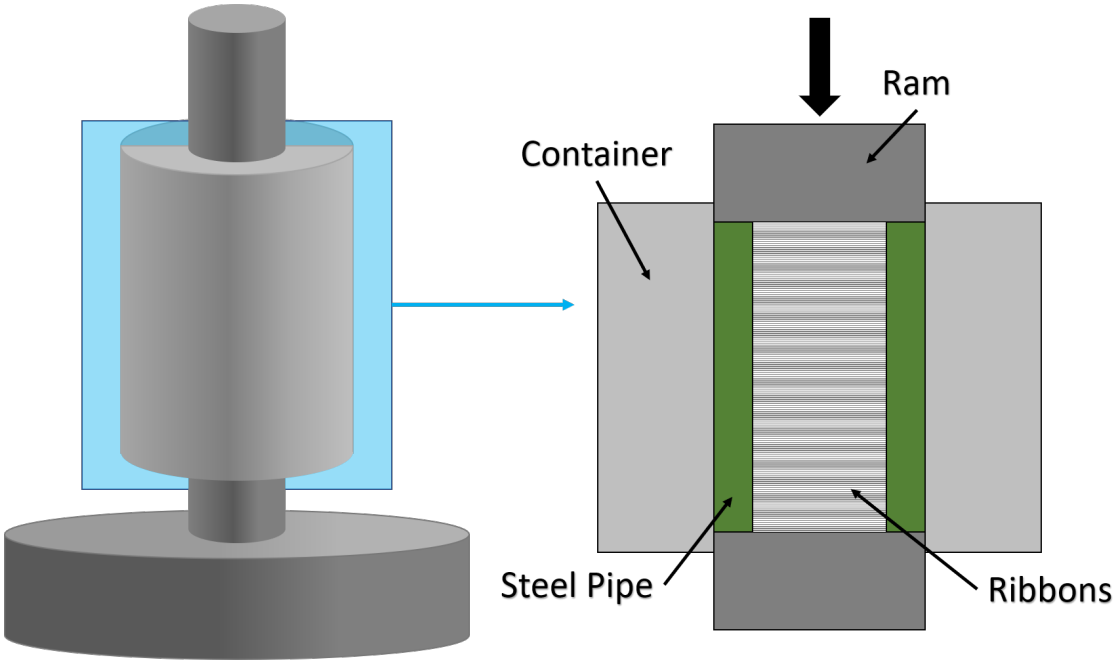

Figure 3.1: *Schematic representation of the compacting process.*

(a) Steel pipes. *(b) Compacted billet.*

Figure 3.2: *Images of* ***(a)*** *the steel pipes used during compaction and* ***(b)*** *a compacted billet with a steel sleeve and aluminium core.*

3.3 Co-extrusion

The co-extrusion process was performed at SINTEF Raufoss Manufacturing. The setup for the co-extrusion can be seen in figure 3.3, where the core material was AA6082 and the sleeve material was the rapidly solidified and compacted AA7090 alloys. A small guide pin was made on the core material to guide it between the hard sleeve material during the co-extrusion. An image of one of the machined billets can be seen in figure 3.4. The compacted billets R1, R2, R3 and R4 were machined according to the dimension seen in figure 3.3 and the final height, diameter and weight of each part can be seen in table 3.2. Due to the little amount of aluminium in R1, it was not possible to produce a billet with a diameter of 40 mm.

Table 3.2: *Dimensions of the machined and cut compacted billets of the AA7090 materials.*

Part	**Height** [mm]	**Diameter**[mm]	**Weight** [g]
R1 Part 1	105	35	284
R2 Part 1	40	40	112
R2 Part 2	40	40	116
R3 Part 1	38	40	118
R3 Part 2	40	40	120
R4 Part 1	41	40	126
R4 Part 2	40	40	120

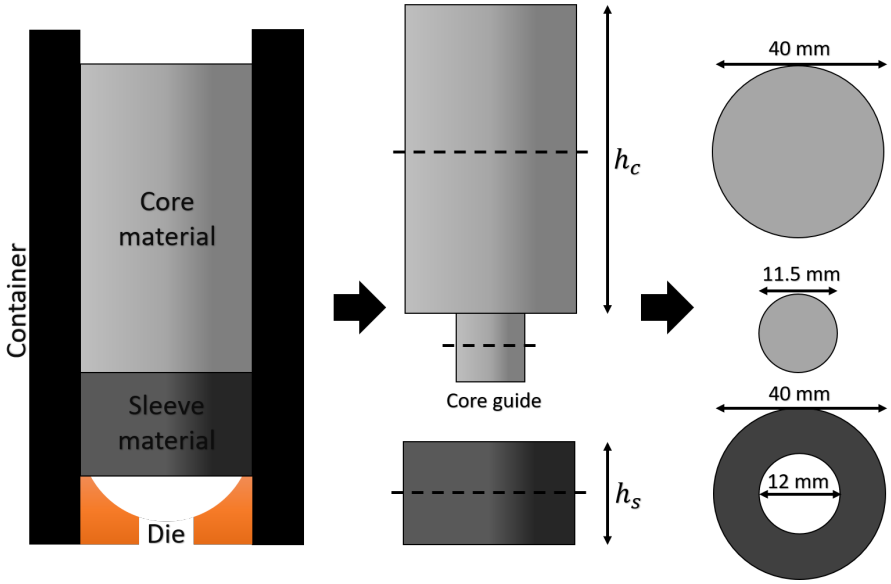

Figure 3.3: *Illustration of the dimension used for the co-extrusion process where h_s is the initial height of the sleeve material, h_c is the initial height of the core.*

(a) *Machined core and sleeve billets.*

(b) *Sleeve billet on top of the core billet.*

Figure 3.4: *Image of* ***(a)*** *the machined AA6082 core billet and AA7090 sleeve billet and* ***(b)*** *how they are mounted together.*

The goal was to produce a rod of each of the materials with approximately equal weight difference between the core and sleeve material. The weights and other parameters used during these co-extrusion trials can be seen in table 3.3. The billets for the core and sleeve material was pre-heated (PH) in an oven for at least 1 hour before the co-extrusion. The diameter of the container and die were 42 mm and 12

mm, respectively. This gives an extrusion ratio of 12.3. The same die geometry, as illustrated in figure 3.3, was used for all trials. The temperature of the billets, when loaded into the container, was also measured. As well as the container temperature, extrusion force, ram speed and exit temperature approximately 20 cm below the die were also recorded during each of the co-extrusion trials. Graphs of these recordings can be found in appendix A, but a summary of these values can be seen in table 3.4. Co-extrusion of rod R2 Part 1 and R4 Part 2 failed due to the material getting stuck at the beginning of the co-extrusion process. The other co-extrusion trials were a success, except for cracks at the end of the some of the rods.

Table 3.3: *Parameters for the co-extrusion trials.*

Rod	**Weight Sleeve** [g]	**Weight Core** [g]	**PH Temp.** [$°C$]	**Container Temp.** [$°C$]	**Ram Temp.** [$°C$]
R2 Part 1	112	448	465	460	401
R2 Part 2	116	448	472	450	375
R3 Part 1	126	447	472	440	306
R3 Part 2	120	446	472	460	307
R4 Part 1	126	447	472	460	347
R4 Part 2	120	448	472	460	266

Table 3.4: *Summary of recorded parameters for the co-extrusion trials.*

Rod	**Billet Temp.** [$°C$]	**Maximum Force** [Tons]	**Average Exit Temp.** [$°C$]	**Ram Speed** [mm/s]	**Extrusion Speed** [m/min]
R2 Part 1	449	170	-	-	-
R2 Part 2	452	70	397	0.41	0.30
R3 Part 1	450	80	399	0.44	0.32
R3 Part 2	453	69	405	0.40	0.29
R4 Part 1	452	73	399	0.35	0.26
R4 Part 2	456	120	-	-	-

Rather than using R1 directly for co-extrusion, it was extruded normally through the same die to produce a rod of uniform melt spun AA7090. This rod will hereby be referred to as RS AA7090. In addition, a rod of DC AA7090 was extruded via the same extrusion process. This rod was intended as a reference material. The graphs for their recorded parameters can be seen in appendix B.

3.4 Sample Preparation

In preparation for the different experimental examinations and characterizations, samples were cut using the Struers Labotom-15. For microstructural and hardness analysis, the samples were cut either in the transverse- or longitudinal cross-section. The different cross-sections are illustrated in figure 3.5.

When samples were grinded, they were grinded on SiC-papers with gradually finer grit size (P320 - P500 - P1200 - P4000). If samples had to be polished, this was done using a Struers Tegramin-30 with gradually finer polishing cloth and diamond solutions ($9\mu m$ - $3\mu m$ - $1\mu m$). In preparation for microstructural analysis in the optical microscope, samples were often anodized with 20V for 90 seconds in a solution containing 5% fluoroboric acid (HBF_4) holding 20 $°C$.

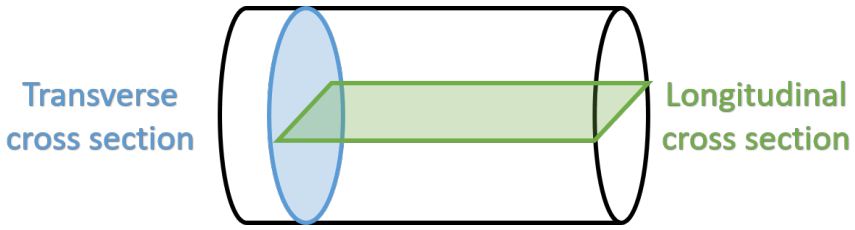

Figure 3.5: *Illustration of the two different cross-sections the samples were cut, where the blue area is the transverse cross-section and the green area is the longitudinal cross section.*

3.5 Sleeve thickness measurements

To investigate the flow of the core and sleeve material throughout the different co-extruded rods, small pieces from the transverse cross-section were cut at different lengths along the rods. At first, samples were cut from 10, 40, 70, 100, and 130 cm along the rods. These samples were grinded, polished and taken to the optical microscope (Zeiss Axio Vert.A1) where the thickness was measured using the ZEN Core software. Three measurements every 90°, as illustrated in figure 3.6, were done for each sample. These measurements were used to get an overview of how the sleeve thickness varies, as illustrated in figure 3.7. Based on this initial overview, other tests were planned and samples for thickness measurements were cut every 10 cm to create a more detailed "map" of the sleeve thickness along the length of the rods. Thickness measurements were done until the fractured part of the rods were reached.

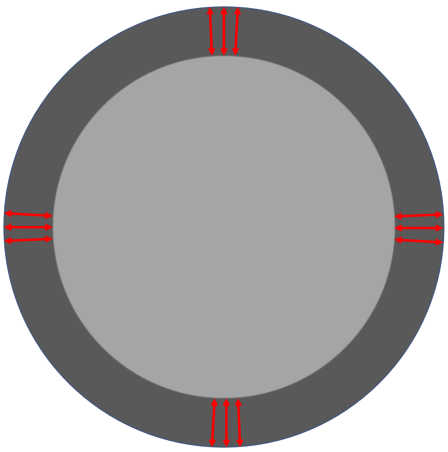

Figure 3.6: *Illustration of the sleeve thickness was measured with three parallels every 90° of the transverse cross-section.*

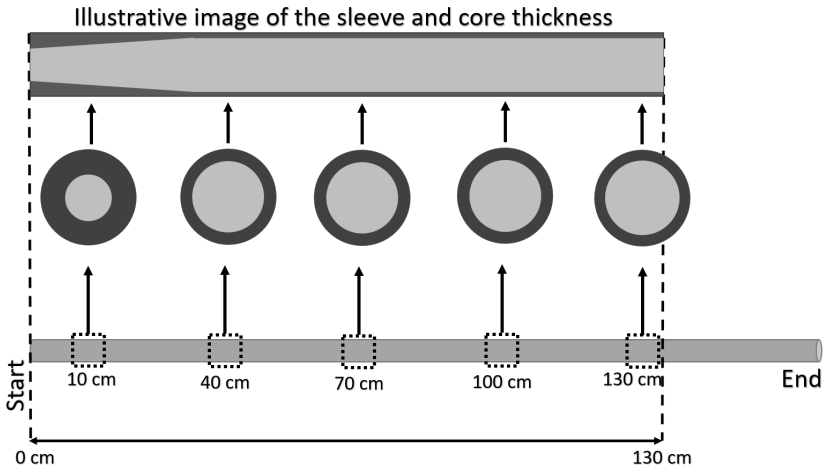

Figure 3.7: *Illustration of how the pieces cut along the co-extruded rods were used to get an overview of the sleeve thickness throughout the rods.*

3.6 Heat Treatment and Aging

In order to establish the optimal heat treatment and precipitation hardening response of the two different materials in the co-extruded rods, a precipitation hardening curve was made. The co-extruded rods with either RS AA7090 or RS AA7090-Sc as the sleeve material will hereby be referred to as CoEx1 and CoEx2-Sc, respectfully. Samples were cut from between 10 - 20 cm of the co-extruded rods, one batch of samples form a CoEx1 and one batch from CoEx2-Sc. Samples cut from the extruded DC AA7090 were used at first to create an outline of the precipitation hardening response of the AA7090 alloy.

An illustration of the heat treatment process can be seen in figure 3.8. The oven used for the solution heat treatment was a Nabertherm N30/85 HA and for

the precipitation heat treatment Nabertherm N15/65 HA and Nabertherm N30/85 HA were used. Both of these ovens are air circulation furnaces. Samples were heated from room temperature to 470°C over 90 minutes, solutionized at 470°C for 20 minutes and then quenched in a bucket of water to room temperature. One sample was taken for investigations in the as-solutionized condition, the rest of the samples were stored in a freezer holding -20°C in order to prevent natural aging at room temperature. The time between quenching and till the samples were put in the freezer was three minutes. This was kept constant for all samples. Time at room temperature between the freezer and the oven, pre-heated to 140°C, was approximately two minutes. This was also kept constant for all samples.

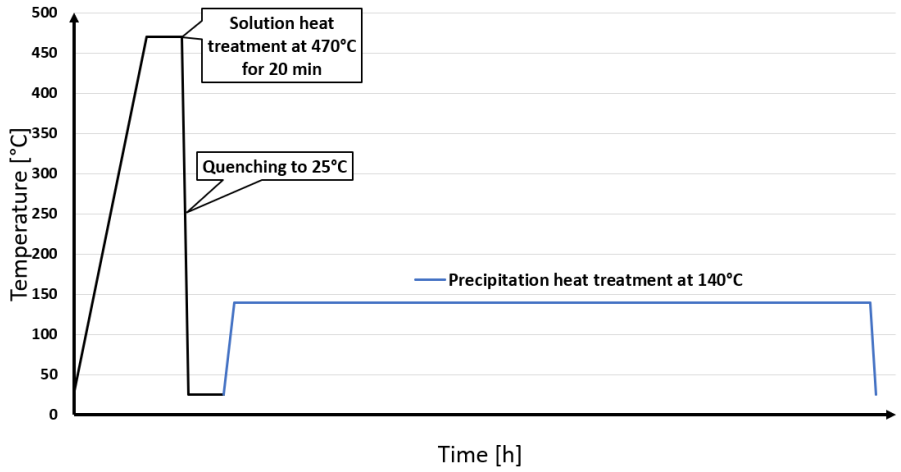

Figure 3.8: *Illustration of the heat treatment process used during this project. Solution heat treatment at 470°C and precipitation heat treatment at 140°C.*

Hardness measurements and microstructural characterization, in the transverse and longitudinal cross-section, were done of the samples in as-extruded and as-solutionized condition. The hardness measurements were done with a Zwick/Roell ZHV30 Vickers hardness tester using a load of 1 kg and l0 seconds load time. During precipitation heat treatment, only hardness measurements were done in the transverse cross-section. The measurements were done as illustrated in figure 3.9, with six measurements in the core and six measurements in the sleeve. All the samples were grinded prior to the heat treatment process to reduce the time between quenching and hardness measurements. The time between quenching and for all the 12 hardness measurements to be done, was approximately 15 minutes. This was kept constant for all the samples. The initial time intervals, for at which time during the precipitation heat treatment process the hardness measurements of the DC AA7090 were taken, started from 5 minutes all the way to 40 hours. For the co-extruded samples, measurements were done to better depict the precipitation hardening response between 30 minutes and 40 hours.

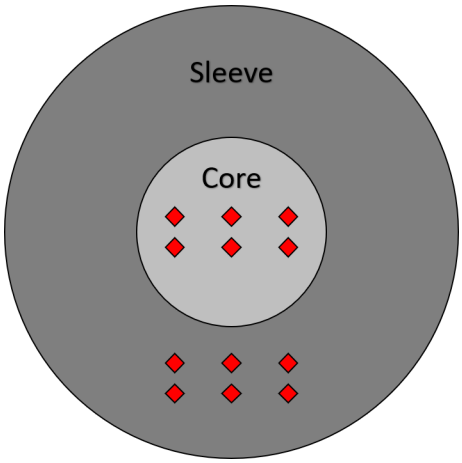

Figure 3.9: *Illustration of where the hardness measurements were taken of the co-extruded rods. Six measurements in the core and six in the sleeve material.*

3.7 Tensile Testing and Deformation Analysis

3.7.1 Tensile Testing of Normally Extruded Rods

In order to establish a basis for mechanical properties of the co-extruded rods, tensile tests of specimens of normally extruded AA6082, RS AA7090 and DC AA7090 where done. Three specimens of each material were machined at Finmekanisk verksted at Norwegian University of Science and Technology, according to figure 3.10. The tensile specimens of AA6082 were made by machining away the sleeve material of co-extruded rods. Within each material, two specimens were solutionized and aged to T6 and one specimen was kept at the solutionized condition. The machine used for the tensile testing was a MTS 810 Material Testing System and the specimens were stretched at a rate of 2 mm/min.

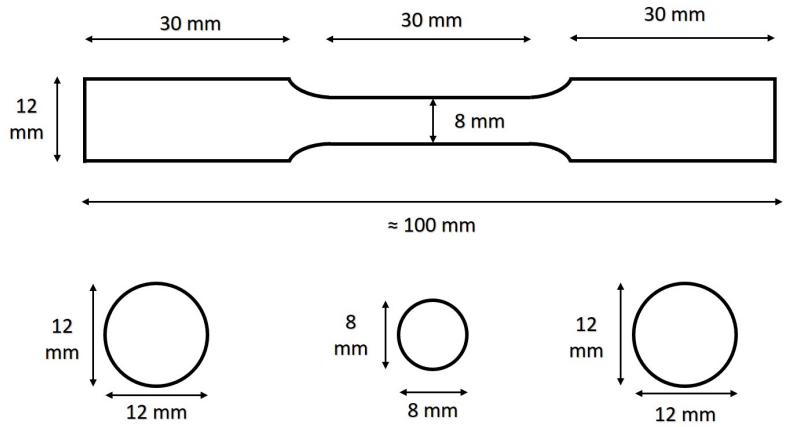

Figure 3.10: *Dimensions of the samples used for tensile testing of the normally extruded rods.*

3.7.2 Tensile Testing of Co-Extruded Rods

With the objective to find the mechanical properties of the co-extruded rods, a tensile test was performed. Samples, with a length of approximately 90 mm, were cut from different positions along the co-extruded rods with different sleeve thicknesses. Because of the fact that the rods contain a sleeve material, a normal tensile specimen geometry was not adequate. A modified tensile specimen geometry, as seen in figure 3.11, was used to better control where the fracture occurs and to investigate deformation behaviour along the interface during tensile testing. This the same geometry previously used by H. Kalager et al. [33]. The machining of the modified tensile specimens was done at Finmekanisk verksted at Norwegian University of Science and Technology and an image of two machined specimens can be seen in figure 3.12.

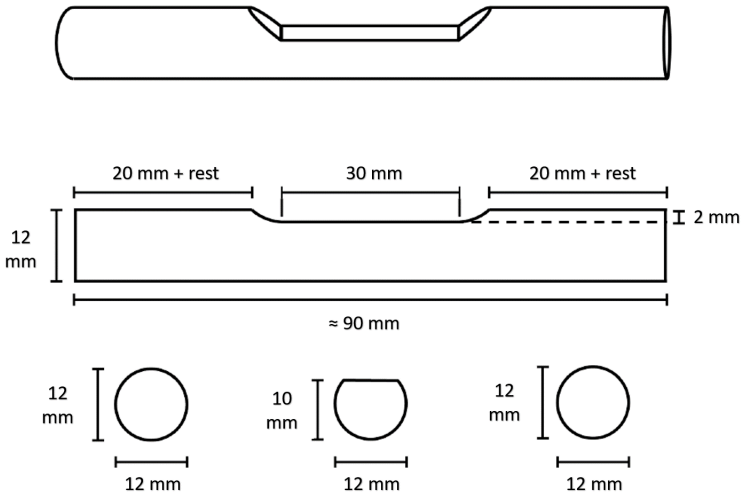

Figure 3.11: *Dimensions of the samples used for tensile testing of the co-extruded rods [33].*

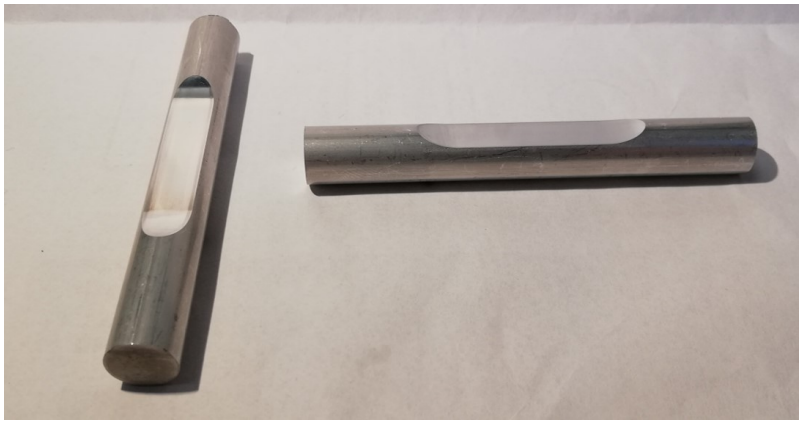

Figure 3.12: *Image of the machined tensile specimens of a co-extruded rod.*

Five and eight modified tensile specimens were made of CoEx-1 and CoEx-2, respectively. The sleeve thickness was measured at each side of the specimens, as illustrated in figure 3.13. These values, for each specimen, are listed in table 3.5 together with the average sleeve thickness. The tensile specimens will hereby be referred to as either CoEx1 or CoEx2-Sc and its average sleeve thickness, e.g. CoEx1 - 520 μm or CoEx2-Sc - 431 μm. All modified tensile specimens are solutionized and aged to T6 condition, except for CoEx1 - 222 μm and CoEx2-Sc - 234 μm which remained in the solutionized condition. The tensile testing was conducted with a MTS 810 Material Testing System and the specimens were stretched at a rate of 2 mm/min.

Figure 3.13: *Illustration of how the thickness of the sleeve varies in one tensile specimen. $t_{s,1}$ is the sleeve thickness on one side and $t_{s,2}$ is the sleeve thickness of the other side.*

Table 3.5: *Sleeve thickness at each side of the different tensile specimens as illustrated in figure 3.13 and t_A is the average sleeve thickness.*

	Material	$t_{s,1}$ [μm]	$t_{s,2}$ [μm]	t_A [μm]
CoEx-1	50 cm	1047	614	831
	60 cm	614	425	520
	90 cm	248	197	222
	100 cm	197	163	180
	130 cm	119	105	112
CoEx-2	40 cm	1534	799	1167
	50 cm, 1	859	531	695
	50 cm, 2	737	477	607
	60 cm	508	353	431
	80 cm	261	206	234
	90 cm	206	157	182
	110 cm	127	106	117
	150 cm	66	58	62

3.7.3 Deformation analysis

To investigate the deformation behaviour of the co-extruded rods during the tensile tests, a digital image correlation (DIC) technique was used. The way DIC works is that it compares digital images and deformation of specimens at the different stage during the tensile test [34]. A software can track blocks of pixels during deformation, which can be utilized to create strain maps and to do in-situ deformation analysis.

Prior to the tensile tests, the tensile specimens were coated with a white paint and sprayed using a spray gun with black paint to create small, finely distributed black dots on the flat surface of the specimens. This black and white pattern makes it easier for the software to follow the blocks of pixels throughout the tensile tests. The DIC setup can be seen in figure 3.14a, with a digital camera pointing at the flat surface of the tensile specimen. An image of the view of the camera can be seen in figure 3.14b. During tensile testing, the camera was set to take an image every second and the software was connected to the MTS 810 Material Testing System to record the corresponding loads. Instead of using an extensometer to record the strain, the strain was found by drawing a vector line across the specimen surface. The software will calculate the engineering strain based on the length of this line, which is given in pixels, throughout the test. In order to investigate how the two dissimilar materials in the core and sleeve behaved during deformation, five parallel vector lines were drawn as seen in figure 3.15. Two lines in the sleeve material and three lines in the core material, all of equal length. These lines were used to record the local strain behaviour of the core and sleeve.

In order to examine the fracture surface of the tensile specimens, samples were cut from the specimens and taken to the SEM for fractography. Two specimens of each material, CoEx1 and CoEx2-Sc, were made. For CoEx1 the specimens with average sleeve thickness of 520 μm and 180 μm were examined. While the tensile specimens with average sleeve thickness of 431 μm and 182 μm were examined for CoEx2-Sc. After being cut, the fracture samples were rinsed with acetone and dried prior to fractography in the scanning electron microscope (SEM). The parameters used in the SEM during fractography can be seen in table 3.6.

Table 3.6: *SEM parameters used during fractography of tensile specimens.*

SEM Parameters	
Aperture [μm]	30
Accelerating voltage [kV]	10
Working distance [mm]	17 - 27
Magnification	500 - 2000

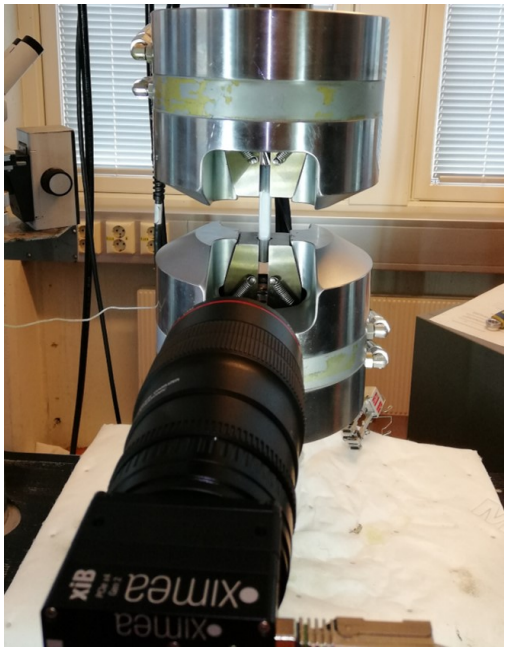

(a) Setup of the camera use for DIC during tensile testing.

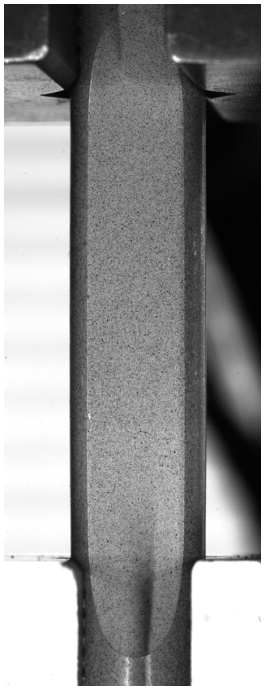

(b) View of the camera.

Figure 3.14: *Image of* ***(a)*** *the setup used for DIC during tensile testing and* ***(b)*** *how the view of the camera was.*

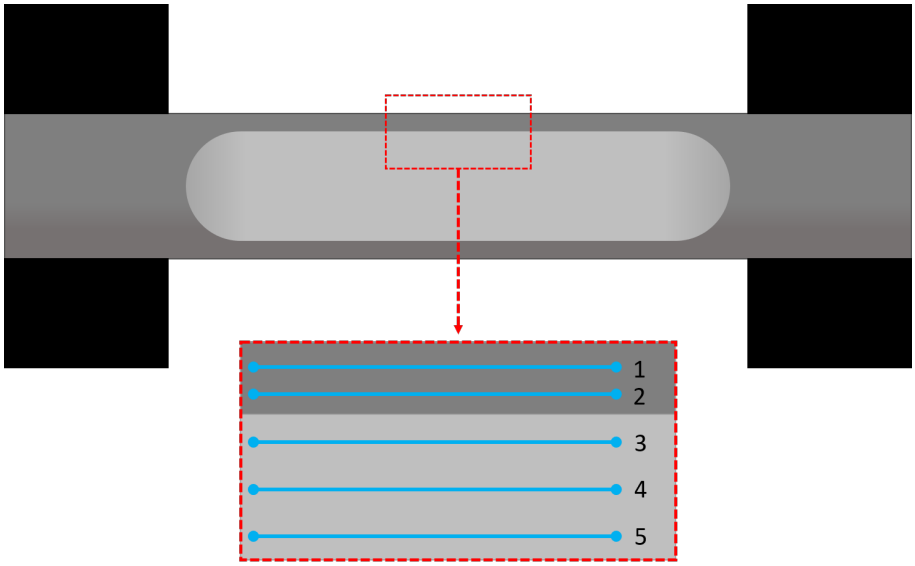

Figure 3.15: *Illustration of how the strains in the core and sleeve were followed during the tensile tests along five vector lines. Two lines in the sleeve material and three lines in the core material. The black blocks illustrate the grip area.*

4 Results

4.1 Sleeve Thickness Measurements of the Co-Extruded Rods

In this chapter, the results from the sleeve thickness measurements of the different co-extruded rods are presented. The average sleeve thickness, together with the standard deviation, for every 10 cm of the successfully co-extruded rods are given in the graphs in Appendix C. In these graphs the average sleeve thickness is plotted against the length along the co-extruded rods. To better see how the sleeve thickness differs between the four different co-extruded rods, the results are put together in one graph as seen in figure 4.1. From this graph, it can be observed that sleeve thickness through all of the co-extrusion trials seems to be relatively repetitive, except for the first 40-50 cm. The co-extruded rod of R3 Part 1 stabilized faster at lower sleeve thicknesses than the others. Co-extruded rod R2 Part 2 is the slowest to stabilize. The co-extruded rod of R3 Part 2 is the second fastest to stabilize, while R4 Part 1 is the third. At about 60 cm along the rods, the initial drop in sleeve thickness ceases and the sleeve thickness have stabilized between 349 - 425 μm for all of the rods. From here on out, the sleeve thickness decreases at approximately at the same rate for all rods.

This can be better seen in figure 4.2, which is a graph of the smaller sleeve thicknesses from 30 cm and out. Co-extruded rod R4 Part 1 started to exhibit severe fractures in the sleeve at about 60 cm, which is why the measurements stop at 70 cm. For R3 Part 2, severe fracturing started at about 90 cm and measurements were stopped at 100 cm. The co-extruded rods of R2 Part 2 and R3 Part 1 continued until all of the material was used and produced rods without fractures at 130 cm and 170 cm, respectively. The minimum sleeve thickness achieved for these two rods were 105 μm and 56 μm, respectfully. As can be seen from the standard deviation in the figures in Appendix C, the sleeve thickness was not uniform in the transverse cross-section. For all of the thickness measurements, the thickness deviates with between ± 1 - 5% of the average sleeve thickness. During the sleeve thickness measurements in the optical microscope, it was observed that there was a gap-free and perfect contact interface between the two dissimilar alloys for all samples.

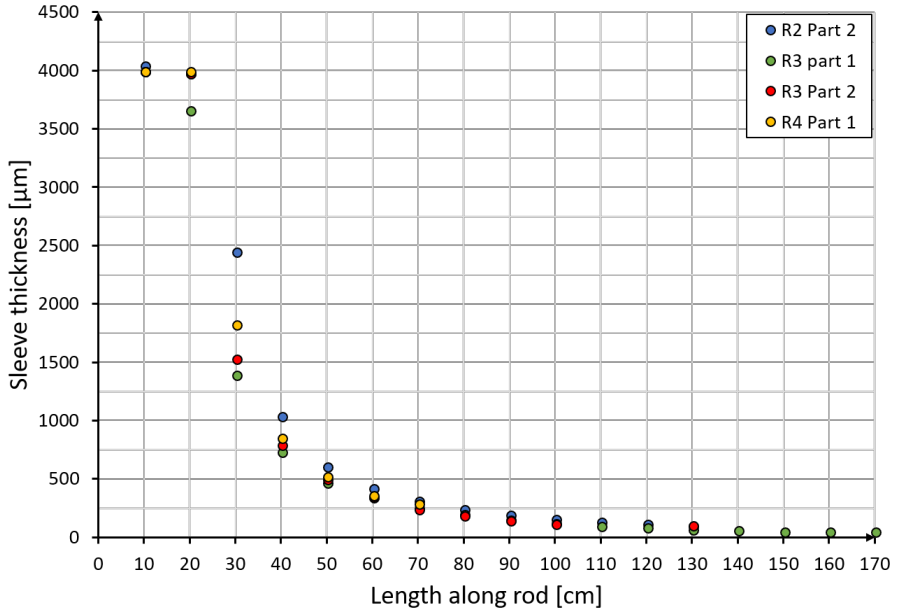

Figure 4.1: *Graphs of the average sleeve thickness along the length of the co-extruded rods of R2 Part 2 (blue), R3 Part 1 (green), R3 Part 2 (red) and R4 Part 1 (yellow).*

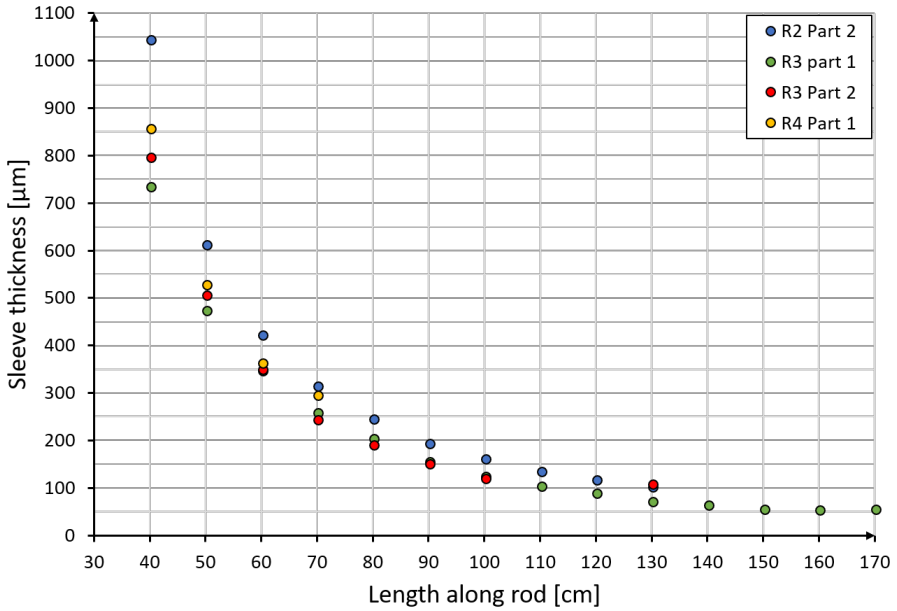

Figure 4.2: *Graphs of the average sleeve thickness along the length of the co-extruded rods of R2 Part 2 (blue), R3 Part 1 (green), R3 Part 2 (red) and R4 Part 1 (yellow).*

4.2 Heat Treatment and Aging

In the following chapter the results from the heat treatment and precipitation hardening response of DC AA7090, CoEx1 and CoEx2-Sc are presented. The results

of the heat treatment and ageing of DC AA7090 can be seen in figure 4.3. This figure shows a graph of the hardness of the solutionized sample and how the hardness varies with the time exposed to 140 °C. The x-axis shows the time in hours on a logarithmic scale. In the solutionized condition, the hardness was 116±2 HV1. After being precipitation heat treated at 140°C for 50 min, the hardness increased to 205±3 HV1. Then the hardness slowly increases to a maximum of 220±5 HV1 at 4 hours, a small decrease in hardness was measured at 5 and 6 hours before another maximum of 220±3 HV1 is reached at 10 hours. From there on out the hardness slowly decreased, with the last measurement at 40 hours falling to 197±7 HV1. The peak hardness of the DC AA7090 seems to be somewhere close to 4 - 10 hours. Based on these results, it was decided that the samples for CoEx1 and CoEx2-Sc should be more concentrated in this time frame.

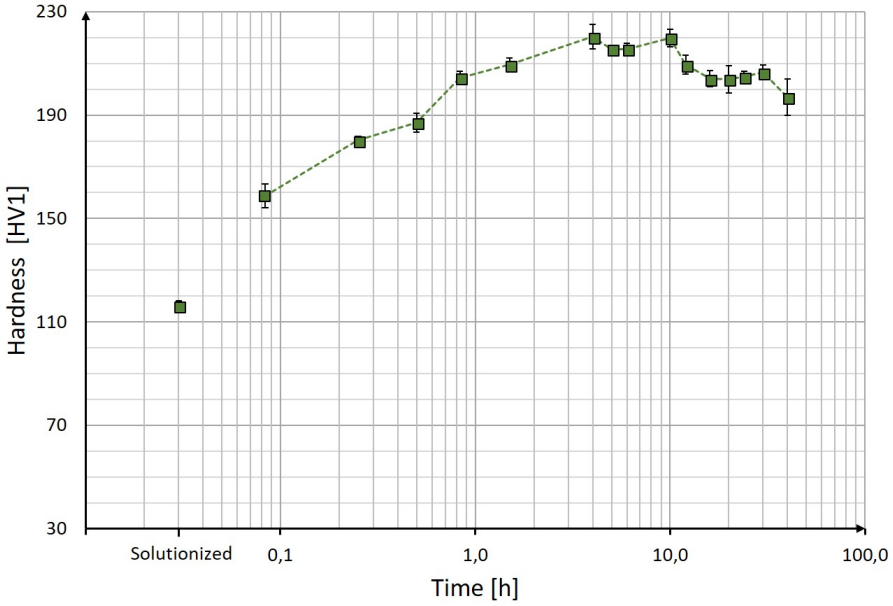

Figure 4.3: *Hardness of DC AA7090 samples as a function of time for precipitation heat treatment at 140°C.*

The results from the heat treatment and ageing of CoEx1 and CoEx2-Sc can be seen in figure 4.4. For these samples, the hardness was measured in sleeve and core material. The circular markers represent CoEx1 and the diamond markers represent CoEx2-Sc. The dark and lighter colours differentiates the sleeve and core material, respectively. Hardness measurements were done for the as-extruded- and solutionized condition and between 30 min and 30 hours. CoEx2-Sc was also measured at 40 hours exposure.

In the as-extruded condition the hardness of the sleeve in CoEx1 and CoEx2-Sc were measured to 97±2 HV1 and 105±2 HV1, respectfully. After being solutionized the hardness of CoEx1 increased to 106±1 HV1, while CoEx2-Sc went up to 108±2

HV1. CoEx1 had a hardness in the sleeve after 50 minutes of precipitation heat treatment of 194±3 HV1. A maximum after 8 hours with 216±2 HV1 and then a continuous decrease in hardness till 198±3 HV1 after 30 hours. After the first 50 minutes, CoEx2-Sc's hardness increased to 182±5 HV1 and went on to achieve a maximum, also at 8 hours, of 210±5 HV1. Afterwards, the hardness decreased to 191±3 HV1 at 40 hours exposure. Peak hardness of the sleeve material, for both CoEx1 and CoEx2-Sc, was achieved after being exposed to 140°C for 8 hours.

The core material (AA6082), for both CoEx1 and CoEx2-Sc, did not experience the same precipitation hardening response as the sleeve material. This can be seen in figure 4.4. In the as-extruded condition, both cores had a hardness of 40±1 HV1. After solution heat treatment and 8 hours of precipitation hardening at 140°C, the hardness reached 47±1 HV1 and 45±1 HV1 for the CoEx1 and CoEx2-Sc, respectfully. However, after 10 hours and onward the core material started to experience a substantial increase in hardness. After 30 hours of precipitation hardening, the core achieved a hardness of 82±1 HV1 and 79±1 HV1 for CoEx1 and CoEx2-Sc, respectfully. CoEx2-Sc had a measurement done after 40 hours as well, where the hardness of the core material was measured to 86±1 HV1.

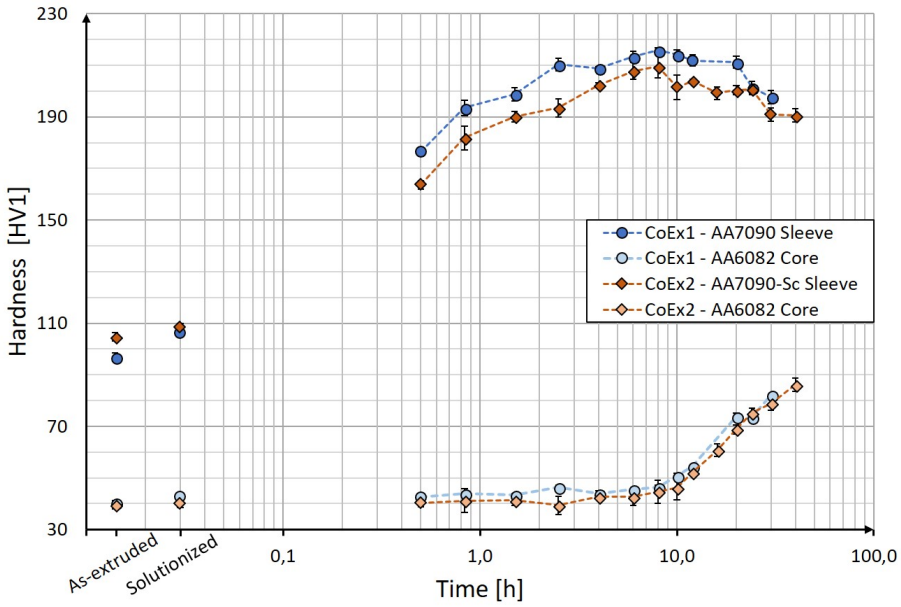

Figure 4.4: *Hardness of CoEx1 and CoEx2-Sc samples as a function of time for precipitation heat treatment at 140° C. The circular markers represent CoEx1 and the diamond markers represent CoEx2-Sc. The dark and lighter colours differentiates the sleeve and core material, respectively.*

Panorama images in the transverse and longitudinal cross-section of CoEx1 in the solutionized condition can be seen in figure 4.5a and figure 4.5b, respectively. Microstructural images of the interface and edge of the sleeve material at higher

magnification can be seen in figure 4.6. These images show that there has been grain growth in the outer 0.5 - 1 mm edge of the sleeve after solution heat treatment for CoEx1. In the transverse cross-section (figure 4.6a), it can be seen that the grains at the edge of the sleeve have grown to a size of several hundred micrometres and that they seem to follow the curve of the edge. Some clusters of small grains, less than 10 μm in size, can be observed in between some of the larger grains. Further into the sleeve material, there is an equiaxed microstructure with a grain size of less than 10 μm.

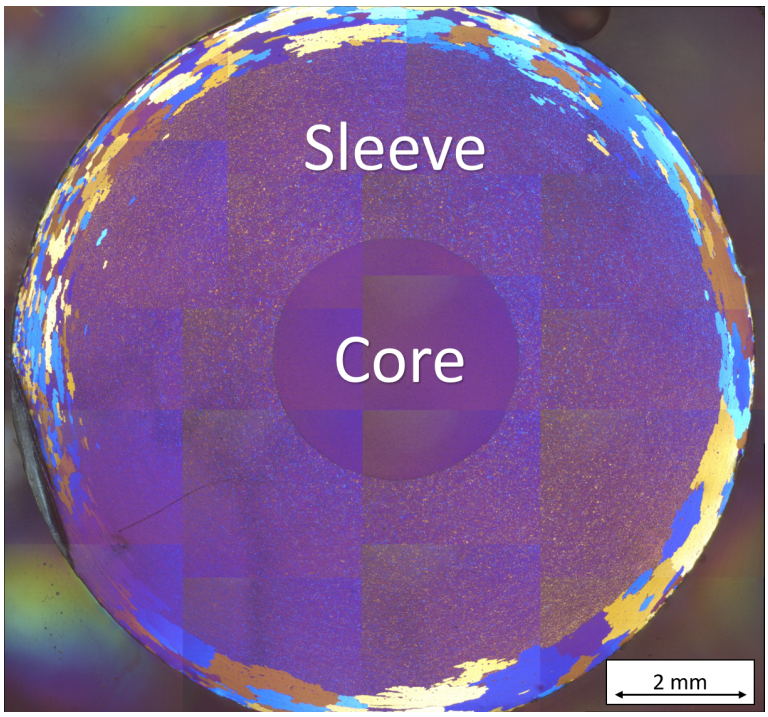

(a) *Panorama image put together of images of CoEx1 taken in the transverse cross-section at 2.5X magnification.*

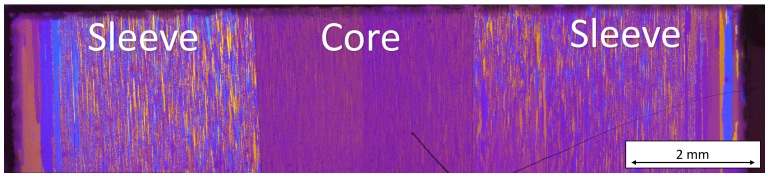

(b) *Panorama image put together of images of CoEx1 taken in the longitudinal cross-section at 2.5X magnification.*

Figure 4.5: *Panorama images of CoEx1 in the* ***(a)*** *transverse and* ***(b)*** *longitudinal cross-section after solution heat treatment.*

From figure 4.6b an image of the gap-free interface between the sleeve and core material in the transverse cross-section can be observed. The core is at the top of the image, while the sleeve is at the bottom. Along the interface, there seems to be a concentration of particles. There can also be observed to be lines of particles

in the sleeve material close to the interface. In the longitudinal cross-section, the microstructure was observed to have a more fibrous structure with the grains arranged along the extrusion direction. Also here, grain growth at the edge of the sleeve and clusters of small grains in between the larger grains can be observed (figure 4.6c). Further into the sleeve material, a microstructure with a combination of thin fibrous grains and equiaxed grains can be seen. The interface between the core and sleeve material in the longitudinal cross-section can be seen in figure 4.6d. Here, the combined microstructure of fibrous and equiaxed grains can be observed on the right and the fibrous microstructure of the core material on the left.

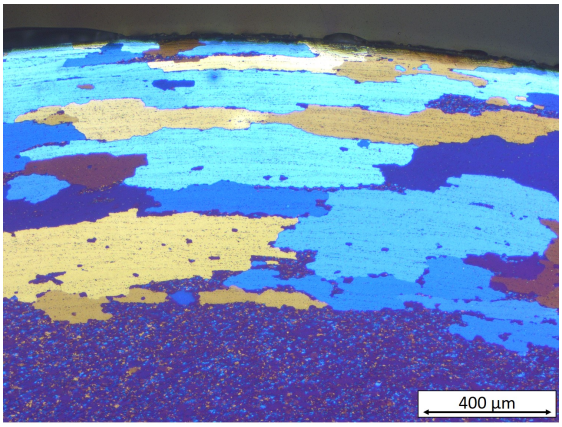

(a) *Transverse cross-section of sleeve edge at 5X magnification. Edge at the top part of the image.*

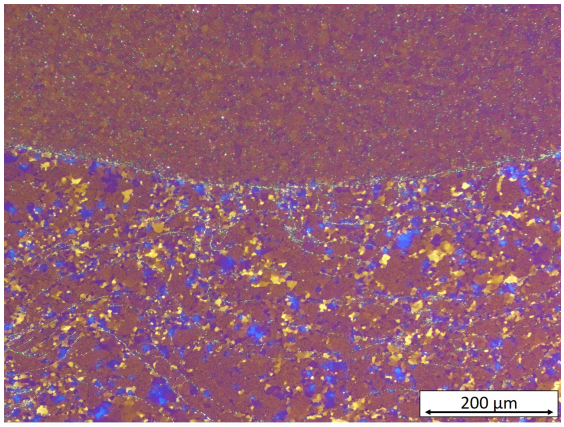

(b) *Transverse cross-section of interface at 10X magnification. The core is at the top part of the image.*

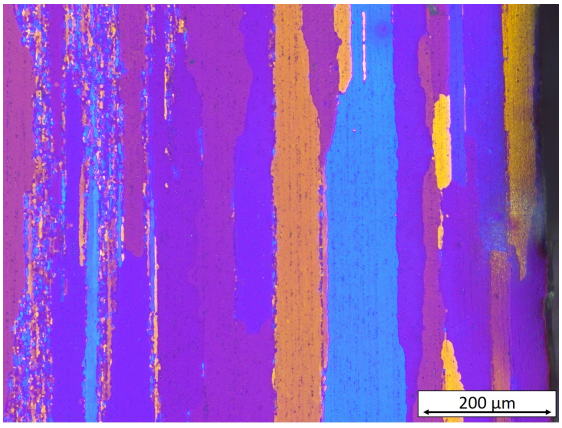

(c) *Longitudinal cross-section of sleeve edge at 10X magnification. Edge at the right part of the image.*

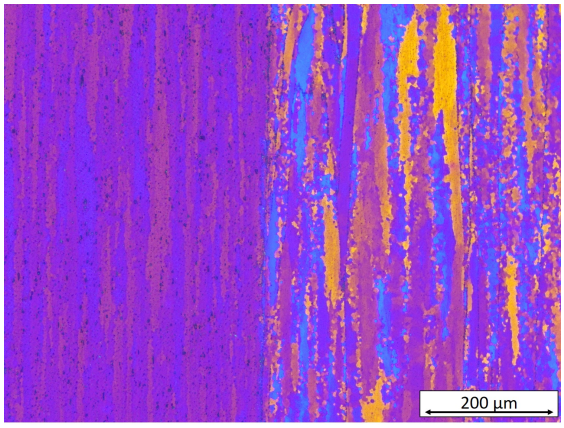

(d) *Longitudinal cross-section of interface at 10X magnification. The core is at the left part of the image.*

Figure 4.6: *Images of the microstructure of a sample of CoEx1, taken from 10 cm into the rod, in the solutionized condition in the transverse (**(a)** and **(b)**) and longitudinal (**(c)** and **(d)**) cross-section. Image **(a)** and **(c)** shows images of the sleeve edge, while **(b)** and **(d)** shows images of the interface between the sleeve and core material.*

The panorama images of CoEx2-Sc, in the transverse and longitudinal cross-section, after solution heat treatment can be seen in figure 4.7. Microstructural images at a higher magnification of the sleeve and interface of CoEx2-Sc are presented in figure 4.8.

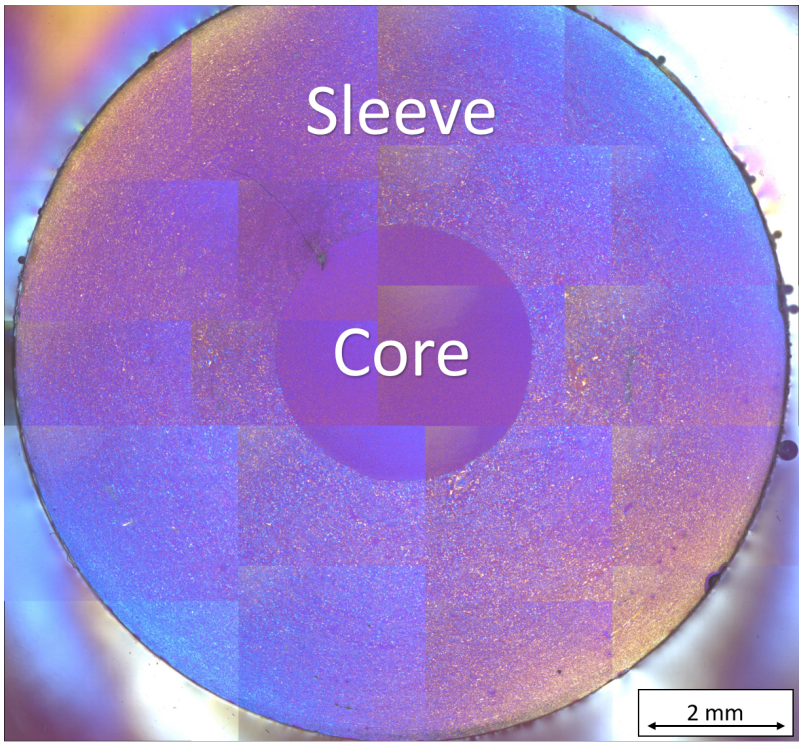

(a) *Panorama image put together of images of CoEx2-Sc taken in the transverse cross-section at 2.5X magnification.*

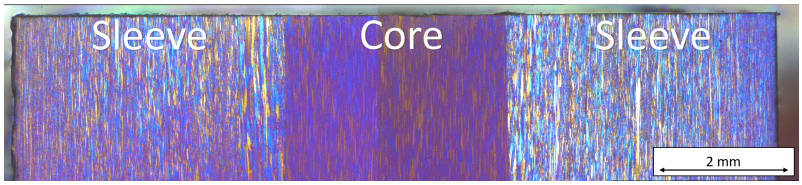

(b) *Panorama image put together of images of CoEx2-Sc taken in the longitudinal cross-section at 2.5X magnification.*

Figure 4.7: *Panorama images of CoEx2-Sc in the* ***(a)*** *transverse and* ***(b)*** *longitudinal cross-section after solution heat treatment.*

Compared to what has been previously seen in the transverse cross-section of CoEx1, CoEx2-Sc seemed to not have experienced any grain growth at the edge of the sleeve material. As as observed in figure 4.8a. Here, the size of the grains are in the order of 1 - 10 μm through almost all of the sleeve. Closer to the interface, the microstructure of the sleeve becomes more complex. A microstructure containing clusters of equiaxed grains with a size of a few micrometres, surrounded by larger equiaxed grains with a size of 10 - 20 μm. This complex microstructure can be

observed in figure 4.8b, where the core material can be seen at the top of the image with the sleeve below. From this figure, the interface between the core and sleeve material be seen. Also here, the interface and some of the grain boundaries in the sleeve material are decorated with what looks like particles.

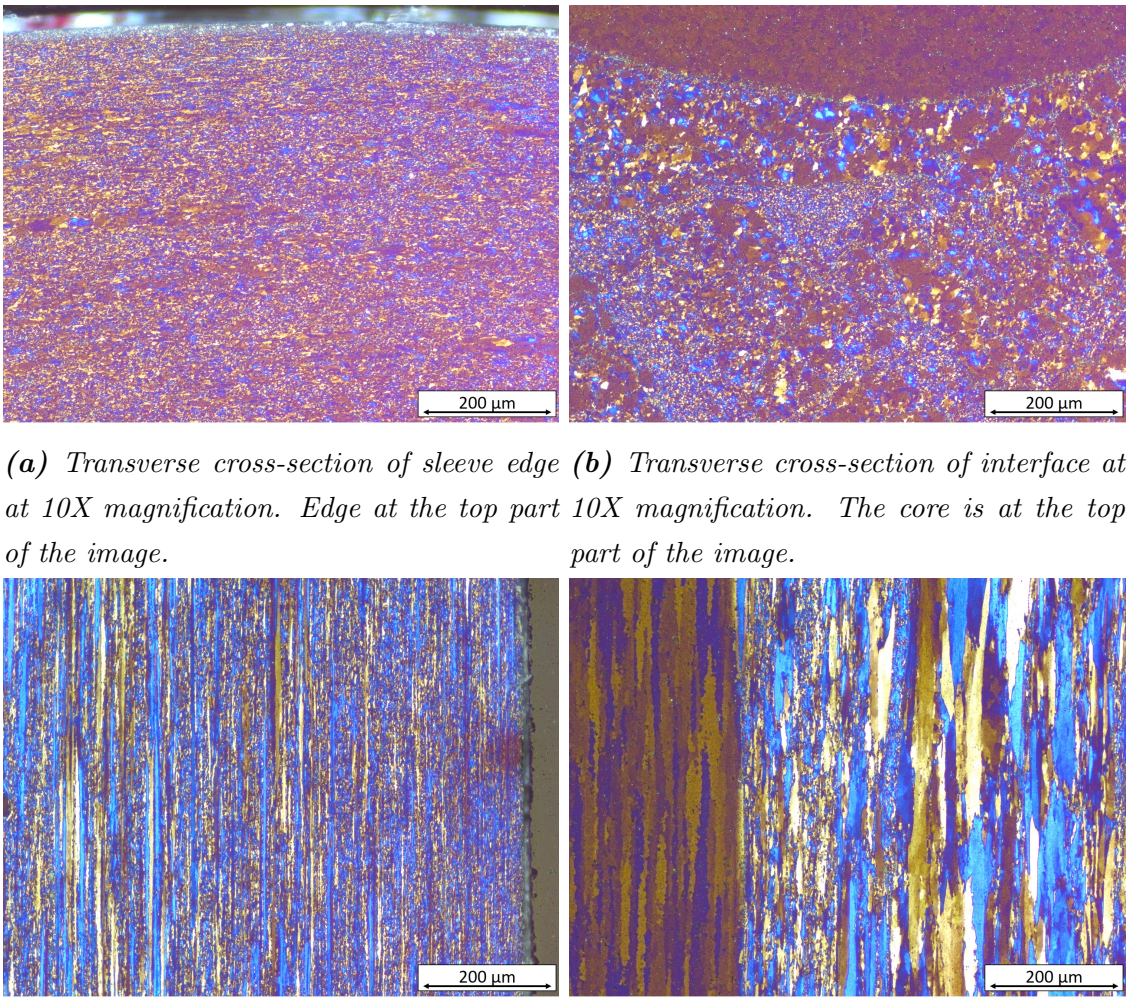

(a) *Transverse cross-section of sleeve edge at 10X magnification. Edge at the top part of the image.*

(b) *Transverse cross-section of interface at 10X magnification. The core is at the top part of the image.*

(c) *Longitudinal cross-section of sleeve edge at 10X magnification. Edge at the right part of the image.*

(d) *Longitudinal cross-section of interface at 10X magnification. The core is at the left part of the image.*

Figure 4.8: *Images of the microstructure of a sample of CoEx2-Sc, taken from 10 cm into the rod, in the solutionized condition in the transverse (**(a)** and **(b)**) and longitudinal (**(c)** and **(d)**) cross-section. Image **(a)** and **(c)** shows images of the sleeve edge, while **(b)** and **(d)** shows images of the interface between the sleeve and core material.*

As previously seen in the longitudinal cross-section of CoEx1, the same fibrous and equiaxed microstructure was observed in CoEx2-Sc. Except that the thin, fibrous grains can be seen all the way to the edge of the sleeve for CoEx2-Sc, as seen in figure 4.8c. The fibrous grains becomes slightly thicker and longer the further

away they are from the edge. Figure 4.8d shows the interface between the core on the left and sleeve on the right. Close to the interface, the microstructure of the sleeve contains slightly larger fibrous grains with equiaxed small grain in between. The core material shows a fibrous microstructure, also elongated along the extrusion direction. No gaps were observed at the interface between the two dissimilar alloys.

After several attempts of anodizing of the as-extruded samples, no complete microstructural images of CoEx1 and CoEx2-Sc was produced. A few microstructural images of the as-extruded samples can be seen in figure 4.9. Even at higher magnification, it was not possible to see the microstructure of the sleeve material. For both CoEx1 and CoEx2-Sc, the sleeve material seemed to be full of particles as seen in figure 4.9a and 4.9c, that may have affected the anodizing process. As seen in figure 4.9b and 4.9d, the core material was successfully anodized in the same process.

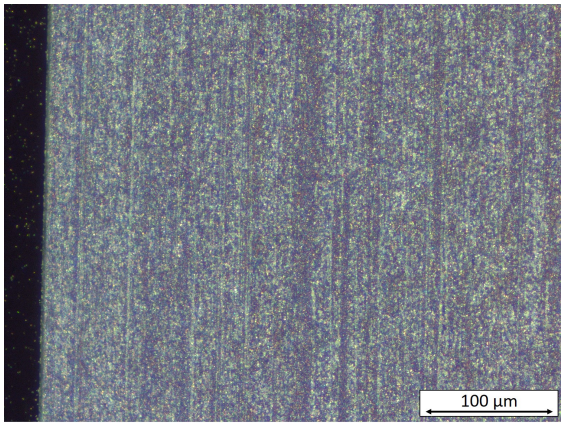

(a) *Longitudinal cross-section of the sleeve edge of CoEx1 at 20X magnification. Edge on the left.*

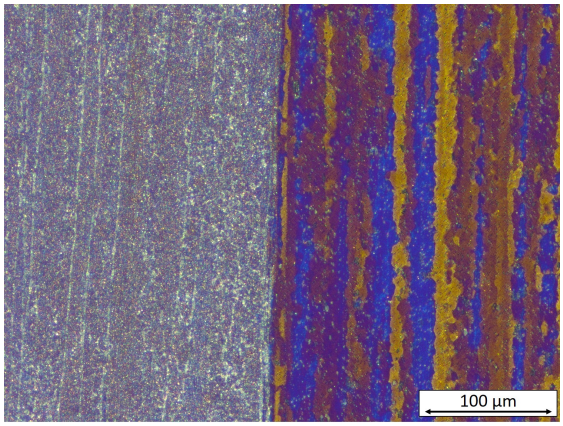

(b) *Longitudinal cross-section of the interface of CoEx1 at 20X magnification. Core material on the right.*

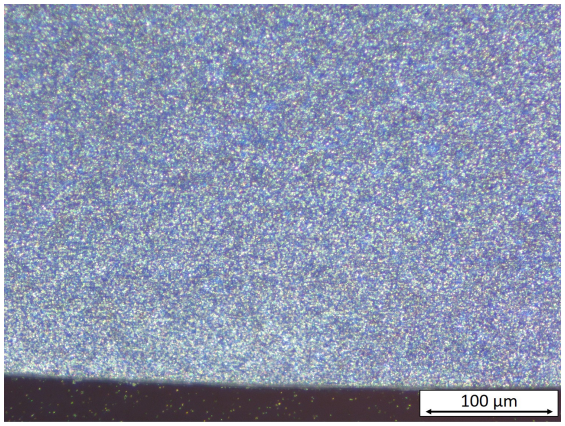

(c) *Transverse cross-section of the sleeve edge of CoEx2-Sc at 20X magnification. Edge at the bottom.*

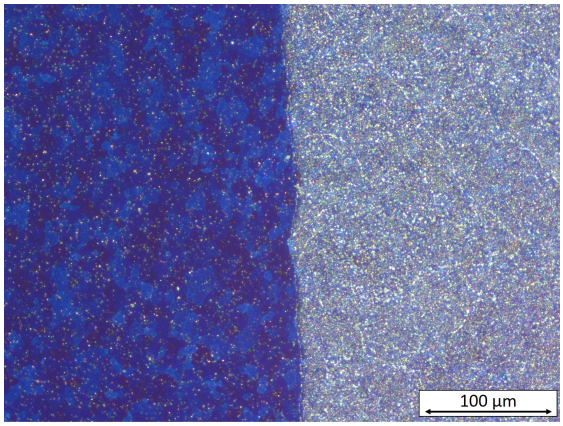

(d) *Transverse cross-section of the interface of CoEx2-Sc at 20X magnification. Core on the left.*

Figure 4.9: *Images of the microstructure of samples of CoEx1 (**(a)-(b)**) and CoEx2-Sc (**(c)-(d)**) in the as-extruded condition.*

4.3 Tensile Testing and Deformation Analysis

In the following chapter, the results from the tensile testing of the normal tensile specimens and modified tensile specimens of the co-extruded rods are presented. Deformation analysis done with the DIC and fractography were done in the SEM of co-extruded tensile specimens are also presented here.

4.3.1 Tensile Testing of Normal Tensile Specimens

The results of the tensile tests of the normal tensile specimens are presented as stress-strain curves in figure 4.10 for the DC AA7090 and RS A7090 and in figure 4.11 for the specimens of AA6082. The specimens referred to as 'aged' are solutionized at 470°C and precipitation heat treated at 140°C for 8 hours. Specimens named with 'SS' are solutionized at 470°C. A summary and comparison of the mechanical properties extracted from these tensile tests are presented below. Figure 4.12 shows the σ_{YS} of the specimens, figure 4.13 shows the σ_{TS} and 4.14 shows the ductility.

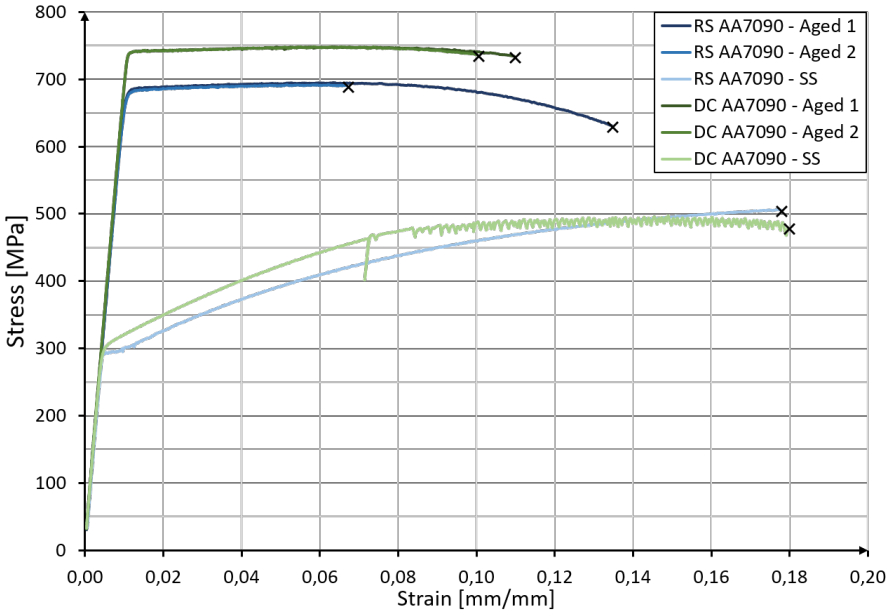

Figure 4.10: *Stress-strain curves recorded during tensile testing of normal tensile specimens of DC AA7090(green lines) and RS AA7090(blue lines). The two darker colored lines are the aged specimens, while the lighter colored lines are the solutionized specimens. The 'X' shows when fracture occurred for each specimen.*

As seen in figure 4.10, the stress-strain curves of the two aged specimens of DC AA7090 were almost identical. The only main difference was that DC AA7090 - Aged 1 had a ductility of 11% and DC AA7090 - Aged 2 had a ductility of 10%. The σ_{YS} and σ_{TS} of both aged specimens were measured to 741 MPa 748 MPa, respectively. The stress-strain curve of the solutionized specimen experienced serration from a

strain of 0.07 and until fracture. The σ_{YS} and σ_{TS} of the solutionized DC AA7090 specimen were measured to 309 MPa and 497 MPa, while the ductility was 18%.

The stress-strain curves of the aged specimens of RS AA7090 were also relatively identical, except for the ductility. The σ_{YS}, σ_{TS} and ductility of RS AA7090 - Aged 1 was measured to 685 MPa, 695 MPa and 13.4%, respectively. For RS AA7090 - Aged 2 these were 680 MPa, 691 MPa and 6.7%, respectively. The solutionized specimen achieved a σ_{YS} of 294 MPa, which was below that measured for the solutionized condition of DC AA7090. But σ_{TS} for RS AA7090 was measured to 506 MPa, which was above DC AA7090. The ductility of the solutionized RS AA7090 was 17.8%.

As observed from the stress-strain curve in figure 4.11, the two aged specimens of AA6082 did not produce two identical curves. The σ_{YS} and σ_{TS} of AA6082 - Aged 1 were measured to 125 MPa and 211 MPa, respectively, and the ductility was 20%. While AA6082 - Aged 2 was measured to 100 MPa for the σ_{YS}, 189 MPa for the σ_{TS} and a ductility of 30.3%. In the solutionized condition, the mechanical properties of AA6082 were measured to 93 MPa, 172 MPa and 34.4% for the σ_{YS}, σ_{TS} and ductility, respectively.

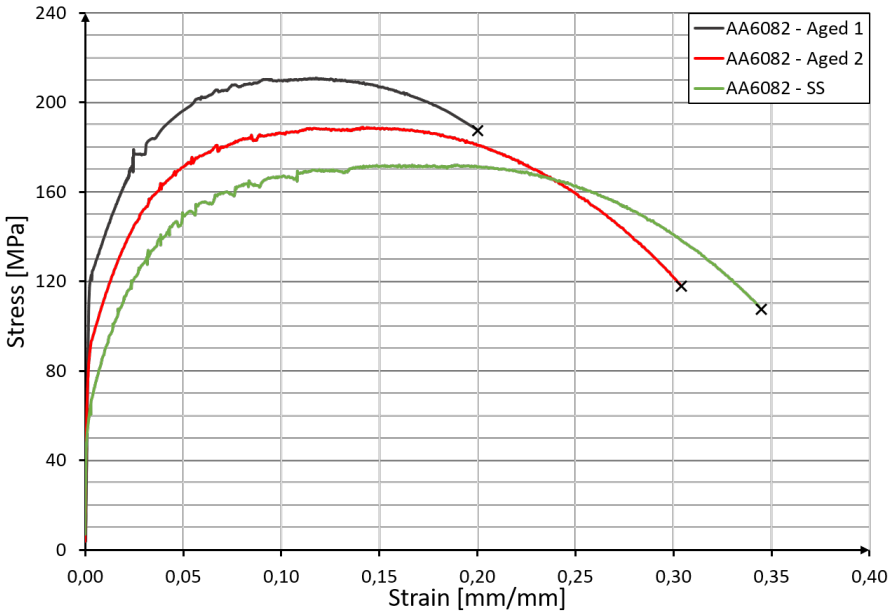

Figure 4.11: *Stress-strain curves recorded during tensile testing of normal tensile specimens of AA6082. The gray, red and green coloured lines are the Aged 1, Aged 2 and SS specimens, respectively. The 'X' shows when fracture occurred for each specimen.*

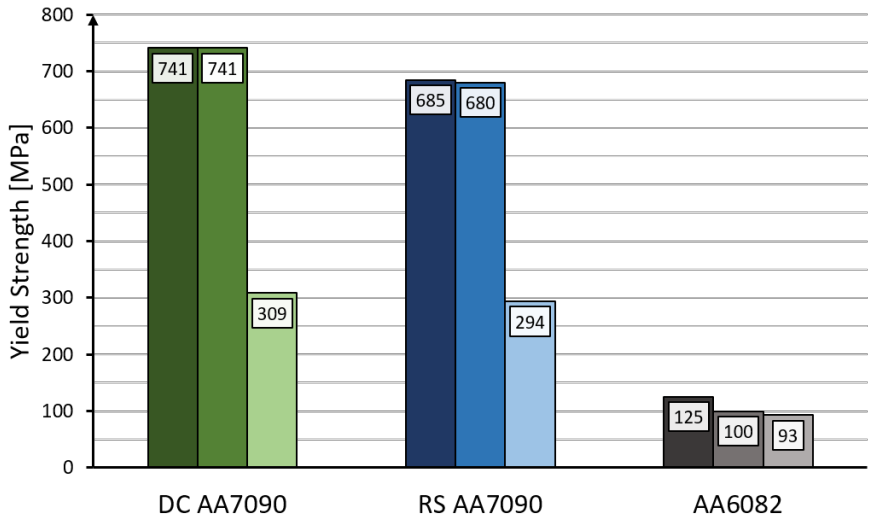

Figure 4.12: *Summary and comparison of the yield strength(σ_{YS}) measured during tensile testing of DC AA7090, RS AA7090 and AA6082. Within each different material, the columns represent specimens 'Aged 1', 'Aged 2' and 'SS' from left to right.*

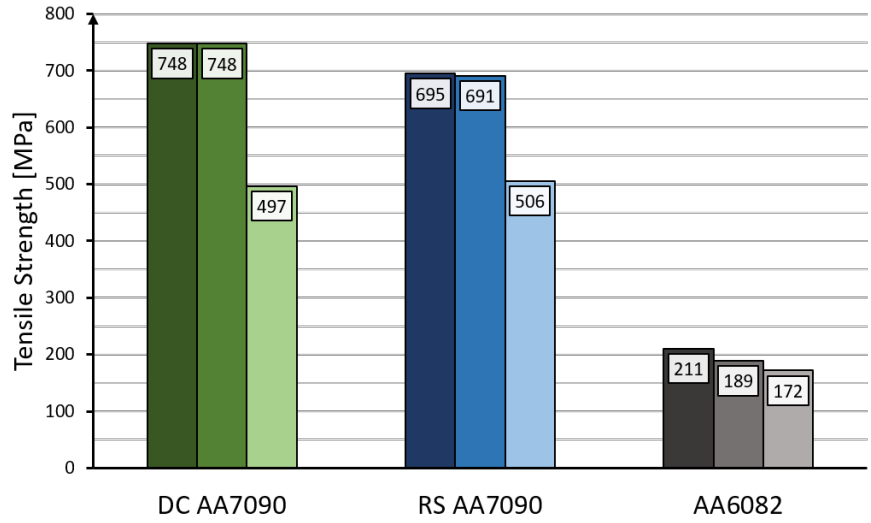

Figure 4.13: *Summary and comparison of the tensile strength(σ_{TS}) measured during tensile testing of DC AA7090, RS AA7090 and AA6082. Within each different material, the columns represent specimens 'Aged 1', 'Aged 2' and 'SS' from left to right.*

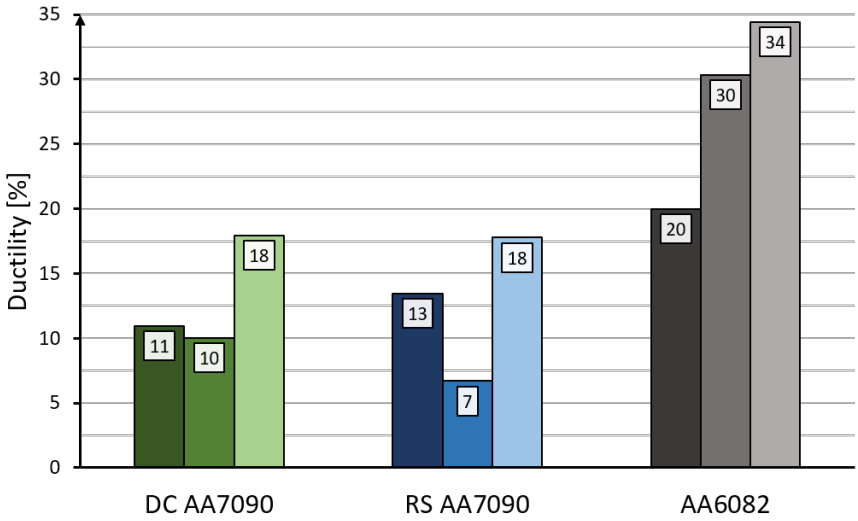

Figure 4.14: *Summary and comparison of the ductility measured during tensile testing of DC AA7090, RS AA7090 and AA6082. Within each different material, the columns represent specimens 'Aged 1', 'Aged 2' and 'SS' from left to right.*

4.3.2 Tensile Testing of Co-Extruded Rods

Stress-strain curves achieved through tensile testing of the modified tensile specimens of CoEx1 with different sleeve thickness' are presented in figure 4.15. The specimen named with 'SS' has just been solutionized at 470°C, while the rest of the specimens has been solutionized at 470°C and precipitation heat treated at 140°C for 8 hours. Because of the fact that the tensile testing procedures conducted here were not according to any standard, the results were not comparable to those of the literature. Due to difficulties with the specimens collapsing in the tension grip during some tests, the gripping force had to be lowered. Resulting in movement of the grips at higher stresses. Once the tension grips reached a position where they would not slide anymore, the tests continued as normal. The point at where the upper and lower grip reached this position can be seen as two jumps in the stress-strain curve. A summary of the maximum stress during tensile testing of CoEx1 with different sleeve thicknesses can be seen in figure 4.16.

For the two specimens with larges sleeve thickness, 831 μm and 520 μm, one large crack initiated in the surface layer before necking. The crack initiated at 0.09 and 0.12 strain, respectively. Once the crack reached the core material, the local strains in the core increased rapidly and fractures occurred soon thereafter. For specimen with 831 μm sleeve thickness the fracture occurred at 0.10 strain and the one with 520 μm fractured at 0.15. The maximum stress measured of CoEx1 with 831 μm and 520 μm sleeve thickness were 259 MPa and 230 MPa, respectively. For the specimen with a sleeve thickness of 180 μm, five to six cracks in the sleeve

material were observed before necking. Once necking started, more and more cracks nucleated locally, strains in the core increased and fracture occurred. The first crack was observed to initiate at 0.12 strain, while the fracture occurred at 0.19 strain. Maximum stress was measured to 205 MPa. For the specimen with a sleeve thickness of 112 μm, the first crack was observed at 0.8 strain and several cracks initiated before necking. When necking began the cracks close to the necking grew, but it took some time before fracture occurred at a strain of 0.24. The maximum stress was measured to 187 MPa for CoEx1 with 112 μm sleeve thickness. For the solutionized specimen, no cracks were observed in the sleeve before necking. The first crack nucleated at a strain of 0.31, and fracture through this crack occurred shortly after at 0.34 strain. Maximum stress recorded was 183 MPa for the solutionized specimen with a sleeve thickness of 222 μm.

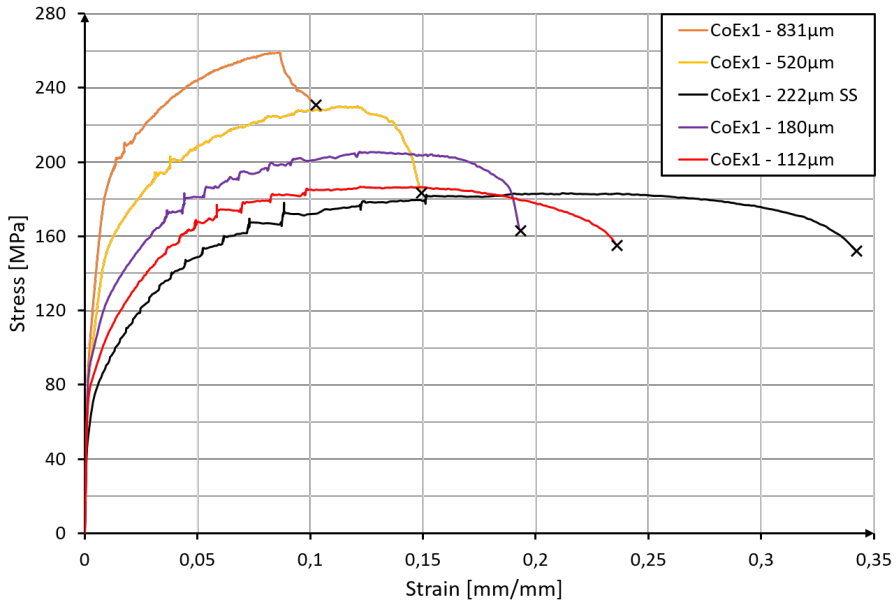

Figure 4.15: *Stress-strain curves recorded during tensile testing of CoEx1. The curves are from specimens with average sleeve thickness of 831 µm(orange), 520 µm(yellow), 180 µm(purple), 112 µm(red) and the solutionized specimen with 222 µm thickness(black). The 'X' shows when fracture occurred for each specimen.*

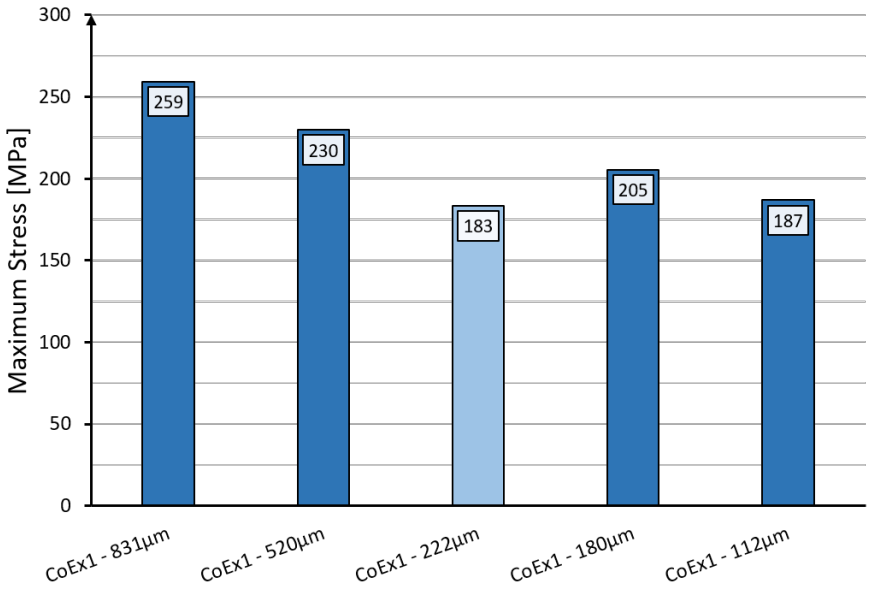

Figure 4.16: *Maximum stress measured during tensile tests of co-extruded rods of CoEx1 with different average sleeve thicknesses. The lighter blue column shows the solutionized specimens.*

The stress-strain curves recorded during tensile testing of CoEx2-Sc are presented in figure 4.17 and figure 4.18. For the CoEx2-Sc tensile specimens with sleeve thickness of 1167 μm, 695 μm and 607 μm, fracture occurred in the tension grips and these results will hereby be excluded. Fracture in the tension grips happened because of too high gripping force. A summary of the maximum stress recorded during tensile testing of CoEx2-Sc with the different sleeve thicknesses is given in figure 4.19.

For the CoEx2-Sc specimen with a sleeve thickness of 431 μm, the first crack initiated approximately 1 mm away from the tension grip after 0.046 strain. The crack grew fast and reached the core material, causing rapid necking and fracture after 0.08 strain. It should be noted that the fracture did not occur in the tension grips, but relatively close. Maximum stress was measured to 205 MPa for the specimen with an average sleeve thickness of 431 μm. The specimen with sleeve thickness of 182 μm experienced crack initiation in the sleeve almost at the same time necking also started, at 0.17 strain. The crack grew as necking continued, causing increased localized strains in the core material and fracture occurred at 0.24 strain. The maximum stress recorded during tensile testing of this specimen was 205 MPa. For the specimen with sleeve thickness of 117 μm, the first necking started before any cracks were observed. The first crack in the sleeve was observed after 0.21 strain and fracture occurred soon thereafter at a strain of 0.25. Necking and crack initiation developed simultaneously for the specimen with sleeve thickness of

62 μm, at 0.16 strain. As necking advanced, several cracks in the sleeve reached the core material. Maximum stress was measured to 201 MPa and fracture did not occur until the strain reached 0.24. For the solutionized specimen with a sleeve thickness of 234 μm, the tensile test went on normally at first. Once necking started close to the tension grip, a crack initiated in the grip at 0.215 strain and fracture occurred rapidly afterwards at 0.22 strain. The maximum stress measured of the solutionized tensile specimen was 194 MPa.

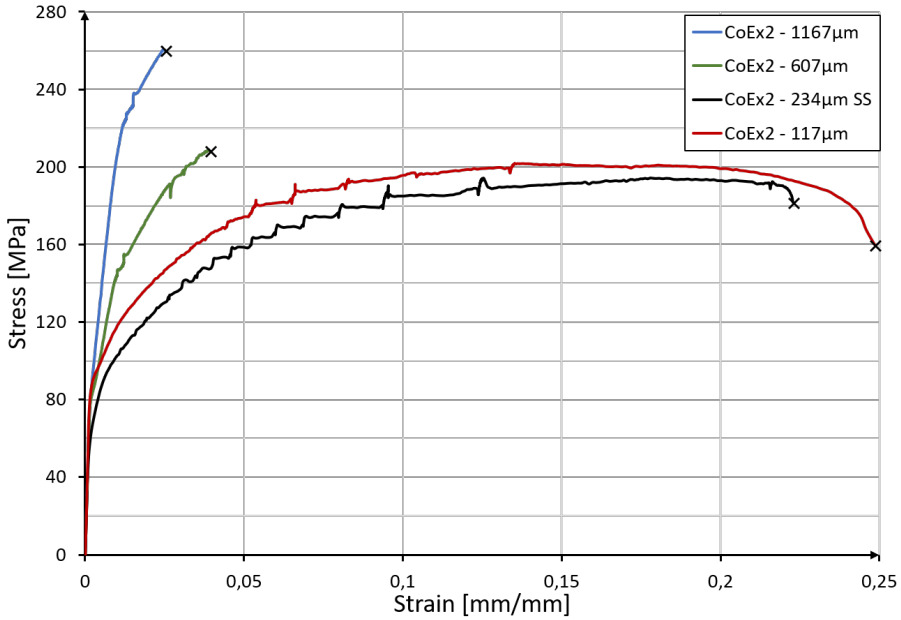

Figure 4.17: *Stress-strain curves recorded during tensile testing of CoEx2-Sc. The curves are from specimens with average sleeve thickness of 1167 µm(blue), 607 µm(green), 117 µm(red) and the solutionized specimen with 234 µm thickness(black). The 'X' shows when fracture occurred for each specimen.*

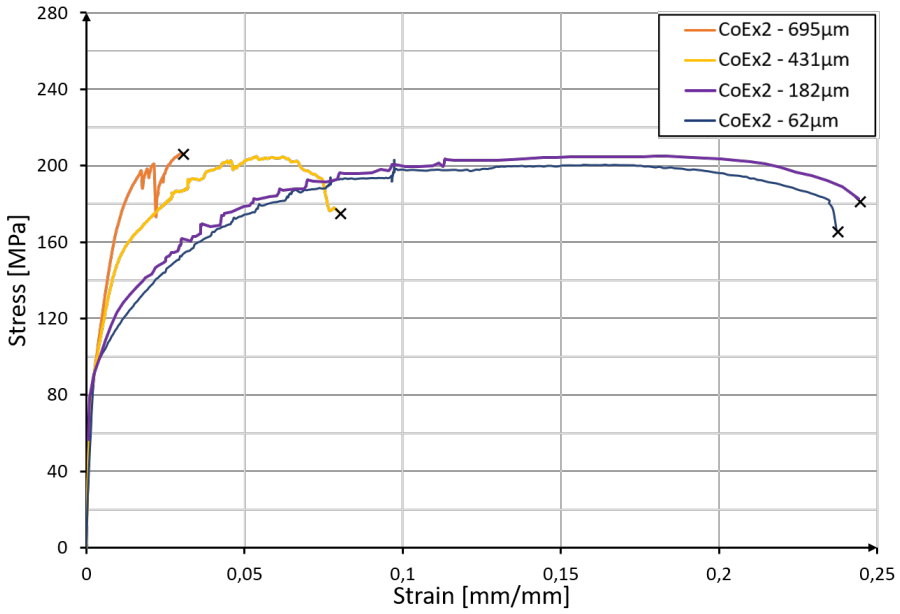

Figure 4.18: *Stress-strain curves recorded during tensile testing of CoEx2-Sc. The curves are from specimens with average sleeve thickness of 695 µm(orange), 431 µm(yellow), 182 µm(purple) and 62 µm(dark blue). The 'X' shows when fracture occurred for each specimen.*

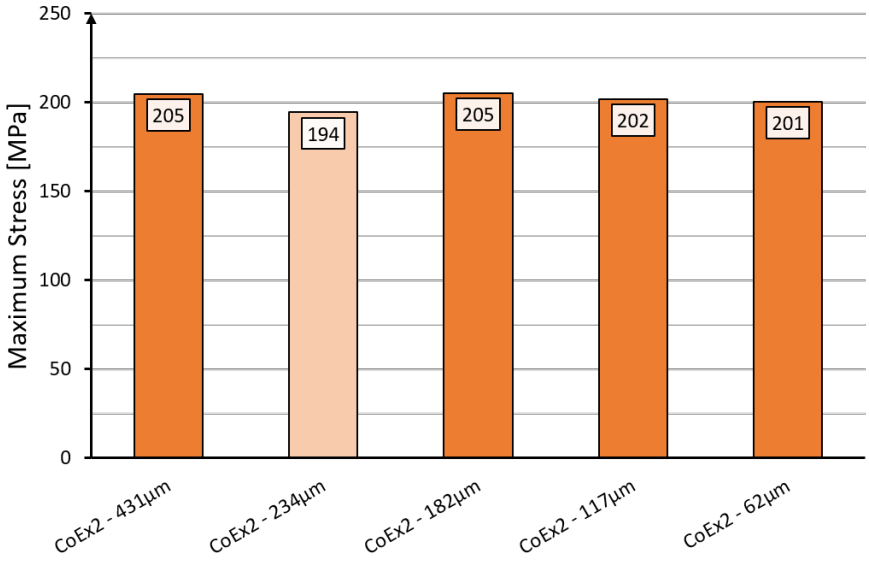

Figure 4.19: *Maximum stress measured during tensile tests of co-extruded rods of CoEx2-Sc with different average sleeve thicknesses. The lighter orange column shows the solutionized specimens.*

4.3.3 Deformation Analysis

The strain field on the flat surface of CoEx1 with an average sleeve thickness of 180 μm was investigated using DIC during different positions on the stress-strain curve, as marked in figure 4.20. Images showing the strain fields of the engineering strain of this specimen can be seen in figure 4.21. Some blocks in these strain fields were removed due to the software having difficulties tracking the blocks during changes in topographic and lighting conditions throughout the tests. This was also why the mesh was not placed all the way to the edge of the sleeve, as this always caused problems.

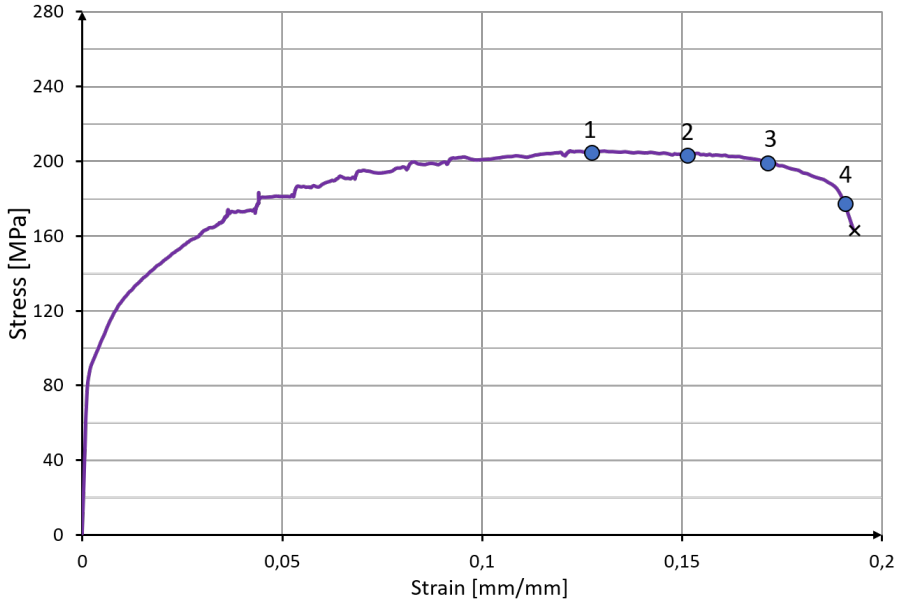

Figure 4.20: *Stress-strain curve of CoEx1 - 180 µm with four positions from where the DIC strain field images in figure 4.21 are taken.*

The strain field of position 1 on the stress-strain curve in figure 4.20 can be seen in figure 4.21a. This strain field image shows the specimen when the maximum stress of 205 MPa was recorded, before necking. The global strain was 0.13, but on the right side there has started developing local strains to above 0.16. Strains up to 0.25 can be seen in the top right corner where a crack has nucleated. For position 2 (figure 4.21b), necking has started, stress has declined to 204 MPa and global strain was measured to 0.15. A crossed pattern of increased strains in lines 45° to the tensile direction can be seen. The local strains are highest close to the sleeve, up to 0.25, and gradually decreases as the lines approach the centre of the core. In the core material, many small crossed strain lines can be observed with strain reaching 0.16 - 0.19 locally. Another crack has nucleated in the top left corner, causing increased strains in a line close to it. At position 3 (figure 4.21c), necking has continued and

more cracks have nucleated in the sleeve close to where the locally high strains were previously observed. Global stress and strain are 200 MPa and 0.17, respectively. The strain lines have increased in size, with some of them already spanning across the whole surface with local strains between 0.20 and 0.34. Position 4 (figure 4.21d) shows the strain field seconds before fracture with global stress and strains at 178 MPa and 0.19, respectively. Large strain lines form a V-shape, where local strains above 0.27 spans across the surface in two directions. The fracture occurred in the line closest to the centre of the specimen.

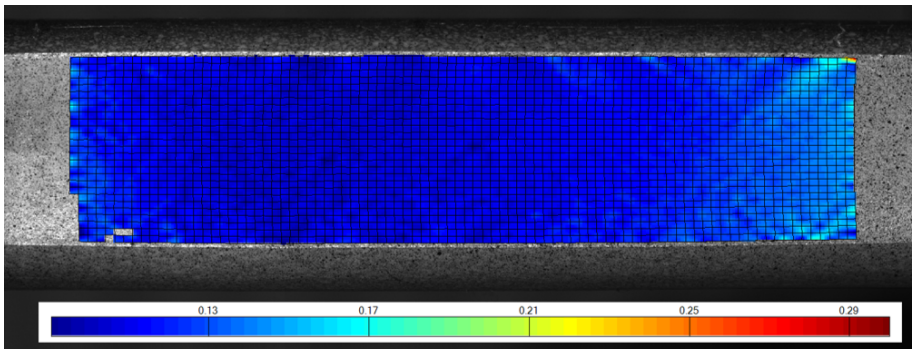

(a) *Position 1: Global stress and strain at 205 MPa and 0.13, respectively. Before necking, crack observed in top right corner.*

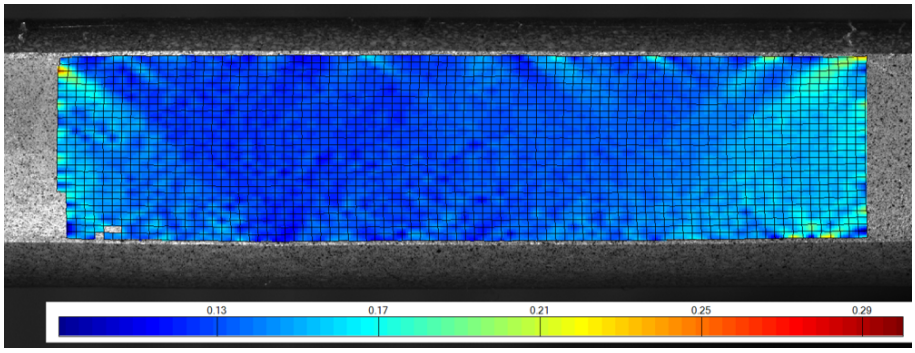

(b) *Position 2: Global stress and strain at 204 MPa and 0.15, respectively. As necking starts.*

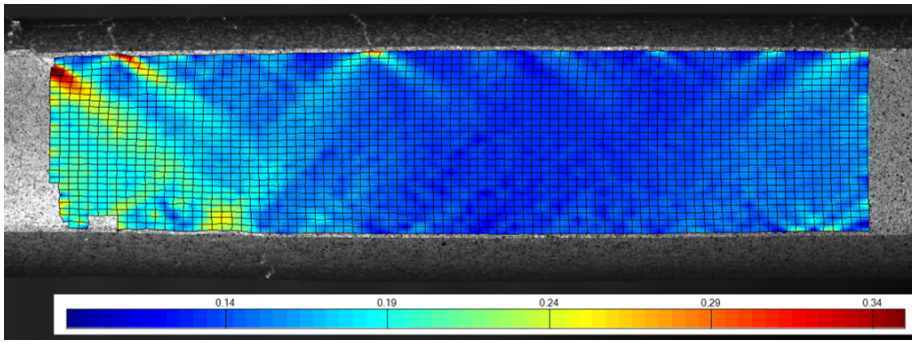

(c) *Position 3: Global stress and strain at 200 MPa and 0.17, respectively. Increasing localized strains.*

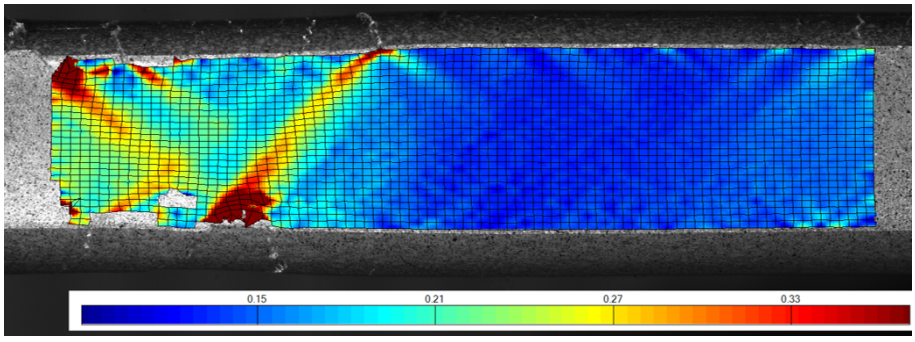

(d) *Position 4: Global stress and strain at 178 MPa and 0.19, respectively. Seconds before fracture.*

Figure 4.21: *DIC strain field images of the local strains experienced at different positions during tensile testing of CoEx1 - 180 µm. The positions 1 - 4 referees to the positions marked in figure 4.20.*

The stress-strain curve of CoEx2-Sc with an average sleeve thickness of 117 μm, where the positions of the strain field images were taken, can be seen in figure 4.22. The strain field images of the engineering strain over the flat surface of the specimen are presented in figure 4.23. During the DIC analysis, some blocks had to be removed due to changes in topography and lighting conditions.

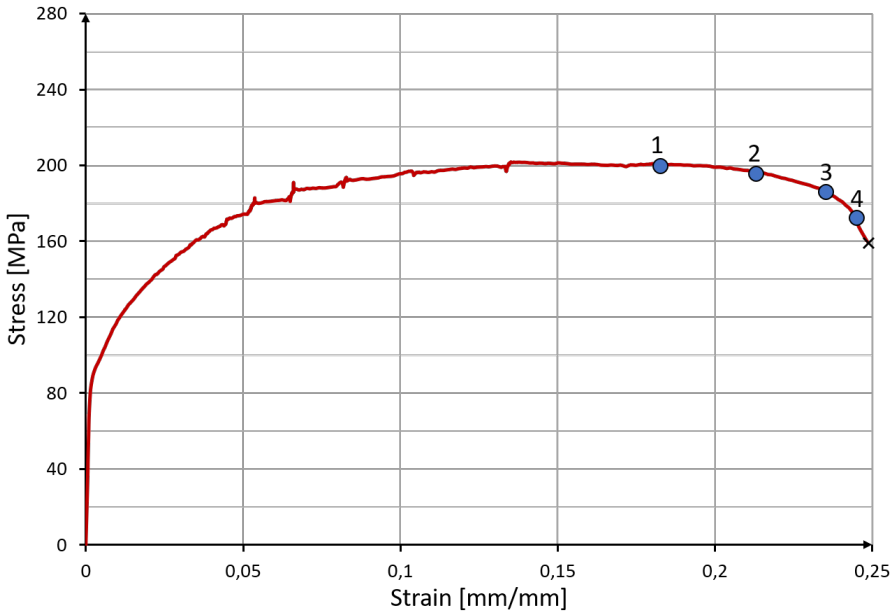

Figure 4.22: *Stress-strain curve of CoEx2-Sc-117 µm with four positions from where the DIC strain field images in figure 4.23 are taken.*

Position 1 in figure 4.23a shows the strain field at a global stress of 201, which close to the maximum stress measured. The global strain at this position was 0.18, but slightly higher strains of approximately 0.19 can be seen locally in the same crossed pattern seen previously. Some strain lines, with local strains above 0.2, can be observed close to the sleeve even before necking. As necking starts at a global strain of 0.21, the global stress declines to 196 MPa. The strain field of this situation can be seen in figure 4.23b. The first cracks nucleated can be seen inside the red circles. In the necking zone, the strain has increased locally to above 0.23 across the surface with lines 45° to the tensile direction. Some of the areas closest to the sleeve experienced strains up to 0.27. Necking continues and the global stress and strain reach 187 MPa and 0.23, respectively. The strain lines become larger with local strains of 0.27 spanning across the surface, as seen in figure 4.23c. The areas at the bottom, close to cracks, can be observed to experience strains above 0.31. A V-shaped strain field between the first three cracks nucleated, with increased local strains, can be seen. In the non-necked regions, the local strains were below 0.18. Figure 4.23d shows the strain field seconds before fracture. At this position, the global stress and strain were 173 MPa and 0.24, respectively. Strain lines,

commencing from cracks at the top and bottom, were almost connected with local strains of 0.33 reaching across the surface. Shortly after the fracture occurs along these lines, creating a 45° fracture surface.

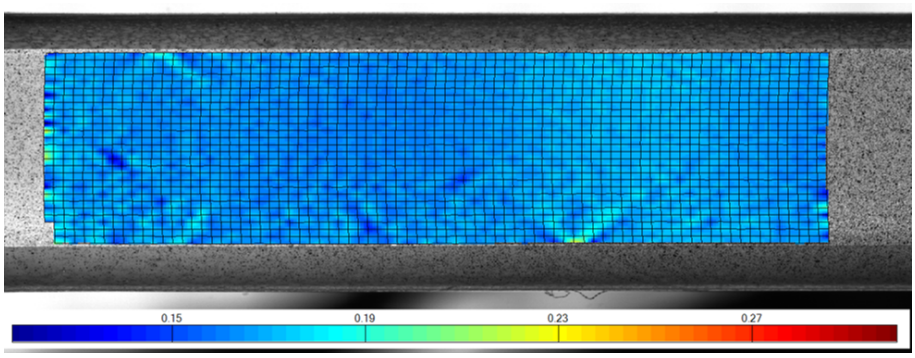

(a) *Position 1: Global stress and strain at 201 MPa and 0.18, respectively. Before necking.*

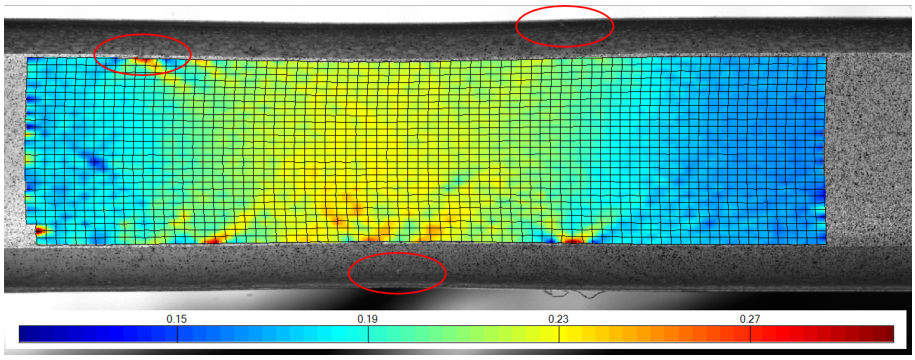

(b) *Position 2: Global stress and strain at 196 MPa and 0.21, respectively. Just as necking starts and the first cracks are observed inside the red circles.*

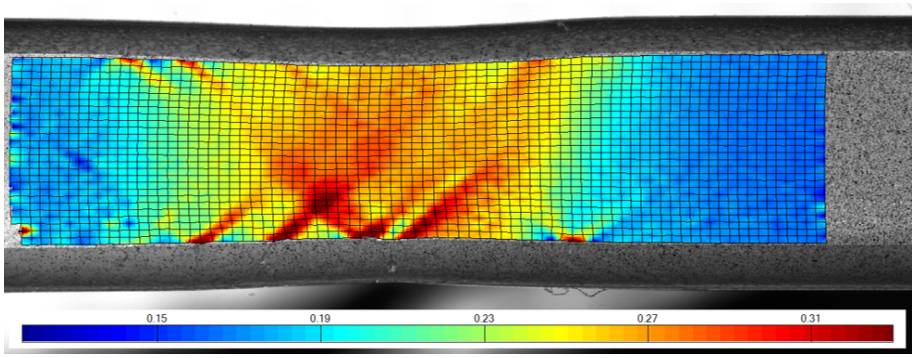

(c) *Position 3: Global stress and strain at 187 MPa and 0.23, respectively. Increasing localized strains.*

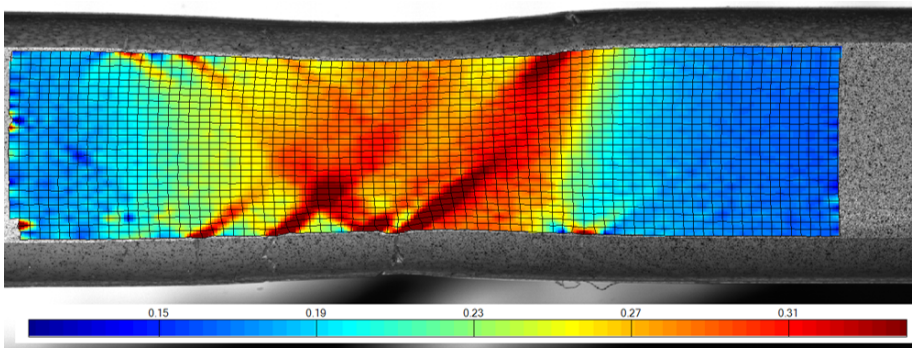

(d) *Position 4: Global stress and strain at 173 MPa and 0.24, respectively. Right before fracture occurred.*

Figure 4.23: *DIC strain field images of the local strains experienced at different positions during tensile testing of CoEx2-Sc - 117 µm. The positions 1 - 4 referees to the positions marked in figure 4.22.*

During tensile testing of CoEx1 and CoEx2-Sc specimens, it was observed that there were different behaviours in the sleeve deformation of specimens with approximately same sleeve thickness. This was first observed in the strain field images presented above. In order to investigate this phenomenon, images were captured at identical strains (figure 4.24) and stresses (appendix D) conditions of specimens with approximately the same sleeve thickness of CoEx1 and CoEx2-Sc. Figure 4.24 show specimens CoEx1 - 112 μm and CoEx2-Sc - 117 μm at 0.2 and 0.22 strain during tensile testing. It can be observed that with approximately the same sleeve thickness and strain conditions, the difference in the amount of cracks in the sleeve is apparent.

Comparing CoEx1 (figure 4.24a) and CoEx2-Sc (figure 4.24b) at 0.2 strain it can be seen that there was severe cracking in the sleeve for CoEx1 and none for CoEx2-Sc. For both specimens, necking has started at this strain. Even though CoEx2-Sc was subjected to higher stress (199 MPa), compared to CoEx1 (177 MPa), no cracks can be seen at this strain for CoEx2-Sc. During further necking and strain of 0.22, the cracks in CoEx1 has increased in size and fracture has initiated as seen in figure 4.24c. While for CoEx2-Sc, at the same strain, only a few cracks were observed. These observations were also the same for CoEx1 and CoEx2-Sc with a sleeve thickness of 180 μm and 182 μm, respectively. This can be seen in appendix D. These figures show both specimens at maximum stress measured of 205 MPa and 191 MPa during necking. Two cracks in the sleeve were visible for CoEx1 - 180 μm (figure D.1a) at maximum stress, while one relatively small crack was observed for CoEx2-Sc - 182 μm (D.1b). During necking there was still only one crack for CoEx2-Sc - 182 μm (figure D.1d), but this crack grew larger and were responsible for fracture of this specimens. For CoEx1 - 180 μm (figure D.1c) several cracks in the sleeve has nucleated, causing fracture.

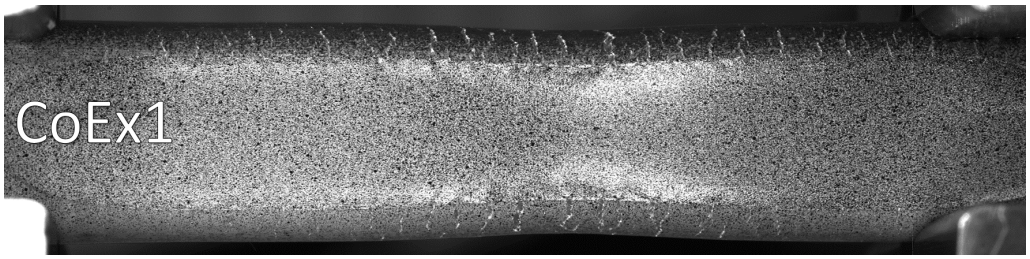

(a) *Image taken of a specimen from CoEx1 with a sleeve thickness of 112 µm being subjected to 177 MPa and 0.2 strain.*

(b) *Image taken of a specimen from CoEx2-Sc with a sleeve thickness of 117 µm being subjected to 199 MPa and 0.2 strain.*

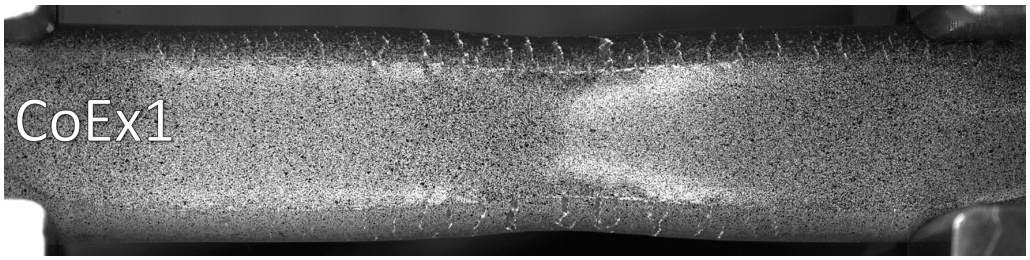

(c) *Image taken of a specimen from CoEx1 with a sleeve thickness of 112 µm being subjected to 169 MPa and 0.22 strain.*

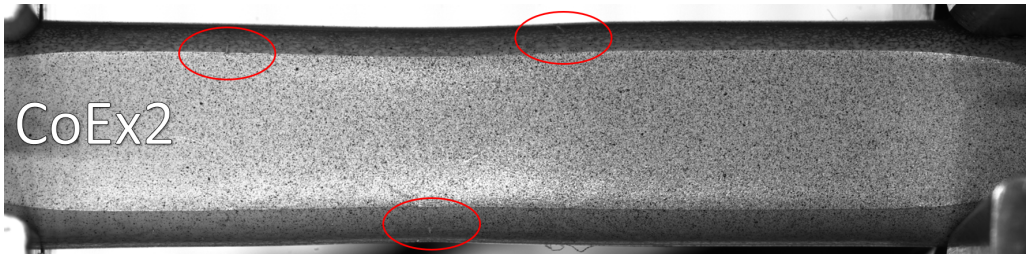

(d) *Image taken of a specimen from CoEx2-Sc with a sleeve thickness of 117 µm being subjected to 194 MPa and 0.22 strain. Small cracks can be observed inside the red circles.*

Figure 4.24: *Four images of captured with the DIC to show the difference in sleeve behaviour of CoEx1 - 112 µm (**(a)** and **(c)**) and CoEx2-Sc - 117 µm (**(b)** and **(d)**) at 0.2 strain (**(a)** and **(b)**) and 0.22 strain **(c)** and **(d)**).*

The results from the investigation of local strain with five parallel vector lines, as explained in figure 3.15, can be seen below. Figure 4.25 shows the last seconds during the tensile test of CoEx1 - 520 μm before fracture. Figure 4.26 shows the same for CoEx2-Sc - 431 μm. The strain behaviour of the five vector lines for a larger

time frame for both specimens can be seen in appendix E. For both specimens, there was no significant difference in strain for the sleeve and core before crack nucleation. The first crack in CoEx1 - 520 μm nucleated 435 seconds into the test. From figure 4.25, it can be observed that the strains in the sleeve and core starts to mismatch. Once the crack reaches the core at 440 seconds, the strain in the sleeve stabilizes at approximately 0.122 while in the core it rapidly increases. After 448 seconds, line 3 (green) gets affected by changes in topography and lighting conditions. That's why it suddenly goes out of the graph. Fracture occurs after 460 seconds and at this point, the maximum difference in strain in the sleeve and core were 0.02 in favour of the core. During tensile testing of CoEx2-Sc - 431 μm, the same phenomenon when it comes to sleeve and core strain behaviour can be observed in figure 4.26. The first crack nucleates in the sleeve after 336 seconds and reaches the core at 440. Once it reaches the core, the crack starts to propagate along the sleeve and core interface. As the crack grows, the strain mismatch increases and after 354 seconds the specimens begins to slowly fracture with increasing strain rates in the core. The fracture occurred after 380 seconds with a maximum difference in the strain of 0.014, in favour of the core.

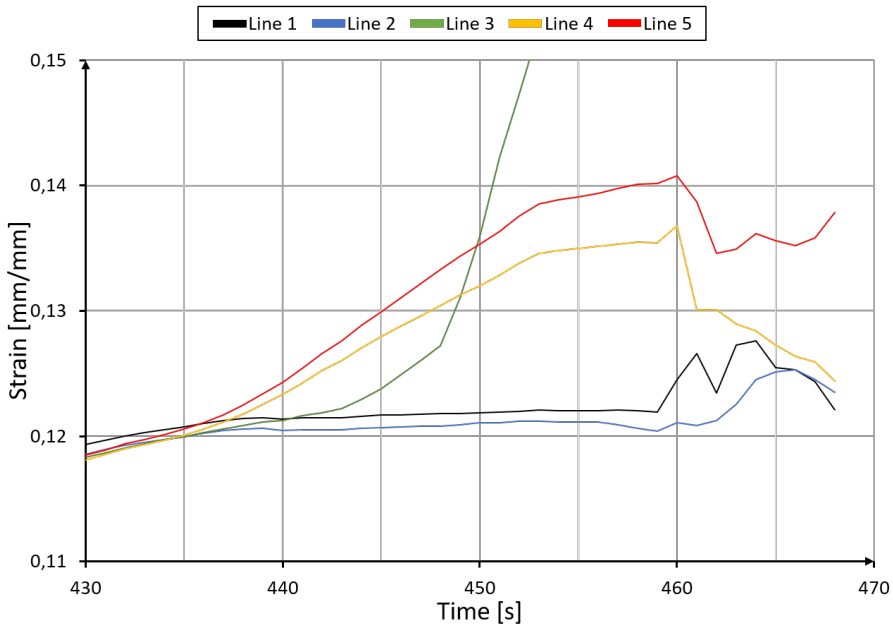

Figure 4.25: *Graph showing the local strains measured along the five vector lines in the sleeve (black and blue) and core (green, yellow and red) during tensile testing of CoEx1 - 520 mum. This graph shows the last seconds before fracture, occurring after 460 seconds.*

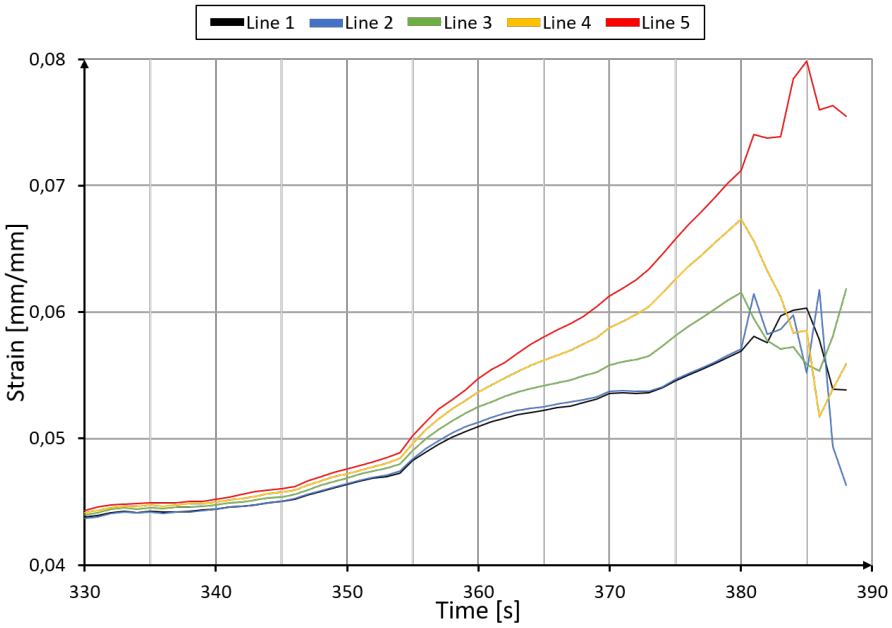

Figure 4.26: *Graph showing the local strains measured along the five vector lines in the sleeve (black and blue) and core (green, yellow and red) during tensile testing of CoEx2-Sc - 431 mum. This graph shows the last seconds before fracture, occurring after 380 seconds.*

4.3.4 Fractography of Co-extruded Tensile Specimens

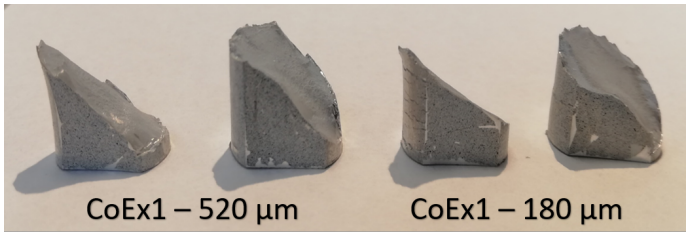

(a) *Image of fractured specimens of CoEx1 - 520 µm and CoEx1 - 180 µm.*

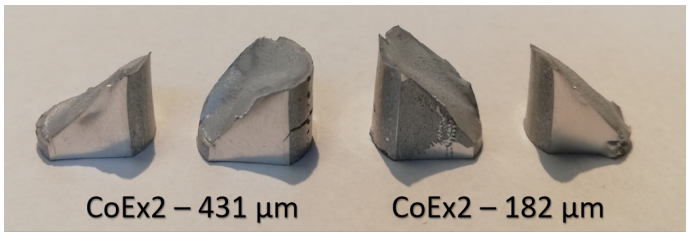

(b) *Image of fractured specimens of CoEx2-Sc - 431 µm and CoEx2-Sc - 182 µm.*

Figure 4.27: *Image of the fracture specimens of* ***(a)*** *CoEx1 and* ***(b)*** *CoEx2-Sc whom have been taken to the SEM for fractography.*

An image of the fracture specimens cut from CoEx1 and CoEx2-Sc can be seen in figure 4.27a and figure 4.27b, respectively. From these images, it can be seen that

all specimens have a 45° fracture surface. That was the case for all specimens tested during tensile tests. Except for those who fractured in the tension grip. It should be noted that all specimens examined have been solutionized and aged. Fractography done in the SEM of CoEx1 and CoEx2-Sc with different sleeve thickness can be found in figures 4.28 - 4.31.

From the overview image of CoEx1 - 520 μm in figure 4.28a, no separation between the core and sleeve material can be observed. Indications of shear lips can be seen in the sleeve material. Looking at the core material in figure 4.28b, a dimpled fracture surface can be seen with several large voids and some shear regions. Inside some of the voids, it's possible to see the inclusions which nucleated the voids. These are the typical signs of a ductile fracture. In the sleeve material (figure 4.28c), a very fine dimpled fracture surface with many small microvoids can be observed. Indicating ductile fracture of the sleeve in this area. At the interface between the core and sleeve material, figure 4.28d, two to three different kinds of fracture surfaces can be seen. In the core material to the left shear, elongated dimples and voids can be observed. At the interface, in the middle of the image, a very fine dimpled fracture surface with microvoids can be seen. This indicates a ductile separation of the core and sleeve. To the right in the image, the sleeve exhibits a fine dimpled intergranular fracture surface.

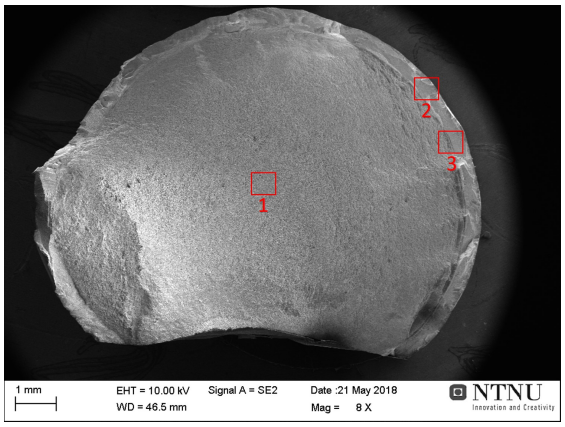

(a) Overview image of fractured CoEx1 - 520 µm at 8X magnification.

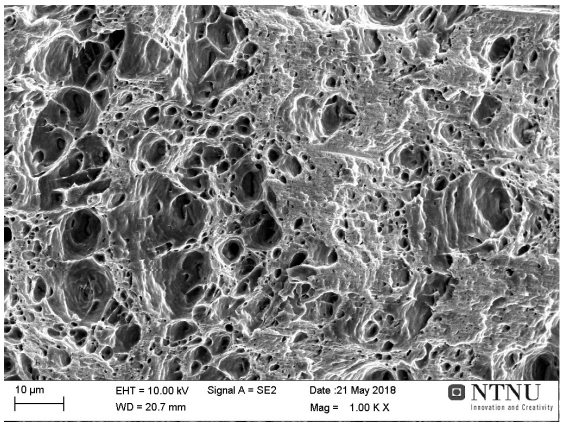

(b) Image of the core material at 1000X magnification.

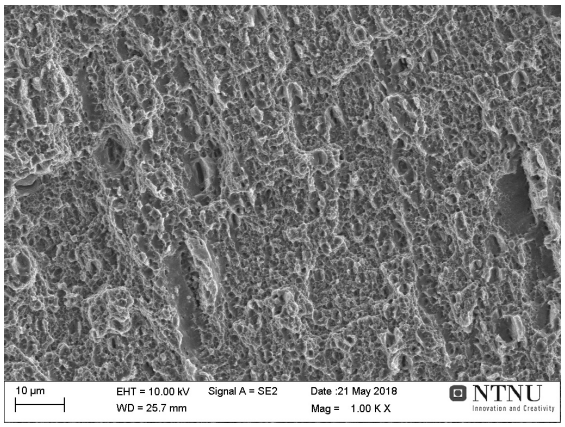

(c) Image of the sleeve material at 1000X magnification.

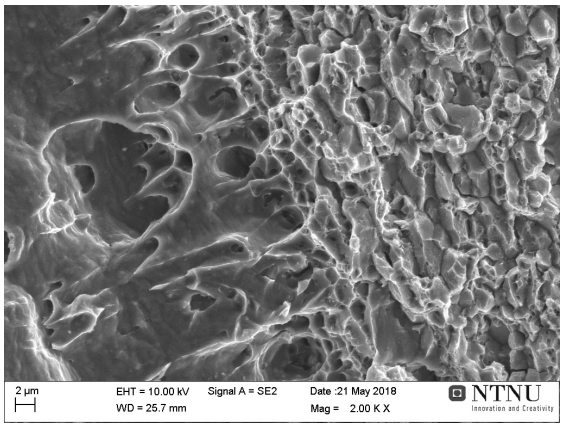

(d) Interface at 2000X magnification. Core to the left and sleeve to the right.

Figure 4.28: *Images of CoEx1 - 520 µm from the SEM showing* ***(a)*** *an overview of the fracture surface,* ***(b)*** *core material,* ***(c)*** *sleeve material and* ***(d)*** *the interface between the core and sleeve material.*

The overview image of CoEx1 - 180 μm in figure 4.29a shows that neither this specimen display separation between the core and sleeve material. The core features the typical signs of ductile fracture surface with large dimples and voids, as seen in figure 4.29b. In this specimen, another fracture surface was observed in the sleeve material. Several areas along the sleeve exhibited multifaceted, river-like fracture surface of multiple lines converging in the same direction. This indicates cleavage fracture in the sleeve material. The cleavage pattern implies that cleavage has occurred along the sleeve. CoEx1- 180 μm was the only specimen where cleavage fracture was found. These fracture surfaces can be seen in the right part of figure 4.29c and figure 4.29d. In the same images, the interface between the core and sleeve is shown. The core, on the topological top to the left, displays shear, dimples and voids. Along the fracture surface of the interface, small dimples and voids are

observed. This reveals that there has been a ductile fracture separating the core and sleeve material. In figure 4.29d, small voids in the sleeve are also observed.

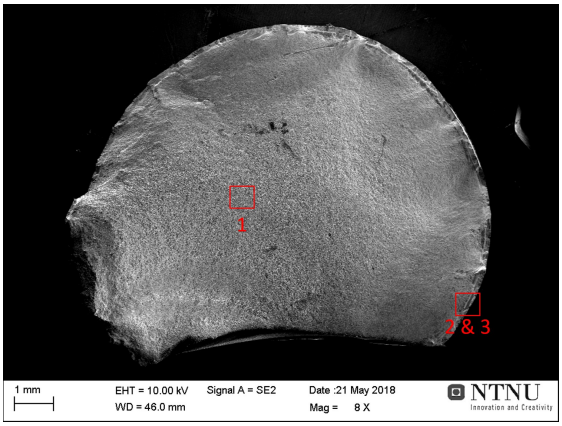

(a) *Overview image of fractured CoEx1 - 180 µm at 8X magnification.*

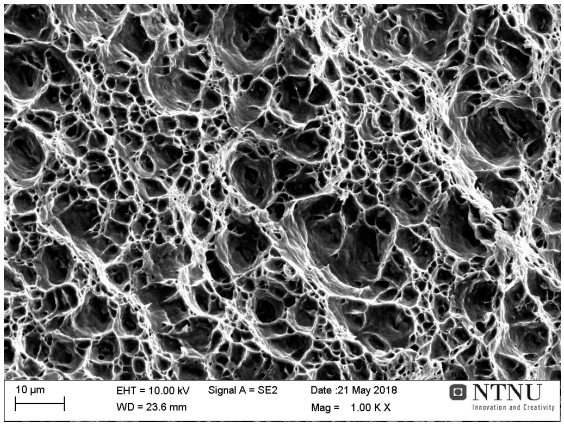

(b) *Image of the core material at 1000X magnification.*

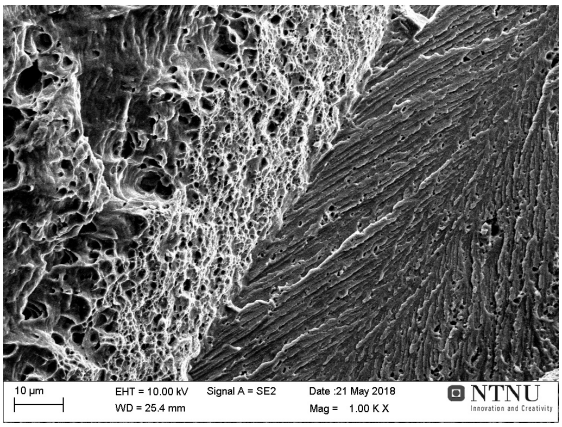

(c) *Interface at 1000X magnification. Core to the left and sleeve to the right.*

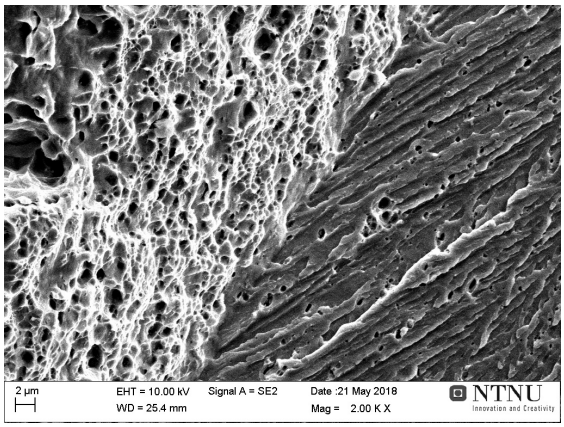

(d) *Interface at 2000X magnification. Core to the left and sleeve to the right.*

Figure 4.29: *Images of CoEx1 - 180 µm from the SEM showing* ***(a)*** *an overview of the fracture surface,* ***(b)*** *core material and* ***(c)-(d)*** *the interface between the core and sleeve material at two different magnifications.*

Some separation of the sleeve and core material can be seen in the bottom left of the overview image of CoEx2-Sc - 431 μm in figure 4.30a. The core displayed the same ductile fracture as previously described. The sleeve material of in this specimen exhibited two different fracture surfaces. Figure 4.30b, which was an image taken in the middle of the sleeve, displays a very fine dimpled intergranular fracture surface. Some microvoids can be observed in the right part of the image. The sleeve also displayed evidence of ductile fracture, as seen in figure 4.30c. In this figure, a fracture surface of very fine dimples and microvoid can be observed. Inclusions that have caused the microvoid formation can be seen inside some of the voids. At the interface (figure 4.30d), a shear fracture surface can be seen along the

core down towards the interface. At the interface itself, a transition from large voids in the core material to microvoids in the sleeve. Once again, indicating a ductile separation of the two dissimilar alloys. In the top right corner, the sleeve features signs of an intergranular fracture.

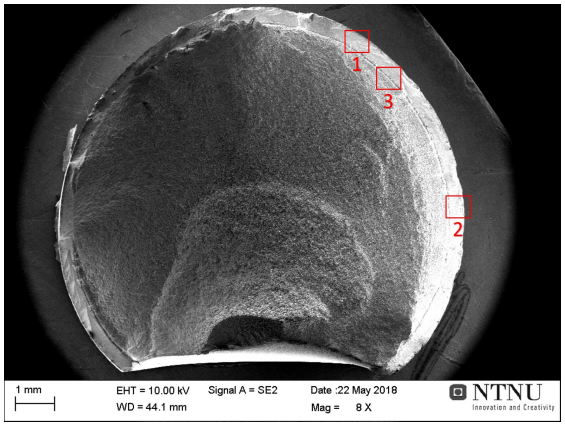

(a) *Overview image of fractured CoEx2-Sc - 431 µm at 8X magnification.*

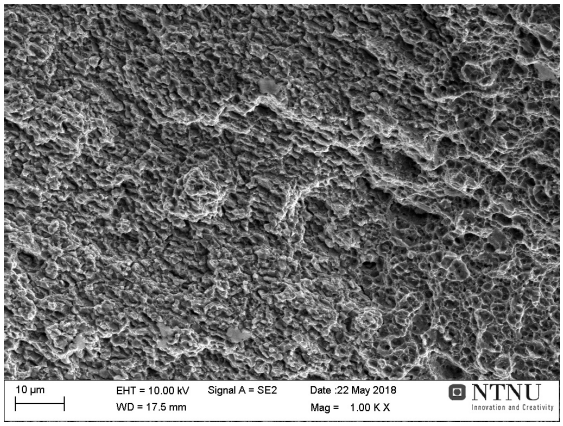

(b) *Image of the sleeve material at 1000X magnification.*

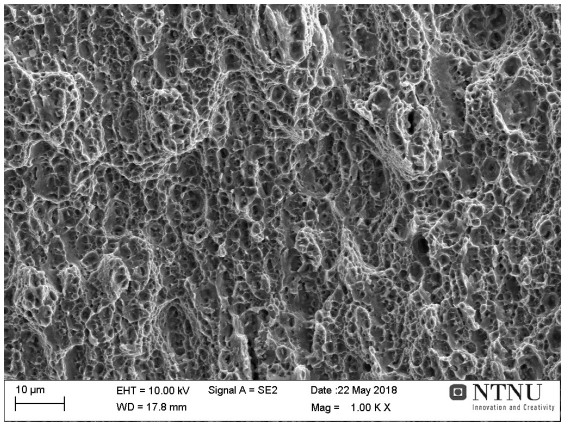

(c) *Image of the sleeve material at 1000X magnification.*

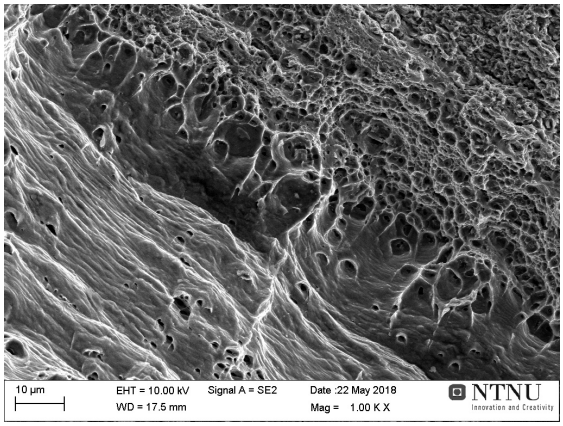

(d) *Interface at 2000X magnification. Core at the bottom and sleeve at the top.*

Figure 4.30: *Images of CoEx2-Sc - 431 µm from the SEM showing* ***(a)*** *an overview of the fracture surface,* ***(b)*** *core material,* ***(c)*** *sleeve material and* ***(d)*** *the interface between the core and sleeve material.*

The overview image of CoEx2-Sc - 182 μm in figure 4.31a shows no separation of the core and sleeve material and ductile fracture of the core material. The sleeve material displays indications of ductile fracture as well, with very fine parabolic dimples and microvoids as seen in figure 4.31b. Close to the interface (figure 4.31c), the core exhibits a combination shear, voids and elongated dimples. At the contact between the core and sleeve material, the fracture was ductile with large dimples in the at the core side and very fine dimples at the sleeve side. This can be observed in figure 4.31d.

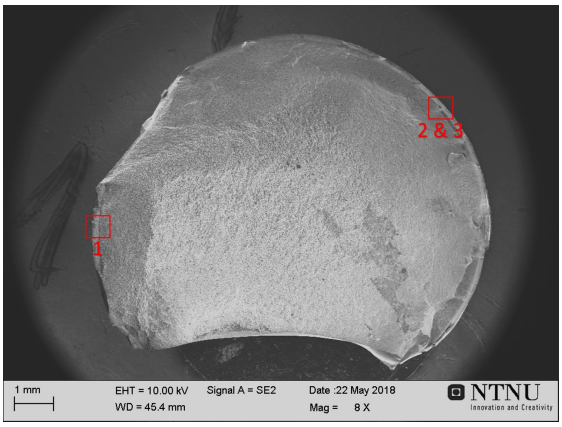

(a) *Overview image of fractured CoEx2-Sc - 182 µm at 8X magnification.*

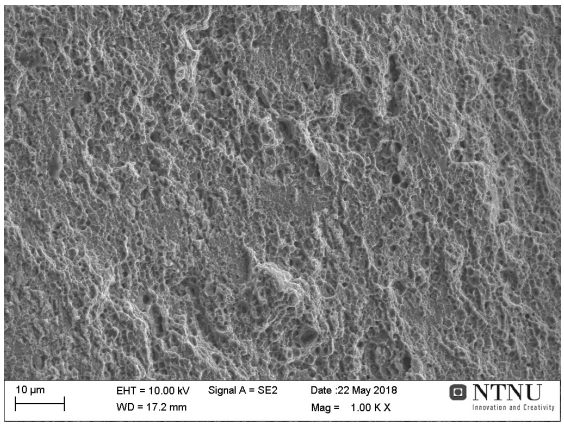

(b) *Image of the sleeve material at 1000X magnification.*

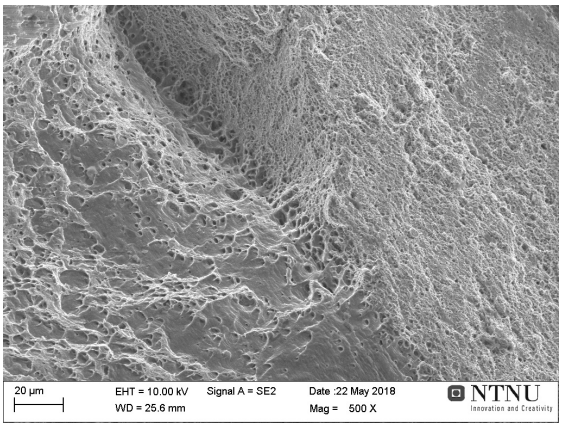

(c) *Interface at 500X magnification. Core to the left and sleeve to the right.*

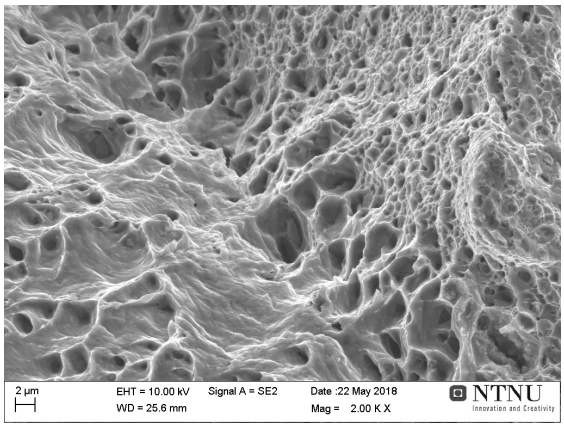

(d) *Interface at 2000X magnification. Core at the bottom left and sleeve at top right.*

Figure 4.31: *Images of CoEx2-Sc - 182 µm from the SEM showing* ***(a)*** *an overview of the fracture surface,* ***(b)*** *sleeve material and* ***(c)-(d)*** *the interface between the core and sleeve material at two different magnifications.*

5 Discussion

5.1 The Base Materials and Their Differences

The two dissimilar aluminium alloys, RS AA7090 and AA6082, have proven to exhibit vastly different mechanical properties on their own. For example, the average yield strength of aged RS AA7090 (683 MPa) was over six times higher than that measured for aged AA6082 (113 MPa). But the ductility of RS AA7090 was approximately one-third of that measured for AA6082, as seen in figure 4.14. There were some variations in the ductility, but this was most likely due to defects in the specimens. These differences in mechanical properties can result in difficulties of co-extruding these alloys. Both with regards to achieving bonding between the two alloys and uniform sleeve thickness. Especially when it comes the co-extrusion setup with a soft core/hard sleeve, as demonstrated by R. Sliwa [28] who investigated plastic zones during extrusion of metal composites. In their solutionized condition, the alloys have lower yield strength, but higher ductility. This corresponds to the theory that states that an increase in yield strength often comes at the cost of ductility.

Even though the two aged specimens of AA6082 have been cut from the same material and have been through the same heat treatment, they produced different stress-strain curves. It's unclear why this was the case, as there was not much at all that distinguishes the specimens. There was one difference when it comes to the gripping forced used during tensile testing. For AA6082 Aged 1, the gripping force was initially too low causing the tension grips to move. Once the gripping force was increased, the test continued as normal. The specimen AA6082 Aged 1 had measured higher strength levels than AA6082 Aged 2 even before the movement of the grips occurred. It is quite possible that the results from AA6082 Aged 1 were within the expected standard deviation for tensile testing this alloy. But due to the shortage of materials, it was not possible to produce more tensile specimens of AA6082. The same goes for the other alloys as well.

Even though RS AA7090 has been rapidly solidified, the yield strength and tensile strength was inferior to that displayed by DC AA7090, as seen in chapter 4.3.1. As both parallels within the same material produced almost identical stress-strain curves, the results seem conclusive. During the creation of precipitation hardening curves, the DC AA7090 displayed superior hardness as well. There was some uncertainty as to why the RS AA7090 was below whats expected, but it might have something do to with differences in alloying elements and process parameters. As can be seen from table 2.1, there was some variation in the amount of alloying elements for the two. DC AA7090 has a greater amount of Zn, which is one of

the main elements contributing to precipitation hardening. It does also have fewer impurity elements, such as Si and Fe, than RS AA7090. These alloying elements are often associated with a reduction of mechanical properties. The geometry of the billets used during extrusion of the two was not identical either. The rod of RS AA7090 was made by extruding a flaky billet of compacted material with a diameter of 35 mm, while DC AA7090 was extruded using a 40 mm diameter smooth billet. There were also differences in the extrusion parameters, as seen in appendix B. DC AA7090 has been extruded with a lower container and ram temperature, as well as higher extrusion speeds than RS AA7090. These parameters have resulted in a higher extrusion force, thus may have caused higher degree of plastic deformation and strain hardening of DC AA7090 rods.

The solutionized specimen of DC AA7090 seems to experience the Portevin-Le Chatelier (PLC) effect [35]. The PLC effect is caused by diffusion of solute atoms to dislocations, which pins the dislocation. This causes an increase in the stress and as the stress increases the dislocations are able to break away from the solute atoms. This causes fluctuations in the stress-strain curve and may explain the behaviour of the solutionized specimen of DC AA7090, as seen in figure 4.10.

Because of the limited time available at SINTEF Raufoss Manufacturing, where the extrusion and co-extrusion were done, production of a rod of 100% RS AA7090-Sc was not performed. Which means that the mechanical properties of this alloy are yet to be found.

5.2 The Heat Treatment Process and Response to Precipitation Hardening

As seen from the chapter 2.1.2 and 2.1.3, the two alloys in the 6xxx- and 7xxx series has vastly different heat treatment processes to achieve maximum strength. The heat treatment process in this project was designed to achieve maximum strength for the AA7090 alloy, but the temperatures were tweaked with the hopes of obtaining some increase of strength of AA6082 as well. That was why a one-stage solution heat treatment at 470°C and 140°C precipitation heat treatment temperature was chosen. The 90 minutes of slow heating from 25°C to 470°C during the solution heat treatment was selected in order to avoid melting of particles in the alloy due to rapid temperature changes. The increased solution heat treatment temperature may also allow for easier dissolution of alloying elements, which might be needed due to a large amount of alloying elements in the alloy. The use of air circulation furnaces was chosen because they're the most common types of furnaces used in the industry. In hindsight, using oil baths may have been more beneficial for experimental purposes. But the use of air circulation furnaces was considered to not have affected the results.

After solution heat treatment of DC AA7090 and precipitation heat treatment at 140°C for 5 minutes, the results show an increase in hardness from 116 HV1 to 159 HV1. This indicates a high driving force for precipitation and a solid hardness response in the alloy. As S. Koch et. al [36] suggested, the formation of solute clusters and vacancy-rich clusters (VRC) may already from immediately after quenching following the solution heat treatment. These solute clusters and VRC are the precursors of GP(I)- and GP(II)-zones, respectively. That was why the time at room temperature for all samples was kept constant. As the samples were inserted into the oven for precipitation heat treatment, rapid nucleation of GP(I)- and GP(II)-zones occurs. The GP(I)-zones are less stable at temperatures above 60°C and will start to dissolve, which is why the hardness does not increase at as fast after the initial 5 minutes. GP(II)-zones forms at higher temperatures and are more stable. These zones will during long exposure to 140°C transform into M'-particles, causing a continued increase in hardness. Further nucleation of M'-particles results in a peak hardness after just 4 hours, and up to 10 hours, of almost twice of that measured in the solutionized condition. After longer exposure, the M'-particles coarsens and the formation of M-particles starts. These particles are not able to strengthen the material efficiently, causing a decrease in hardness [37]. That's when the overaged condition is reached. As seen from the results, the DC AA7090 samples had achieved a maximum hardness higher than that measured for both RS AA7090 and RS AA7090-Sc in the sleeve of CoEx1 and CoEx2-Sc, respectively. The reasons for this difference in properties are discussed in chapter 5.1.

The sleeve of CoEx1 and CoEx2-SC has likely experienced the same precipitation sequence as discussed above, but they have not reached the same hardness as DC AA7090. The precipitation hardening response in the sleeve of both CoEx1 and CoEx2-Sc followed the same response pattern as seen in DC AA7090, but at slightly lower hardness levels. Both sleeves achieved maximum hardness after 8 hours of precipitation heat treatment. After 8 hours, both alloys get into the overaged condition with a reduction in hardness.

Another discovery, though unfortunate, was that the core material (AA6082) started to experience an increase in hardness just as the sleeve materials got into the overaged condition. Compared to G. Mrówka-Nowotnik et. al [38] who solutionized AA6082 at 575°C and aged at 125°C, the difference in solution heat treatment temperature becomes evident. They achieved a hardness of 105 HV1 after 8 hours at 125°C, while in this project the hardness was measured to 86 HV1 after 40 hours at 140°C. As the precipitation heat treatment process was terminated after 40 hours before the AA6082 reached its overaged condition, it could be likely that the hardness could exceed 100 HV1. But a heat treatment process that takes several

days would not be practical in commercial use. As stated above, the goal was to achieve maximum strength in the sleeve material. That was why 8 hours at 140°C was chosen as the ageing time for the co-extruded rods.

5.3 Microstructure and Effect of Sc Additions

Another discovery during the heat treatment was that after solution heat treatment, the edge of the sleeve of CoEx1 and CoEx2-Sc had different microstructure. A comparison of the microstructures can be seen in figure 5.1. CoEx1 seems to have experienced recrystallization and grain growth in the sleeve material after being solutionized at 470°C. From the microscopic images, it can be observed that the edge of the sleeve has experienced the most recrystallization and grain growth. This was most likely due to the fact that the outer parts of the co-extruded rod experienced the most deformation during extrusion. Causing more dislocations and strains in this area, which increases the driving force for recrystallization. As seen in figure 5.1b, CoEx2-Sc does not exhibit recrystallization and grain growth in the sleeve as that observed for CoEx1. This implies that the addition of Sc to this alloys, with the combination of Zr, have had a positive effect on the inhibiting of recrystallization and grain growth. These results are in line with the work done by Y. W. Riddle et. al [39], who investigated the effect of adding Sc to aluminium alloys. They discovered that an aluminium alloy containing 0.12 wt% Zr had no ability to resist recrystallization when exposed to 400°C for 1 hour. While an aluminium alloy with the combination of Sc (0.2 wt%) and Zr (0.12 wt%) showed no signs of recrystallization even after 1 hour at 590°C. The addition of Sc to the AA7090 alloy in this project has caused the formation of $Al_3(Sc_{1-x}, Zr_x)$ dispersoids, improving the resistance to recrystallization. Beyond the recrystallized sleeve edge of CoEx1, all of the rods displayed a fine microstructure with equiaxed grain with a size below 10 μm in the transverse cross-section and a fibrous microstructure in the longitudinal cross-section in the solutionized condition.

There were difficulties with achieving a perfectly anodized microstructure during anodizing of the co-extruded samples in the as-extruded condition, as seen in figure 4.9. The sleeve material seemed to be full of particles, which seems to be "attacked" during the anodizing process. It's reasonable to assume that these particles have formed during the extrusion process due to slow cooling and that they contain Zn and Mg, which are the main alloying elements. As seen in figure 2.1, the solubility of Zn and Mg rapidly decreases with temperature. Large particles containing Zn and Mg will be less noble than the matrix of Al, acting as an anode when submerged in an electrolyte. Causing degradation of these large particles instead of anodizing of the aluminium matrix. When the samples were solutionized, these large particles

have dissolved into solid solution with the matrix. Making it easier to achieve a perfectly anodized surface.

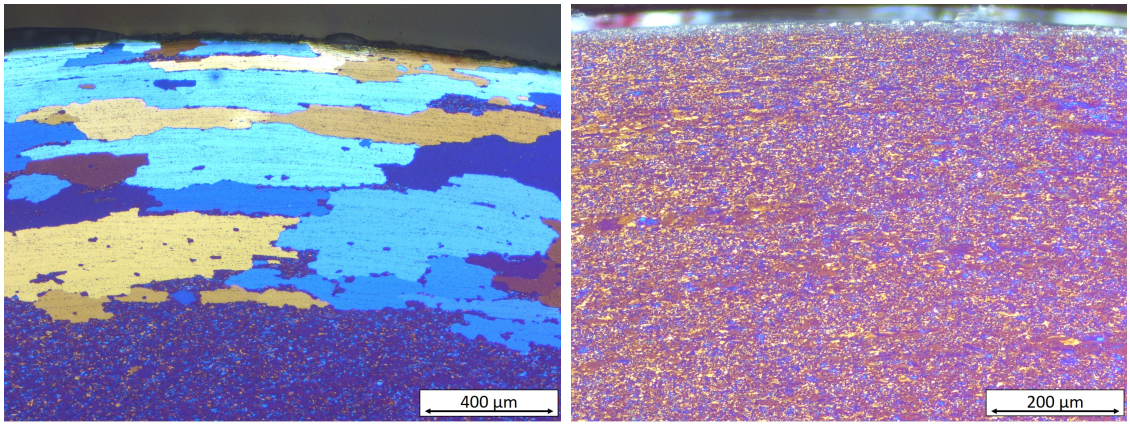

(a) *Transverse cross section of sleeve edge of CoEx1 at 5X magnification.*

(b) *Transverse cross section of sleeve edge of CoEx2-Sc at 10X magnification.*

Figure 5.1: *Microstructural images of the sleeve edge of* ***(a)*** *CoEx1 and* ***(b)*** *CoEx2-Sc.*

5.4 Co-Extrusion Process and Sleeve Thickness

Billets produced from cold compacting the melt spun ribbons were relatively porous and flaky, as seen in figure 3.4. It was recognized that the more ribbons that were filled into the steel pipe during compacting, the more compact and larger diameter the final aluminium billet got. That was why R1 got a diameter of just 35 mm, due to the lack of melt spun material left of its batch. This should be taken into consideration if more compaction of ribbons were to be done in the future.

The setup used for co-extrusion was designed to create a rod with a soft core and hard sleeve. As previously discussed in chapter 5.1, this setup is one of the more difficult once when it comes to flow of the dissimilar alloys. Billet designs with a hole in the sleeve material and a guide pin on the softer core material were done in order to reduce the initial cramping caused by the hard sleeve. During the co-extrusion trials in this project, only one sleeve/core weight ratio and die geometry was used. Experimenting with different weight ratios could also have been interesting with respect to how that would have affected the sleeve thickness. Due to difficulties with optimizing the co-extrusion process, failed attempts and material shortage, experimenting with the weight ratio was not done in this project. The same goes for die geometry. Another die geometry might have been beneficial when it comes to achieving a uniform sleeve thickness throughout the co-extruded rods.

As seen from appendix A, table 3.3 and table 3.4, there were some variation in the parameters for the four successful co-extrusion trials. The main differences

being ram temperature, container temperature and extrusion speed. Also the fact that the rod of R2 contains RS AA7090 as the sleeve material, while R3 and R4 rods use RS AA7090-Sc as sleeve material. Reviewing the parameters recorded during the co-extrusion trials and the sleeve thickness measured of each rod, it's possible to see some indications of which parameters that may affect the sleeve thickness and quality of the rods. The recommendations of previous work [32] by reducing temperature and extrusion speed to avoid fracturing were followed and resulted in a better quality of the co-extruded rods. The co-extruded rod of R2 part 2 and R3 Part 1 had no cracks in the surface. While R3 part 2 and R4 part 1 got cracks in the surface layer at the end and middle of the co-extrusion process, respectively. This indicates that a container temperature of 460°C was at the edge of what the sleeve material could handle before cracking. Especially as the sleeve thickness becomes thinner. Of the co-extruded rods with the same sleeve material, RS AA7090-Sc, the one extruded at the lowest container temperature was the one that achieved the best surface quality and fastest stabilized at a lower sleeve thickness. This shows that co-extrusion of these aluminium alloys can be done at temperatures down to 440°C without any problems. The sleeve thickness was continuously decreasing for all the co-extruded rods. That implies that there might not be enough sleeve material to maintain an even sleeve thickness throughout the rod. As seen by the microstructural observations and tensile testing of the co-extruded rods, excellent metallurgical bonding between the two dissimilar alloys have been obtained. From the DIC analysis and fractography, there was no separation of the two alloys. Unless for one occasion where a crack that nucleated in the sleeve propagated along the interface as it reached the core.

The exit temperatures measured for all successful co-extruded rods were in the same area of approximately 400°C. But as stated in the experimental part, the measurements of the exit temperature were done manually and 20 cm below the actual die opening. Due to the fact that aluminium has a relatively high thermal conductivity, the temperature may have changed substantially by the time it reaches the spot where it was measured. To get a better view of the exit temperature, a thermocouple should be mounted directly below die that continuously measures the temperature. From the figures in appendix A, it can be seen that the co-extrusion process often took more than five minutes from start to finish. This means that the rods have most likely experienced relatively slow cooling after leaving the container, causing the formation of large heterogeneously distributed particles as discussed in chapter 5.3.

5.5 Tensile behaviour of Co-Extruded Rods and Effect of Sleeve thickness

During tensile testing of the co-extruded rods, specimens with varying sleeve thickness were tested. The five tensile specimens of CoEx1 had average sleeve thickness ranging from 112 μm to 831 μm, while CoEx2-Sc had eight specimens ranging from 62 μm to 1167 μm. The three tensile specimens of CoEx2-Sc with the highest sleeve thickness failed due to the force of the tension grips and were excluded from the results. After lowering the gripping force, more successful results were achieved. As the modified specimen geometry used was not according to standards and tension grips moving during the tests, it was not possible to obtain mechanical properties that are comparable to those of the literature. That was why the maximum stress, comparable to σ_{TS}, was used in this project. Due to the material shortage, it was not possible to test several parallels with the same sleeve thickness of the same material.

As the sleeve material of RS AA7090 contributes to a small amount of the total volume fraction, the properties of the co-extruded rods were dominated by those of the AA6082 core material. From the stress-strain curves of aged CoEx1 specimens in figure 4.15, the effect of increasing sleeve thickness on the maximum stress was evident. The addition of an 831 μm sleeve of RS AA7090 has increased the strength from 200 MPa for 100% AA6082 to 259 MPa. If it's assumed that a specimen contained 100% AA6082 (0 μm sleeve thickness), one specimen containing 100% RS AA7090 (6000 μm sleeve thickness). The relationship between sleeve thickness and maximum stress can be plotted as seen in figure 5.2. A straight, dotted line is drawn between the average maximum stress measured for AA6082 and RS AA7092. It is important to highlight the fact that the specimens are plotted with their average sleeve thickness, which means that they have areas that are below the average. These areas with thinner sleeve thicknesses are the limiting factors of the specimens. Which means that the points in the figures should, in reality, be plotted at a slightly lower thickness. From figure 5.2b it can be observed that the maximum stress has an almost linear relationship with the sleeve thickness. This corresponds to the theory about tensile testing of continuous and aligned fibre reinforced composites [7]. If the sleeve material of RS AA7090 is considered as the fibre and AA6082 as the matrix, equation 8 can be used to calculate the strength of the composite. This equation is a version of the 'rule of mixture' concept often used to predict properties of composite materials. In this equation, σ_c and σ_f is the maximum stress of the composite and fibre, respectively. While V_f is the volume fraction of fibre material and σ_m is the stress of the matrix when the fracture in the sleeve occurs.

$$\sigma_c = \sigma_m(1 - V_f) + \sigma_f V_f \tag{8}$$

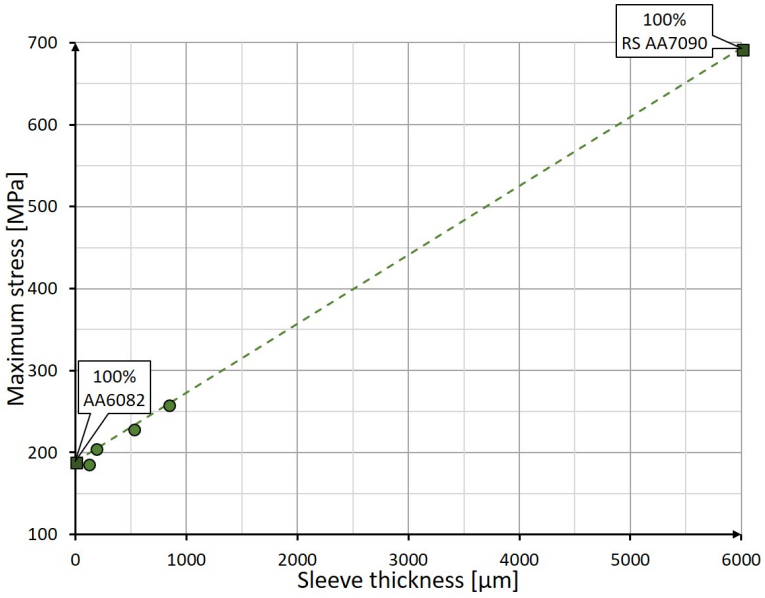

(a) *Maximum stress vs average sleeve thickness from 0 - 6000 µm.*

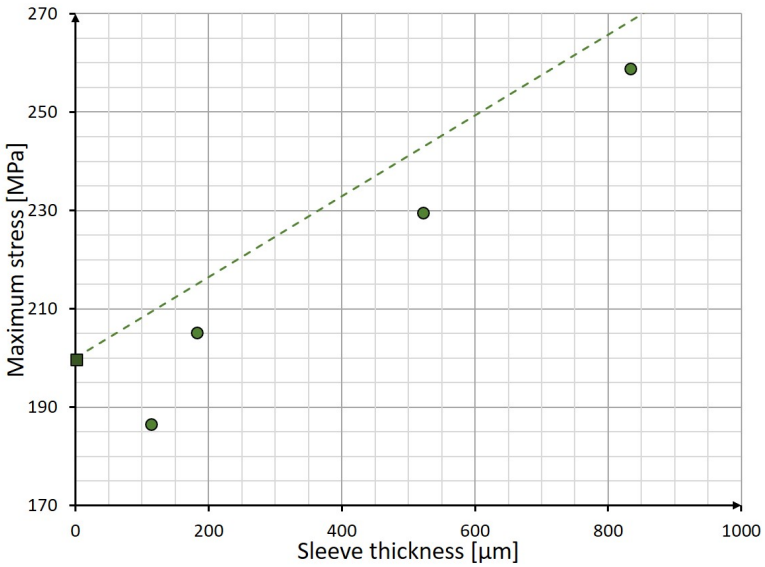

(b) *Maximum stress vs average sleeve thickness from 0 - 1000 µm.*

Figure 5.2: *Maximum stress measured during tensile testing plotted against the average sleeve thickness of the tensile specimens. The co-extruded specimens are circular while normal tensile specimens are squared, where the one at 0 µm is AA6082 and RS AA7090 is plotted at 6000 µm. Figure* ***(a)*** *shows the whole graph from 0 - 6000 and* ***(b)*** *shows a zoomed in part of the low sleeve thickness region.*

Fracture of the fibres is often associated with the onset of failure of the composite [7]. This was also the case for the co-extruded rods. As the thin sleeve material

reached its load and strain carrying capacity, cracking of the sleeve started. If the stresses were far above that capable of the core material, fracture occurs rapidly. For specimens with a thin sleeve thickness, the core material was capable of carrying the stress after the sleeve failed. But due to the fact that the surface has initiated cracks, stresses increased locally for the core material. Resulting in fracture at strains lower than that measured for AA6082.

These results tie well with previous studies done by D.R. Lesuer et al. [40], who investigated the mechanical behaviour of laminated metal composites. They concluded that the ductility could not be predicted by the rule of mixture and that the ductility was controlled by the least ductile material.

As explained in chapter 5.1, there were not produced any material of 100% RS AA7090-Sc. Which means that a direct comparison between the two base materials cannot be made. But for the tensile specimens of CoEx2-Sc, the effect of increasing sleeve thickness on the maximum stress can be seen in figures 4.17 and 4.18. Even though some of the specimens failed. The relationship between the maximum stress and average sleeve thickness of CoEx1 and CoEx2-Sc is shown in figure 5.3. From this figure, it can be observed that the two specimens of CoEx2-Sc with the lowest sleeve thickness achieved higher maximum stress than that measured for CoEx1 - 117 μm. This might have something to do with the difference in sleeve behaviour, as seen in figure 4.24. The nucleation of several cracks in the sleeve of CoEx1 - 112 μm has caused it to fracture at lower stress. While for CoEx2-Sc - 117 μm, the one (and only) crack observed nucleated at higher stress levels. The explanation for this difference in behaviour may lie in the different microstructures achieved after solution heat treatment, as discussed in chapter 5.3. The tensile specimens of CoEx2-Sc have a uniform small grain size in the sleeve material, thus having higher toughness than CoEx1 which has large recrystallized grains at the sleeve edge [7]. The results of the fractography of CoEx1 - 180 μm found clear support for brittle fracture in the sleeve. Overall these findings are in accordance with the theory about grain size reduction (chapter 2.4.1) and findings reported by D.R. Lesuer et al. [40]: Coarse-grained materials do often exhibit brittle fracture, which should be avoided in metal composites as they will cause early failure. A finely grained microstructure will increase the thoroughness.

Another observation from the graph was that the specimen of CoEx2-Sc with an average sleeve thickness of 431 μm displayed a maximum stress equal to that of CoEx2-Sc - 182 μm. This could be due to the fact that the CoEx2-Sc - 431 μm specimen was cut from a rod that had fractures at the end of it. It could be possible that this specimen had internal defects not visible from outside, causing premature failure during tensile testing.

From the results of the fractography, the core material shows evidence of ductile

fracture for all specimens examined and ductile fracture between the core and sleeve material. Fractography of the sleeve material showed several types of fracture surfaces, but most of the specimens examined displayed a very fine intergranular- and ductile fracture surface. Except for CoEx1 - 180 μm that exhibited indications of brittle cleavage fracture in some areas of the sleeve material, as discussed above.

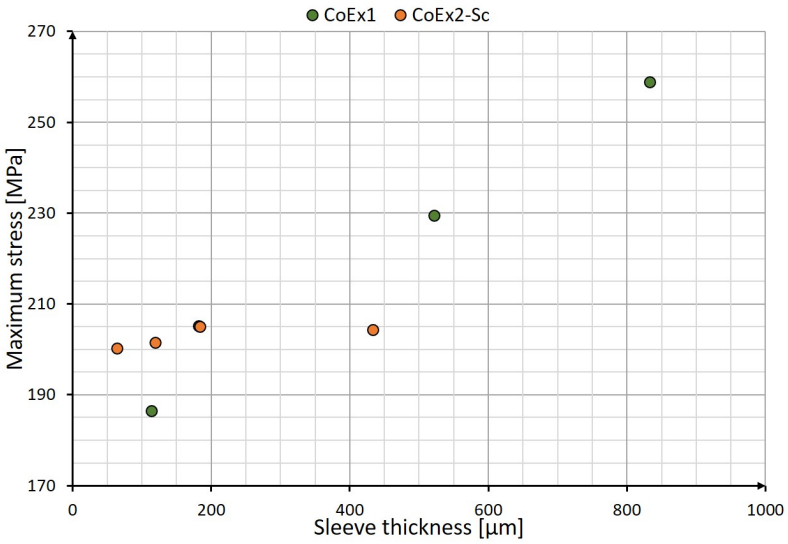

Figure 5.3: *Maximum stress measured during tensile testing plotted against the average sleeve thickness of the tensile specimens. The green circles are CoEx1, while the orange circles are CoEx2-Sc.*

6 Conclusion

Two aluminium alloys, AA7090 and AA7090 with additions of Sc, have been rapidly solidified (RS) by melt spinning and cold compacted into billets. These billets were used to produce co-extruded 12 mm diameter rods with either RS AA7090 or RS AA7090-Sc as the sleeve material and AA6082 as the core material. Hence, referred to as CoEx1 and CoEx2-Sc, respectively. The co-extruded rods have been characterized and tested mechanically giving the following results:

1. Co-extrusion at a container temperature of 440°C and an extrusion speed of 0.32 m/min resulted in co-extruded rods with the best quality. The rods extruded at a container temperature of 460°C experienced partial cracking in the surface. Through microstructural observations and tensile testing, the rods seemed to have achieved excellent metallurgical bonding between the two dissimilar alloys.

2. Heat treatment of the co-extruded rods was done by solution heat treatment at 470°C and precipitation hardening at 140°C. Maximum hardness in the sleeve material of both CoEx1 and CoEx2-Sc was achieved after 8 hours of precipitation hardening. The hardness measured of the core and sleeve of CoEx1 were 47 HV1 and 216 HV1, respectively. For CoEx2-Sc, the hardness of the core and sleeve were measured to 45 HV1 and 210 HV1, respectively.

3. During solution heat treatment, CoEx1 experienced recrystallization and grain growth at the edge of the sleeve material. While CoEx2-Sc was able to withstand recrystallization at 470°C. The present findings confirm that additions of Sc to the AA7090 alloy resulted in improved resistance to recrystallization.

4. Tensile testing of the aged co-extruded rods demonstrated a nearly linear relationship between the maximum stress and sleeve thickness. Specimens of CoEx1 with a sleeve thickness of 180 μm and 831 μm achieved maximum stresses of 205 MPa and 259 MPa, respectively. In comparison, the tensile strength measured for AA6082 was 200 MPa. While the tensile strength measured for RS AA7090 was 693 MPa. CoEx2-Sc displayed less cracking in the sleeve material during tensile testing. This is thought to be the result of a finer microstructure due to improved resistance to recrystallization as concluded above, increasing the toughness.

The main conclusion that can be drawn from these findings is that co-extrusion of AA6082 with a sleeve of rapid solidified AA7090-Sc may provide a potential solution to achieve increased strength, without sacrificing other properties and cost.

Further Work

Future research should develop and confirm these initial findings. Additional co-extrusion trials with varying parameters should be done to optimize the co-extrusion process with regards to quality and uniform sleeve thickness. There should be produced more parallels with similar sleeve thickness and material for mechanical characterization through tensile testing. In order to further investigate the bonding strength between the two dissimilar alloys during, a shear blanking test as described by T. Sapanathan et al. [41] is suggested. It might also be interesting to examine the wear and fatigue properties of the co-extruded rods. The high-temperature properties of the AA7090 alloy with additions of Sc should be further investigated, as there seems to be improved resistance to recrystallization and grain growth for this alloy. In addition, corrosion testing might prove an important area for future research. Rapid solidification might have suppressed the formation of intermetallic particles, often associated with localized corrosion for the 7xxx alloys.

Bibliography

References

[1] M. Delogu et al. “Innovative composites and hybrid materials for electric vehicles lightweight design in a sustainability perspective”. In: *Materials Today Communications* 13 (2017), pp. 192–209.

[2] Thilo Bein et al. “Enhanced Lightweight Design – First Results of the FP7 Project ENLIGHT”. In: *Transportation Research Procedia* 14 (2016), pp. 1031–1040.

[3] Bob Piascik et al. *Materials, Structures, Mechanical Systems, and Manufacturing Roadmap*. NASA Headquarters, Washington, DC 20546: National Aeronautics and Space Administration, 2010.

[4] Martin Goede et al. “Super Light Car—lightweight construction thanks to a multi-material design and function integration”. In: *European Transport Research Review* 1.1 (Mar. 2009), pp. 5–10.

[5] M. Kleiner, M. Geiger, and A. Klaus. “Manufacturing of Lightweight Components by Metal Forming”. In: *CIRP Annals* 52.2 (2003), pp. 521–542.

[6] K. Lu. “The future of metals”. In: *Science* 328 (2010), pp. 319–320.

[7] W. D. Callister and D. G. Rethwisch. *Materials Science and Engineering*. Ninth Edition. Asia: John Wiley and Sons, 2011.

[8] Meng Huang et al. “Role of layered structure in ductility improvement of layered Ti-Al metal composite”. In: *Acta Materialia* 153 (2018), pp. 235–249.

[9] J. K. Solberg. *Teknologiske metaller og legeringer*. 2014.

[10] G. Mrówka-Nowotnik, J. Sieniawski, and M. Wierzbiñska. “Intermetallic phase particles in 6082 aluminium alloy”. In: *Archives of Materials Science and Engineering* 28.2 (Feb. 2007), pp. 69–76.

[11] Nikolay A. Belov, Dmitry G. Eskin, and Andrey A. Aksenov. “Chapter 2 - Alloys of the Al–Mg–Si–Fe System”. In: *Multicomponent Phase Diagrams*. Ed. by Nikolay A. Belov, Dmitry G. Eskin, and Andrey A. Aksenov. Oxford: Elsevier, 2005, pp. 47–82.

[12] J. R. Davis. *Aluminium and Aluminium Alloys*. Third Series. Materials Park, OH 440730002: ASM International Handbook Committee, 1993.

[13] E. Lavernia, G. Rai, and N. J. Grant. “Rapid Solidification Processing of 7XXX Aluminium Alloys: A review”. In: *Materials Science and Engineering* (1986).

[14] Nikolay A. Belov, Dmitry G. Eskin, and Andrey A. Aksenov. "Chapter 6 - Alloys with a High Content of Zinc". In: *Multicomponent Phase Diagrams*. Ed. by Nikolay A. Belov, Dmitry G. Eskin, and Andrey A. Aksenov. Oxford: Elsevier, 2005, pp. 193–222.

[15] Usama S. Mohammad Mustafa Kamal. *A review: Chill-Block Melt Spin Technique, Theories and Applications*. Mansoura University, Egypt: Bentham Science Publishers, 2012.

[16] W. Kurz and D.J. Fisher. *Fundamentals of Solidification*. Fourth Revised Edition. Switzerland: Trans Tech Publications Ltd., 1998.

[17] Lennart Bäckerud, Ella Król, and Jarmo Tamminen. *Solidification Characteristics of Aluminium Alloys*. Vol. 1: Wrought Alloys. Oslo, Norway: Skanaluminium, 1986.

[18] Inge Johansen. "Properties, Microstructure and Modelling of an RS Aluminium Alloy". PhD thesis. University of Trondheim, June 1995.

[19] O. Neikov and Alexander V. Krajnikov. "Advanced PM Aluminium Alloys Produced by New Rapid Solidification Technology". In: *Powder Metallurgy World Congress* 1 (Oct. 2004), pp. 237–242.

[20] Yaojun Lin et al. "The quantitative relationship between microstructure and mechanical property of a melt spun Al–Mg alloy". In: *Materials Science and Engineering: A* 621.Supplement C (2015), pp. 212–217.

[21] Loren A. Jacobson and Joanna McKittrick. "Rapid solidification processing". In: *Materials Science and Engineering: R: Reports* 11.8 (1994), pp. 355–408.

[22] Hongchun Yu et al. "Microstructure and tensile properties of large-size 7055 aluminum billets fabricated by spray forming rapid solidification technology". In: *Journal of Alloys and Compounds* 578.Supplement C (2013), pp. 208–214.

[23] Department of Engineering Physics GITAM. *Hard Ferromagnetic*. URL: `http://eresources.gitam.edu/Engg_Phys/semester_2/magnetic/hard.htm`.

[24] Pradip K. Saha. "Fundamentals of Extrusion". In: *ASM International* (2000).

[25] E. Priel, Z. Ungarish, and N.U. Navi. "Co-extrusion of a Mg/Al composite billet: A computational study validated by experiments". In: *Journal of Materials Processing Technology* 236.Supplement C (2016), pp. 103–113.

[26] M. Thirumurugan et al. "Improved ductility in ZM21 magnesium–aluminium macrocomposite produced by co-extrusion". In: *Journal of Materials Processing Technology* 211.10 (2011), pp. 1637–1642.

[27] Marko Knezevic et al. "Material-based design of the extrusion of bimetallic tubes". In: *Computational Materials Science* 95.Supplement C (2014), pp. 63–73.

[28] R. Sliwa. "Plastic zones in the extrusion of metal composites". In: *Journal of Materials Processing Technology* 67.1 (1997). Proceedings of the International Conference on Mechanics of Solids and Materials Engineering, pp. 29–35.

[29] Pawel Kazanowski, Mario E Epler, and Wojciech Z Misiolek. "Bi-metal rod extrusion—process and product optimization". In: *Materials Science and Engineering: A* 369.1 (2004), pp. 170–180.

[30] L.K Berg et al. "GP-zones in Al–Zn–Mg alloys and their role in artificial aging". In: *Acta Materialia* 49.17 (2001), pp. 3443–3451.

[31] D. Tabor. "The hardness of solids". In: *Review of Physics in Technology* 1.3 (1970), p. 145. URL: http://stacks.iop.org/0034-6683/1/i=3/a=I01.

[32] Vegard Jørgenvåg Bjerkestrand. "Characterization and Mechanical Testing of Co-extruded Rods with an AA 6082 Core and Rapidly Solidified AA 7090 Surface Layer". Project Thesis. Norwegian University of Science and Technology, Dec. 2017.

[33] H. Kalager. "Characterization of Coextruded Rods with Al-4,5Mg as the Base Alloy and Rapidly Solidified Al-4,5Mg-1Ag as the Surface Alloy". Master Thesis. Norwegian University of Science and Technology, June 2017.

[34] Nick McCormick and Jerry Lord. "Digital Image Correlation". In: *Materials Today* 13.12 (2010), pp. 52–54. ISSN: 1369-7021.

[35] Shi-hua Fu et al. "The Mechanism of Critical Strain of Serrated Yielding in Strain Rate Domain". In: *Chinese Physics Letters* 33.2 (2016), pp. 360–370.

[36] Susanne Koch and Helmut Amtrekowitsch. "Study of the precipitation kinetics in AlMgZn alloys by using DSC". In: *European Metallurgical Conference EMC 2007* 4 (2007), pp. 1947–1956.

[37] Myriam Nicolas. "Precipitation evolution in an Al-Zn-Mg alloy during non-isothermal heat treatments and in the heat-affected zone of welded joints." In: *Material chemistry. Institut National Polytechnique de Grenoble - INPG* (2002), pp. 37–72.

[38] Grazyna Mrówka-Nowotnik and Jan Sieniawski. "Precipitation evolution in an Al-Zn-Mg alloy during non-isothermal heat treatments and in the heat-affected zone of welded joints." In: *Rzeszow University of Technology, Poland* (2007), pp. 449–454.

[39] Y. W. Riddle and T. H. Sanders. "A study of coarsening, recrystallization, and morphology of microstructure in Al-Sc-(Zr)-(Mg) alloys". In: *Metallurgical and Materials Transactions A* 35.1 (Jan. 2004), pp. 341–350.

[40] D. R. Lesuer et al. "Mechanical behaviour of laminated metal composites". In: *International Materials Reviews* 41.5 (1996), pp. 169–197.

[41] Thaneshan Sapanathan et al. “Shear blanking test of a mechanically bonded aluminum/copper composite using experimental and numerical methods”. In: *Materials Science and Engineering: A* 623 (2015), pp. 153–164.

Appendices

A - Recorded Co-extrusion Parameters

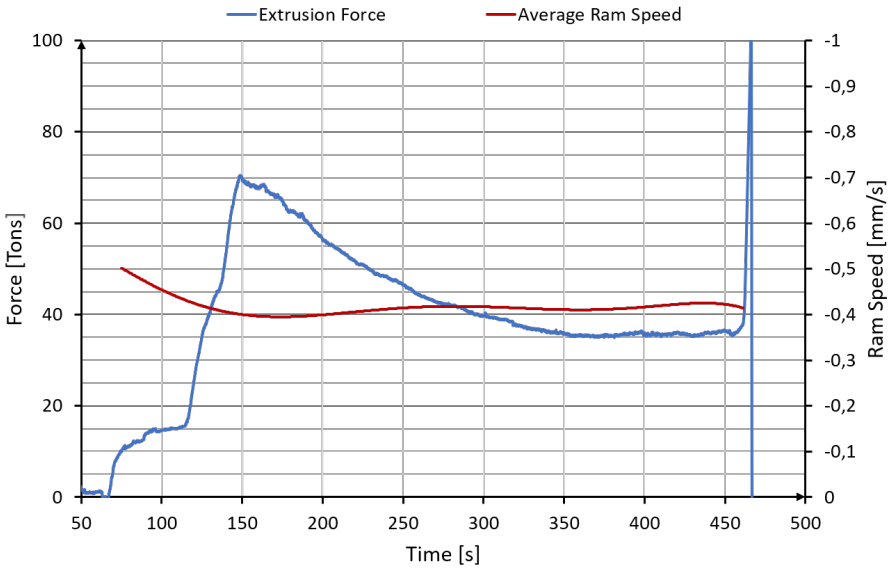

Figure A.1: *Recorded extrusion force (blue line) and average ram speed (red line) during the co-extrusion of R2 part 2.*

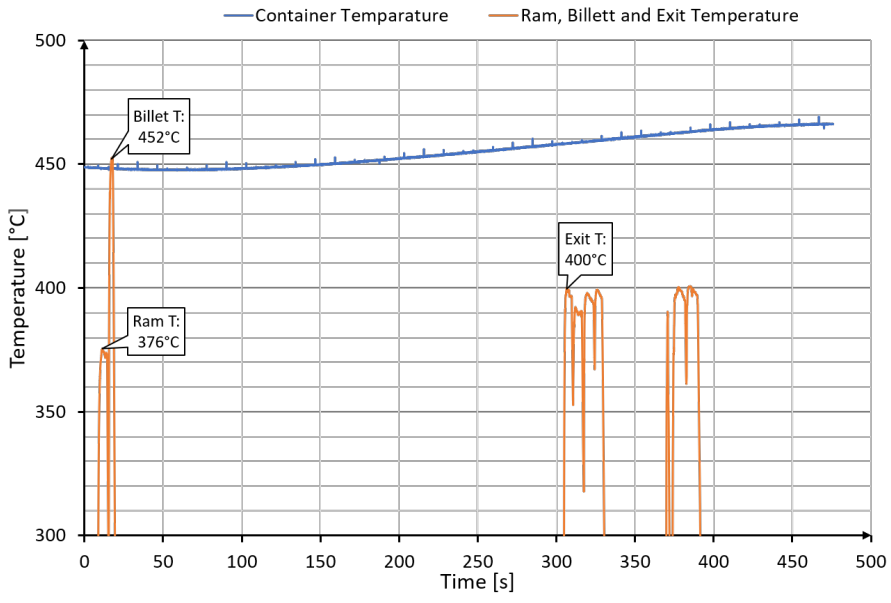

Figure A.2: *Recorded container temperature (blue line) and ram- billet- and exit temperature (marked on the orange line) during the co-extrusion of R2 part 2.*

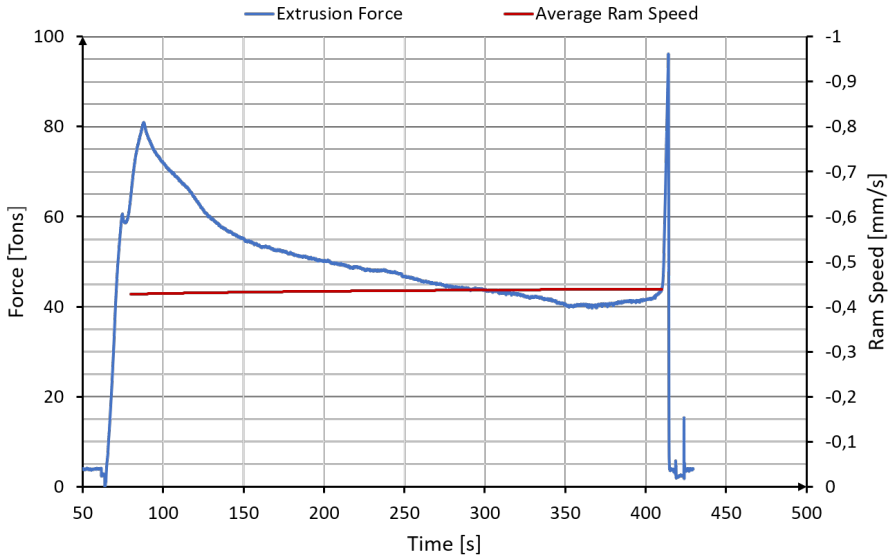

Figure A.3: *Recorded extrusion force (blue line) and average ram speed (red line) during the co-extrusion of R3 part 1.*

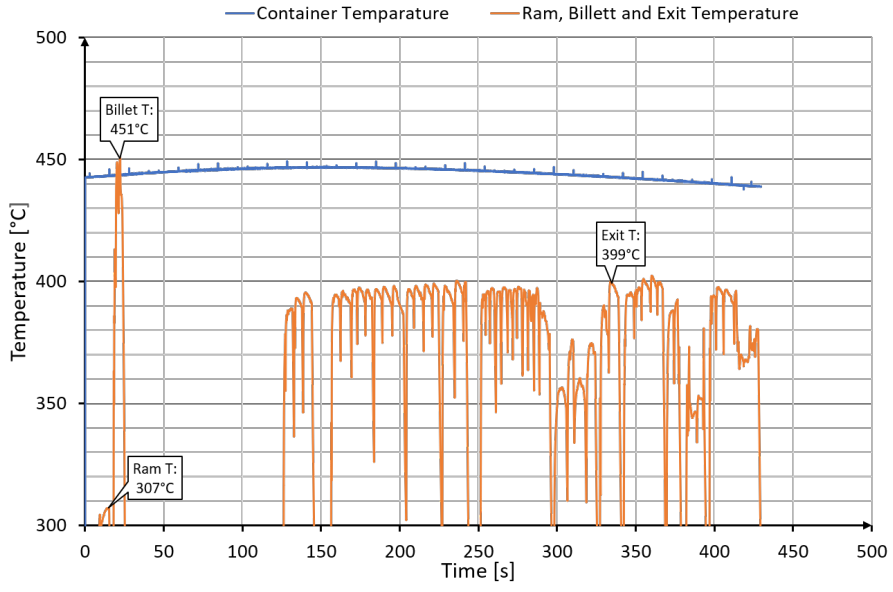

Figure A.4: *Recorded container temperature (blue line) and ram- billet- and exit temperature (marked on the orange line) during the co-extrusion of R3 part 1.*

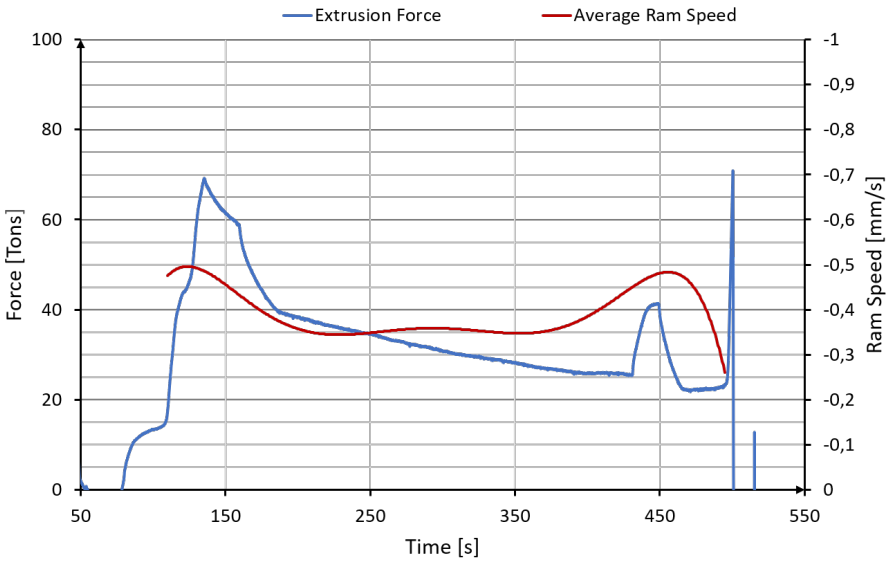

Figure A.5: *Recorded extrusion force (blue line) and average ram speed (red line) during the co-extrusion of R3 part 2.*

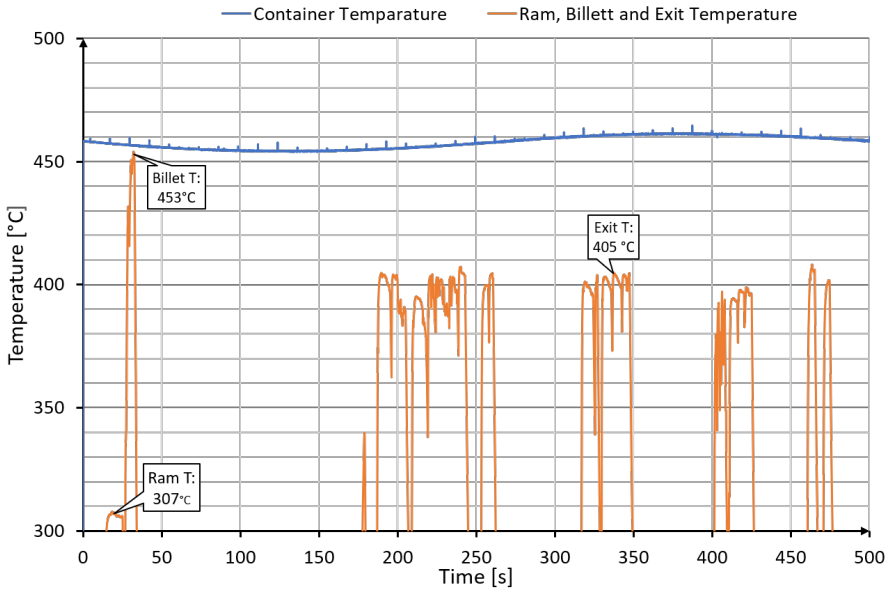

Figure A.6: *Recorded container temperature (blue line) and ram- billet- and exit temperature (marked on the orange line) during the co-extrusion of R3 part 2.*

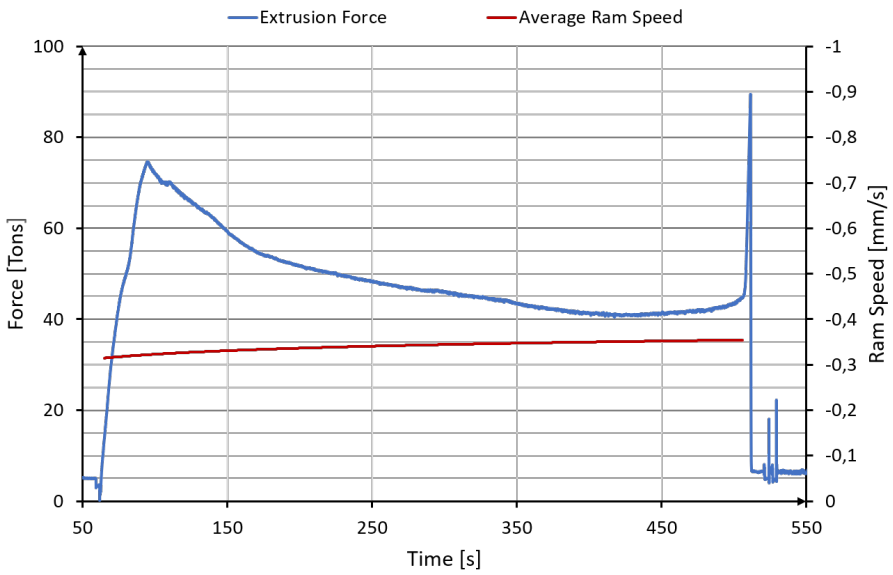

Figure A.7: *Recorded extrusion force (blue line) and average ram speed (red line) during the co-extrusion of R4 part 1.*

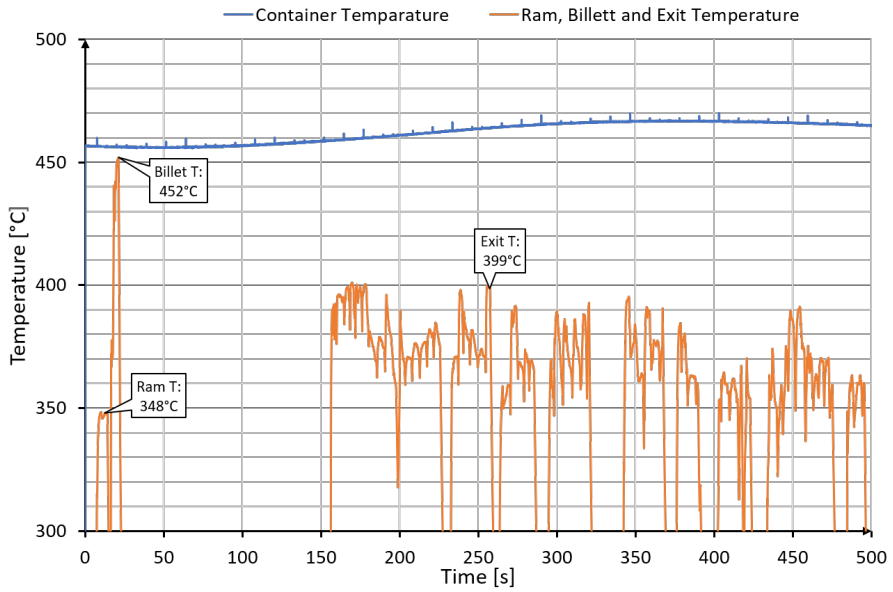

Figure A.8: *Recorded container temperature (blue line) and ram- billet- and exit temperature (marked on the orange line) during the co-extrusion of R4 part 1.*

B - Recorded Extrusion Parameters From DC AA7090 and R1

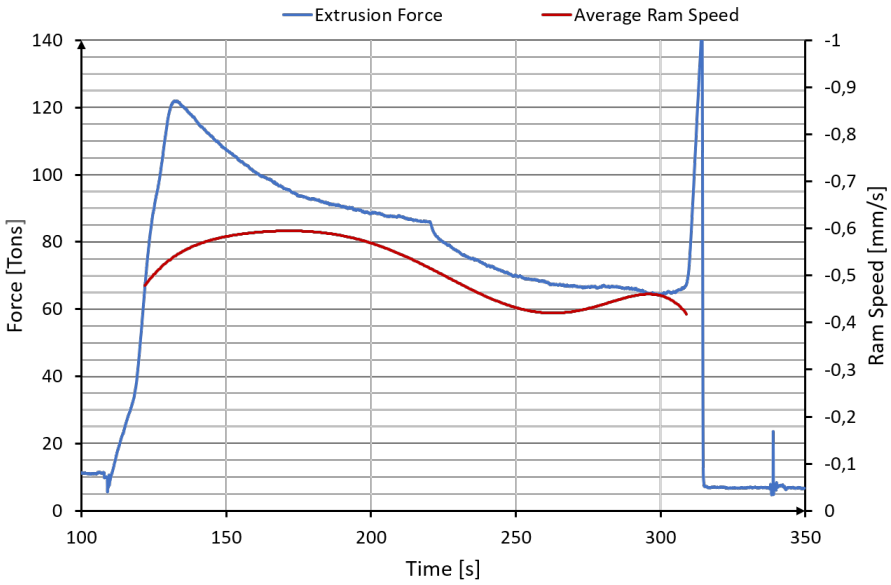

Figure B.1: *Recorded extrusion force (blue line) and average ram speed (red line) during the extrusion of DC AA7090.*

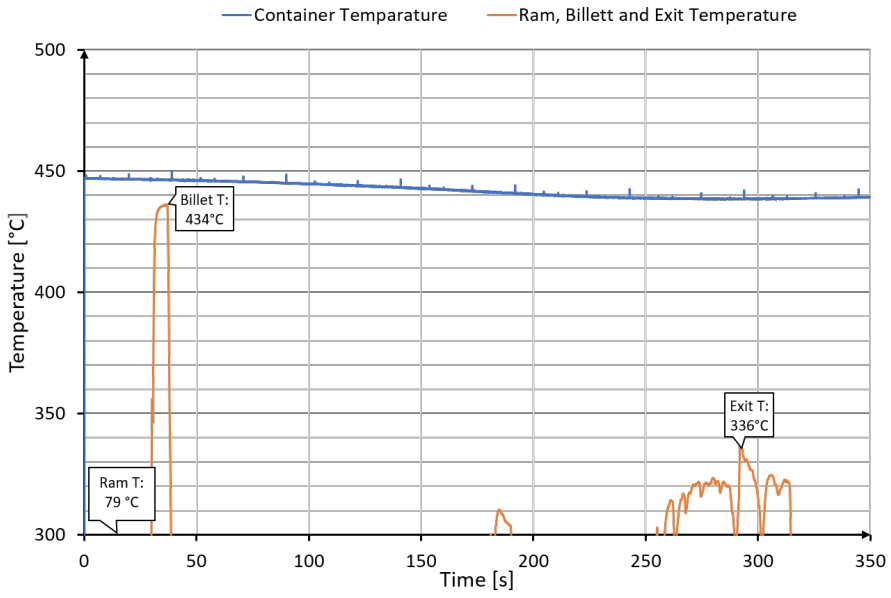

Figure B.2: *Recorded container temperature (blue line) and ram- billet- and exit temperature (marked on the orange line) during the extrusion of DC AA7090.*

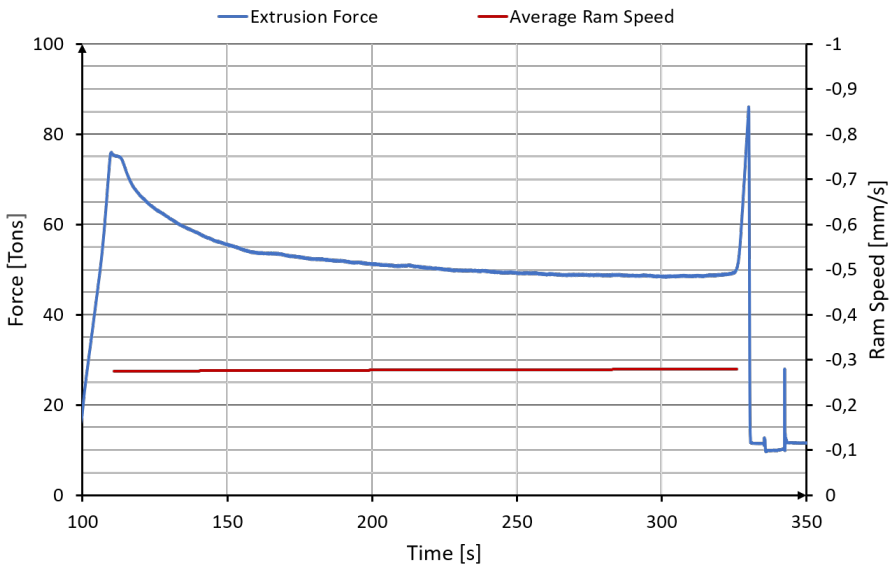

Figure B.3: *Recorded extrusion force (blue line) and average ram speed (red line) during the extrusion of R1.*

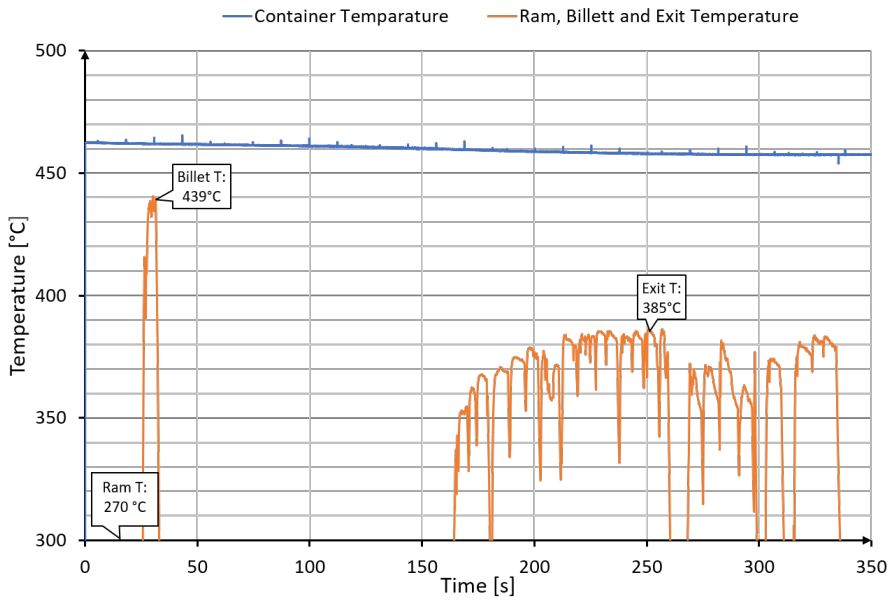

Figure B.4: *Recorded container temperature (blue line) and ram- billet- and exit temperature (marked on the orange line) during the extrusion of R1.*

C - Graphs of the Sleeve Thickness Along the Co-Extruded Rods

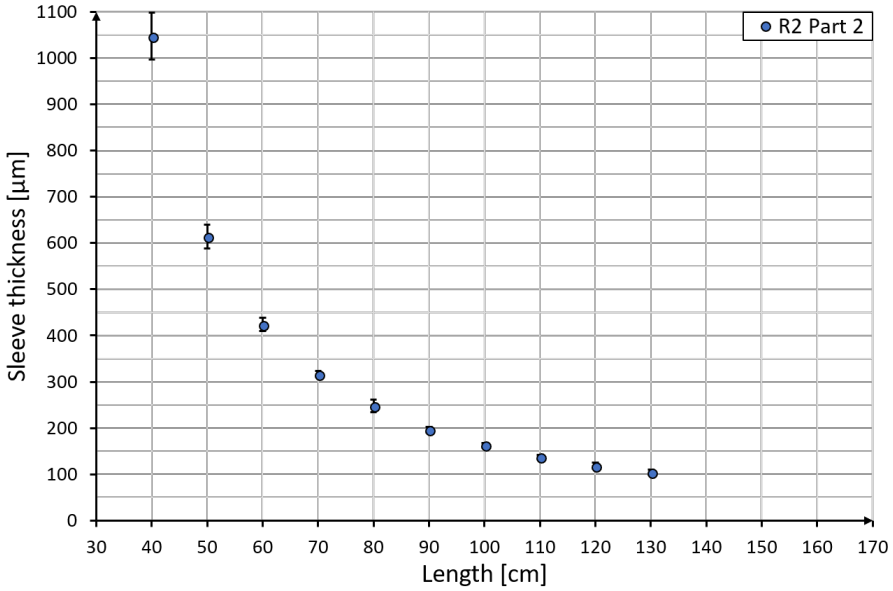

Figure C.1: *Average sleeve thickness with standard deviation at different positions along the co-extruded rod R2 Part 2.*

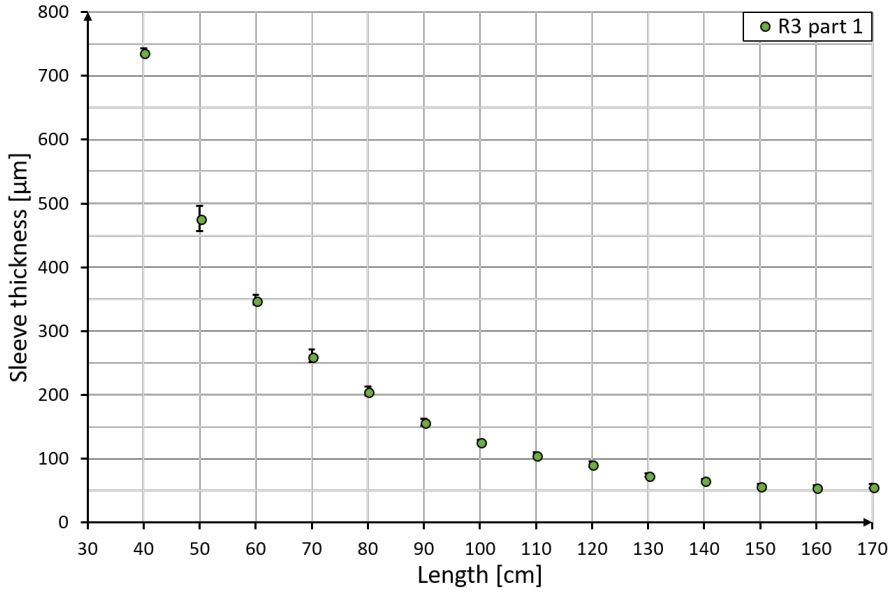

Figure C.2: *Average sleeve thickness with standard deviation at different positions along the co-extruded rod R3 Part 1.*

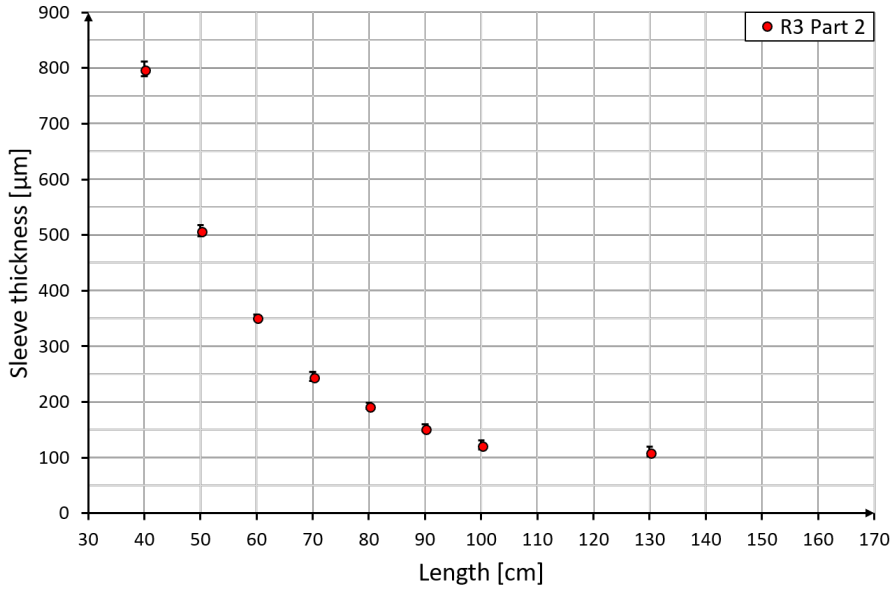

Figure C.3: *Average sleeve thickness with standard deviation at different positions along the co-extruded rod R3 Part 2.*

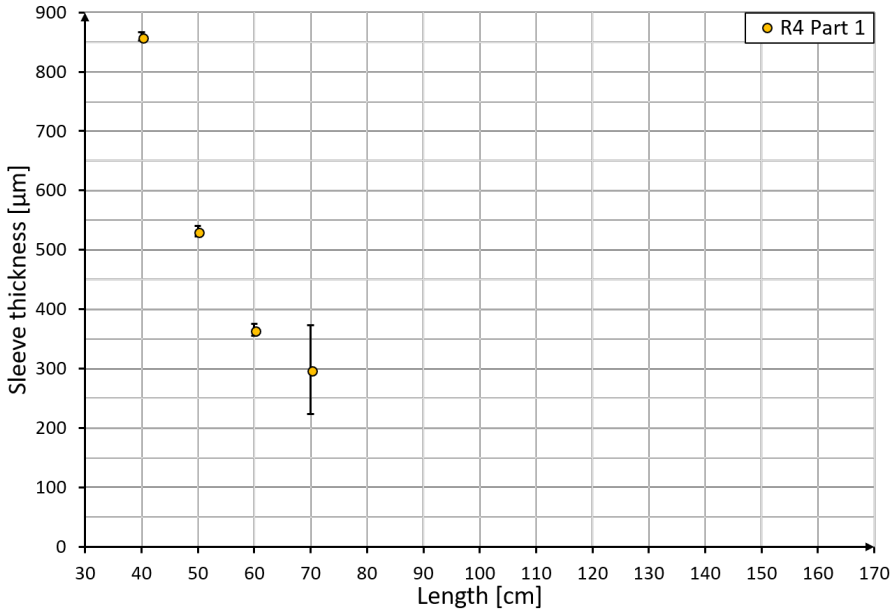

Figure C.4: *Average sleeve thickness with standard deviation at different positions along the co-extruded rod R4 Part 1.*

D - Deformation Images From DIC During Tensile Testing of Co-Extruded Rods

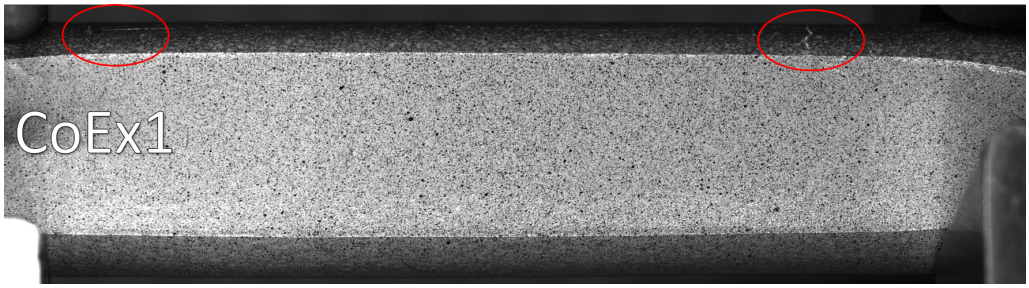

(a) *Image taken of a specimen from CoEx1 with a sleeve thickness of 180 µm being subjected to 205 MPa and 0.13 strain.*

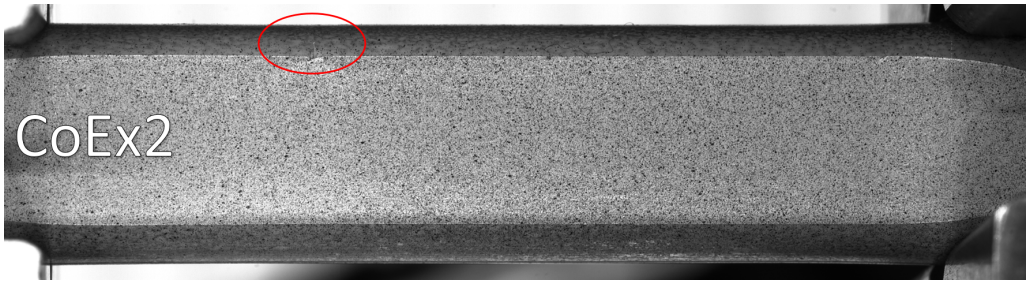

(b) *Image taken of a specimen from CoEx2 with a sleeve thickness of 182 µm being subjected to 205 MPa and 0.18 strain.*

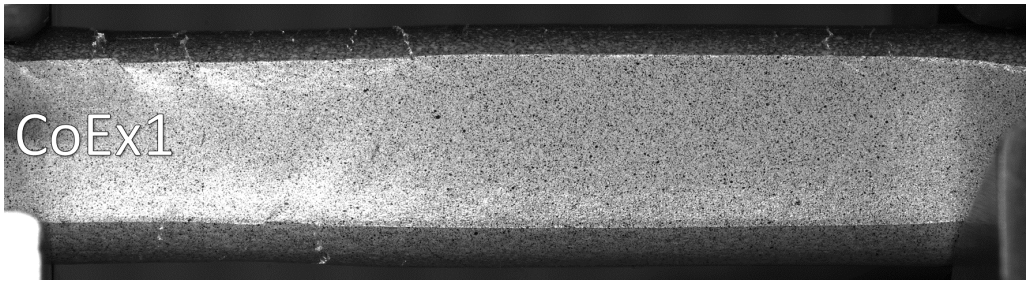

(c) *Image taken of a specimen from CoEx1 with a sleeve thickness of 180 µm being subjected to 191 MPa and 0.18 strain.*

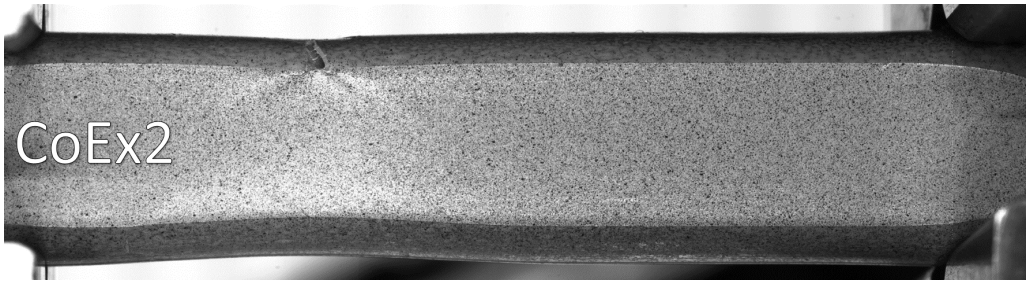

(d) *Image taken of a specimen from CoEx2 with a sleeve thickness of 182 µm being subjected to 191 MPa and 0.23 strain.*

Figure D.1: *Four images of captured with the DIC to show the difference in sleeve behaviour of CoEx1 - 180 µm (**a**) and **c**)) and CoEx2 - 182 µm (**b**) and **d**)) experiencing 205 MPa (**a**) and **b**)) and 191 MPa (**c**) and **d**)).*

E - Lines Measuring Local Strains in the Sleeve and Core During Tensile Testing Using DIC

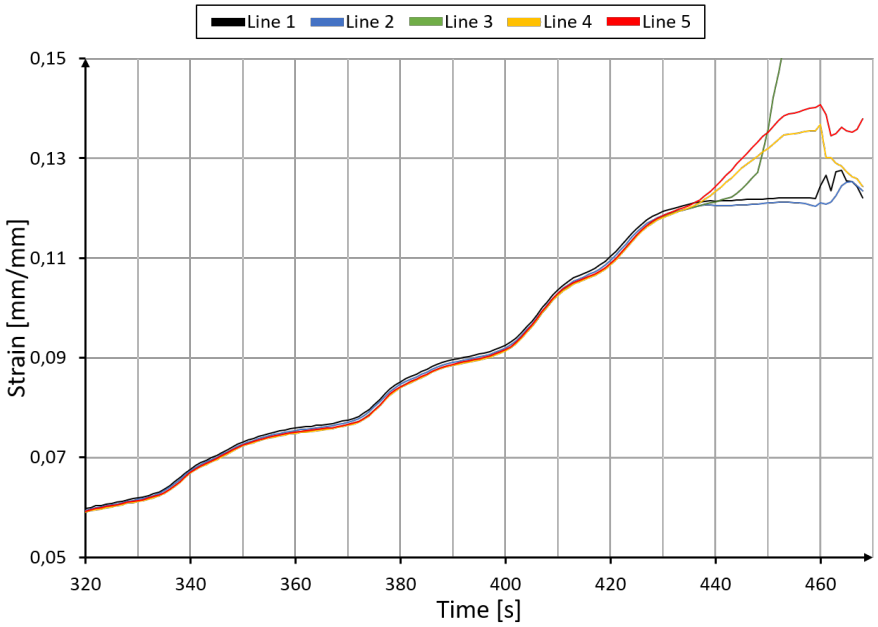

Figure E.1: *Graph showing the local strains measured by the five vector lines in the sleeve (black and blue) and core (green, yellow and red) during tensile testing of CoEx1 - 520 mum.*

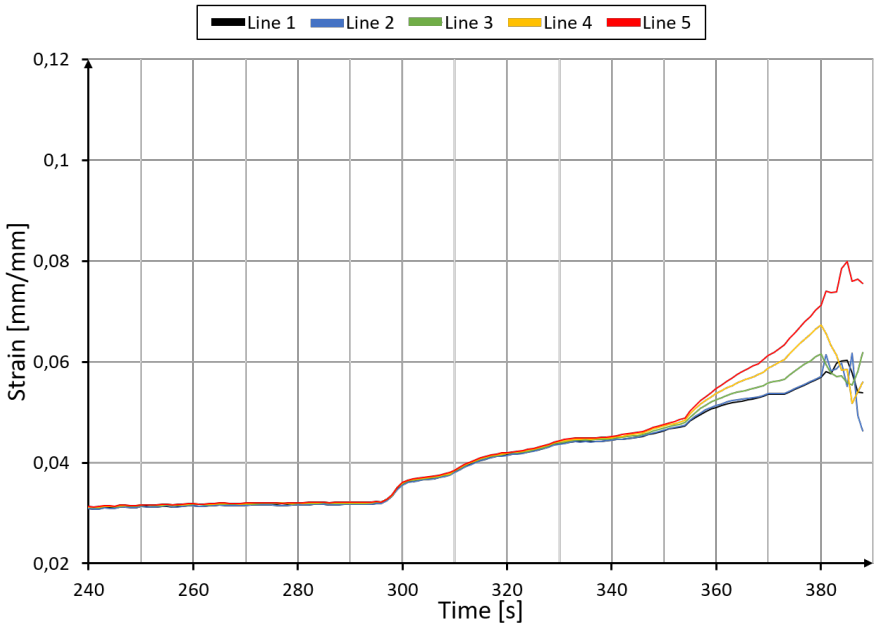

Figure E.2: *Graph showing the local strains measured by the five vector lines in the sleeve (black and blue) and core (green, yellow and red) during tensile testing of CoEx2-Sc - 431 mum.*